

# Design of radiation-hard CMOS sensors for particle detection applications

---

**Berdalović, Ivan**

**Doctoral thesis / Disertacija**

**2019**

*Degree Grantor / Ustanova koja je dodijelila akademski / stručni stupanj:* **University of Zagreb, Faculty of Electrical Engineering and Computing / Sveučilište u Zagrebu, Fakultet elektrotehnike i računarstva**

*Permanent link / Trajna poveznica:* <https://urn.nsk.hr/urn:nbn:hr:168:593406>

*Rights / Prava:* [In copyright](#)/[Zaštićeno autorskim pravom.](#)

*Download date / Datum preuzimanja:* **2025-03-14**



*Repository / Repozitorij:*

[FER Repository - University of Zagreb Faculty of Electrical Engineering and Computing repository](#)





University of Zagreb

FACULTY OF ELECTRICAL ENGINEERING AND COMPUTING

Ivan Berdalović

**DESIGN OF RADIATION-HARD CMOS  
SENSORS FOR PARTICLE DETECTION  
APPLICATIONS**

DOCTORAL THESIS

Zagreb, 2019





University of Zagreb

FACULTY OF ELECTRICAL ENGINEERING AND COMPUTING

Ivan Berdalović

**DESIGN OF RADIATION-HARD CMOS  
SENSORS FOR PARTICLE DETECTION  
APPLICATIONS**

DOCTORAL THESIS

Supervisor: Professor Tomislav Suligoj, PhD

Zagreb, 2019



Sveučilište u Zagrebu  
FAKULTET ELEKTROTEHNIKE I RAČUNARSTVA

Ivan Berdalović

**PROJEKTIRANJE CMOS SENZORA  
OTPORNIH NA ZRAČENJE ZA  
PRIMJENU U DETEKCIJI ČESTICA**

DOKTORSKI RAD

Mentor: Prof. dr. sc. Tomislav Suligoj

Zagreb, 2019.

The doctoral thesis was done at the University of Zagreb, Faculty of Electrical Engineering and Computing, at the Department of electronics, microelectronics, computer and intelligent systems.

Supervisor: Professor Tomislav Suligoj, PhD

The doctoral thesis contains: 120 pages

Doctoral thesis no.: \_\_\_\_\_

## About the Supervisor

Tomislav Suligoj received his Engineer Diploma, MSc and PhD degrees in electrical engineering from the University of Zagreb, Faculty of Electrical Engineering and Computing (FER), Croatia, in 1995, 1998 and 2001, respectively. Currently, he is a full professor at FER, Department of Electronics, Microelectronics, Computer and Intelligent Systems, teaching the courses in the area of electronics and microelectronics. He was a visiting researcher at the University of California, Los Angeles (1999-2001) and a postdoctoral researcher at the Hong Kong University of Science and Technology (2001-2002). He has been a Principal Investigator of more than 20 projects so far, supported by government agencies, international companies and universities. He has published 19 patents and more than 140 papers in journals and conference proceedings in the area of design, measurements and modelling of electron devices, micro- and nano- electronics, semiconductor technology and integrated circuit design. Prof. Suligoj has received 14 scientific awards including the National Science Award in 2015; the Golden plaque at the innovation exhibition ARCA; Best paper awards at the MIPRO MEET conference, Faculty medals "Josip Lončar" for outstanding Doctoral Dissertation, and a Fulbright scholarship. He is a Technical Program Committee member and a Chairman of Device Physics Subcommittee at IEEE Bipolar/BiCMOS Circuits and Technology Meeting (BCTM). He is a Steering Committee member of the MIPRO MEET conference. He was the President of the Electron Devices/Solid-State Circuits Joint Chapter, IEEE Croatia Section from 2010 until 2013. He gave numerous invited talks at conferences, universities, institutions and companies.

## O mentoru

Tomislav Suligoj je diplomirao, magistrirao i doktorirao u polju elektrotehnike na Sveučilištu u Zagrebu, Fakultetu elektrotehnike i računarstva (FER), 1995., 1998. odnosno 2001. godine. Trenutno je redoviti profesor na Zavodu za elektroniku, mikroelektroniku, računalne i inteligentne sustave FER-a, gdje predaje kolegije u području elektronike i mikroelektronike. Bio je gostujući istraživač na University of California, Los Angeles od 1999. do 2001. godine te na poslijedoktorskom usavršavanju na Hong Kong University of Science and Technology od 2001. do 2002. Do sada je vodio više od 20 projekata financiranih od strane državnih institucija, međunarodnih kompanija i sveučilišta. Objavio je 19 patenata i više od 140 radova u časopisima i zbornicima konferencija u području projektiranja, mjerenja i modeliranja elektroničkih elemenata, mikro- i nano- elektronike, poluvodičke tehnologije i projektiranja integriranih sklopova. Prof. Suligoj dobitnik je 14 nagrada uključujući Državnu nagradu za znanost 2015. g., Zlatnu plaketu na izložbi inovacija ARCA, Best paper award na MIPRO MEET konferenciji, srebrnu plaketu "Josip Lončar" za posebno istaknutu doktorsku disertaciju te Fulbrightovu stipendiju. Član je Technical Program Committee i Chairman of Device Physics Subcommittee konferencije IEEE Bipolar/BiCMOS Circuits and Technology Meeting (BCTM). Član je Steering Committee konferencije MIPRO MEET. Bio je predsjednik Odjela za elektroničke elemente i poluvodičke integrirane sklopove Hrvatske sekcije IEEE 2010.-2013. Održao je velik broj pozvanih predavanja na međunarodnim konferencijama, sveučilištima, institutima i kompanijama.

## **Acknowledgement**

I would like to thank my supervisors at CERN, Dr. Heinz Pernegger and Dr. Walter Snoeys for their help and guidance throughout this PhD project. Working with you has been an honour and an experience I will never forget. I would also like to thank my supervisor at the University of Zagreb, Prof. Tomislav Suligoj for his support during the PhD and for letting me pursue the topics I was interested in, never pressuring me to do anything that was not in my best interest. Thanks to Thanushan Kugathasan, Cesar Augusto Marin Tobon, Enrico Junior Schioppa, Carlos Solans Sanchez and everyone else in the EP-ESE-ME and EP-ADE-ID groups who made this work possible. Special thanks to Valerio Dao, whose firmware and software expertise are responsible for a lot of the fancy plots included in this thesis. Thanks also to my office mates, Roberto Cardella, Francesco Piro and Leyre Flores for endless discussions on everything related to electronics and physics, especially during philosophical Fridays. Finally, thanks to my family, who have supported me every step of the way, even from a thousand kilometres away. You continue to provide inspiration and motivation for everything I want to do in life.

This research project has been supported by a Marie Skłodowska-Curie Innovative Training Network Fellowship of the European Commission's Horizon 2020 Programme under contract number 675587 STREAM.

## **Abstract**

The work focuses on the design of large-scale radiation-hard monolithic CMOS sensors for the upgrades of the detectors in the high-energy physics experiments at CERN. The sensors are manufactured using a novel process modification implemented in the TowerJazz 180 nm CMOS process, which uses small collection electrodes to achieve a low sensor capacitance in the order of a few femtofarads, resulting in low noise and low analogue power consumption. The process modification provides full depletion of the sensitive layer and a radiation hardness promising to meet the requirements of the pixel detectors in CERN's largest experiments. The sensors implement a matrix of small pixels (in the order of 30 micrometres) containing a fast, low-noise front-end amplifier and a novel asynchronous digital readout architecture. Measurement results from these sensors before and after irradiation are also discussed.

**Keywords:** Active pixel sensors, CMOS integrated circuits, position sensitive particle detectors, radiation effects, radiation hardening (electronics), semiconductor detectors, solid-state circuit design

# Projektiranje CMOS senzora otpornih na zračenje za primjenu u detekciji čestica

Potruga za novim otkrićima u fizici čestica u Velikom hadronskom sudaraču (engl. Large Hadron Collider, LHC) u Europskoj organizaciji za nuklearna istraživanja (CERN) temelji se na detekciji čestica nastalih u sudarima protona ili teških iona. Protoni se kroz kompleks akceleratora ubrzavaju do energija od 6.5 TeV te se sudaraju u četiri najveća eksperimenta: ATLAS, CMS, ALICE i LHCb. Eksperimenti se sastoje od slojeva detektora koji su postavljeni u koncentričnim cilindrima oko točke sudara te služe za mjerenje naboja, količine gibanja i energije čestica nastalih u sudarima kao i čestica nastalih raspadom kratkoživućih čestica. U slučaju eksperimenta ATLAS, detektori se mogu podijeliti na nekoliko glavnih vrsta. Unutrašnji detektor (engl. Inner Detector, ID) sastoji se od silicijskih piksel i strip detektora visoke rezolucije položaja koji služe za precizno praćenje čestica blizu mjesta sudara. Pomoću njih se obavlja rekonstrukcija putanja čestica u magnetskom polju, gdje zakrivljenost putanje otkriva naboj i količinu gibanja čestica. Elektromagnetski i hadronski kalorimetri služe za mjerenje energije čestica, dok mionski spektrometar obavlja mjerenje količine gibanja miona koji prođu kroz sve ostale slojeve eksperimenta.

Budući da su zanimljivi fizikalni procesi (poput raspada Higgsova bozona) vrlo rijetki, LHC će između 2023. i 2025. biti podvrgnut nadogradnji koja će povećati broj sudara čestica u jedinici vremena za gotovo red veličine. Kako bi se mogli nositi s ovakvim porastom luminoziteta, nekolicinu sustava, uključujući i detektore, također će biti potrebno nadograditi. Veći broj čestica rezultirat će većim brojem detekcija u jedinici vremena, što bi moglo dovesti do smanjenja efikasnosti zbog ograničenja u brzini očitavanja podataka iz detektora. Dodatno ograničenje, osobito kod piksel detektora blizu mjesta sudara, su oštećenja uzrokovana ekstremnim količinama zračenja u tim sredinama tijekom čitavog vremena života detektora. Trenutno svi eksperimenti koriste tzv. hibridne piksel detektore za praćenje čestica u unutrašnjim slojevima. Kod ovakve vrste detektora, sam senzor je proizveden na zasebnoj pločici silicija, dok je elektronika za očitavanje proizvedena na drugoj pločici, obično u standardnom CMOS procesu, te je sa senzorom povezana malim vodljivim spojevima (engl. flip-chip bump-bonding). Senzor je zasebno optimiran za rad u uvjetima visoke razine zračenja, dok sklopovlje za očitavanje projektirano u tehnologiji malih dimenzija omogućuje visoku brzinu i sofisticirano procesiranje podataka.

Iako su zbog dobrih performansi hibridni detektori trenutno standard u detekciji čestica, jedan od glavnih nedostataka jest komplicirana i skupa tehnologija povezivanja dva čipa. Osim toga, disipacija snage i samim time zahtjevi za hlađenjem detektora su visoki, što rezultira velikom količinom materijala, koja pak ograničava rezoluciju količine gibanja zbog raspršenja čestica u materijalu. Zbog toga u novije vrijeme dolazi do razvoja monolitnih CMOS aktivnih piksel senzora (engl. CMOS monolithic active pixel sensors, MAPS), kod kojih su senzor



i sklopovlje za očitavanje integrirani unutar jedne pločice silicija. To u potpunosti eliminira potrebu za povezivanjem čipova, što uz korištenje komercijalnih CMOS procesa znači da su cjenovno vrlo povoljni. Osim toga, kod ovih se detektora kapacitet senzora može dovesti do ekstremno niskih razina, što rezultira niskom potrošnjom snage u odnosu na hibridne detektore te smanjenjem količine materijala. Do nedavno, glavni nedostatak ove tehnologije bila je nedovoljna otpornost na zračenje. Međutim, razvojem CMOS senzorskih procesa, kao što je opisano i u ovom radu, dolazi do pojave monolitnih senzora s poboljšanom otpornošću na zračenje, što ih čini kandidatima čak i za najzahtjevnije primjene. Monolitni CMOS senzori u ovom radu projektirani su s ciljem zadovoljavanja zahtjeva za vanjske slojeve piksel detektora u eksperimentu ATLAS nakon nadogradnje LHC-a. Neki od najvažnijih zahtjeva su efikasnost detekcije od preko 97%, vremenska rezolucija od 25 ns, koliko iznosi vrijeme između sudara dva snopa protona, i to uz potrošnju snage ispod  $500 \text{ mW/cm}^2$ . Zahtjevi moraju biti zadovoljeni nakon što su detektori podvrgnuti dozi od  $10^{15} \text{ 1 MeV n}_{\text{eq}}/\text{cm}^2$  neionizirajućeg zračenja te 50 Mrad ionizirajućeg zračenja tijekom čitavog vremena života u eksperimentu.

Osnovni mehanizam za detekciju čestica u siliciju jest stvaranje parova elektron-šupljina u zaporno polariziranom p-n spoju. Broj ioniziranih nosilaca ovisi o gubitku energije čestice koja prolazi kroz materijal, a koji ovisi o vrsti i samoj energiji čestice. Jedan tip ioniziranih nosilaca sakuplja se na jednoj elektrodi p-n spoja. Naboj generiran unutar osiromašenog područja brzo se sakuplja driftom, a ako sensor nije potpuno osiromašen, i difuzija iz kvazineutralnih područja sudjeluje u procesu sakupljanja naboja. Osim ionizacije parova elektron-šupljina, visokoenergetske čestice mogu izbiti jezgre silicija iz položaja u kristalnoj rešetci, što dovodi do stvaranja defekata u kristalu. To rezultira pojavom energetskih nivoa unutar zabranjenog pojasa (tzv. zamki) koji mogu zarobiti ionizirane nosioce naboja i dovesti do gubitka signala. Kako vjerojatnost zarobljavanja nosilaca ovisi o vremenu sakupljanja naboja, glavna strategija za postizanje otpornosti na ovo neionizirajuće zračenje (engl. non-ionising energy loss, NIEL) jest sakupljati naboj driftom i tako smanjiti vrijeme sakupljanja i vjerojatnost zarobljavanja.

Dva su glavna pristupa u izvedbi sakupljačke elektrode u monolitnim piksel detektorima, i to izvedba s malom sakupljačkom elektrodom, gdje elektroda zauzima tek mali dio piksela, a elektronika za očitavanje nalazi se odvojeno od elektrode, te izvedba s velikom sakupljačkom elektrodom, gdje elektroda zauzima većinu površine piksela, a sklopovlje je smješteno unutar elektrode. Prednost male elektrode je izuzetno nizak kapacitet senzora (reda veličine nekoliko femtofarada), što je povoljno za razinu šuma i disipaciju snage analognih sklopova koji slijede. Međutim, nedostatak male elektrode jest činjenica da je teško postići potpuno osiromašenje sloja za detekciju i samim time zadovoljavajuću otpornost na zračenje. Za potpuno osiromašenje i sakupljanje driftom stoga je povoljnije koristiti piksele s velikom elektrodom, koja međutim znači znatno veći ulazni kapacitet i veće preslušavanje iz digitalnih sklopova za očitavanje prema sakupljačkoj elektrodi.

Kako su sakupljeni naboji relativno mali (reda veličine nekoliko femtokulona), signale s elektrode potrebno je pojačati, što se standardno radi pojačalom osjetljivim na naboj s kapacitivnom povratnom vezom unutar piksela. Važno je da pojačalo ima visoko pojačanje te nizak šum, uz visoku brzinu odziva. Nakon pojačala obično slijedi filtar za suzbijanje nisko- i visokofrekventnih komponenti šuma te komparator, koji osigurava da se očitavaju samo signali iznad određenog praga detekcije. Digitalna arhitektura za očitavanje koja slijedi nakon komparatora vrši dodatno procesiranje signala komparatora te mora do izlaza čipa dovesti točnu adresu piksela unutar dvodimenzionalne matrice u kojima je obavljena detekcija, a u nekim primjenama i informaciju o amplitudi detektiranog signala.

Treba napomenuti da zračenje utječe i na sklopovlje za pojačanje i očitavanje. U ovom slučaju, ionizirajuće zračenje (engl. total ionising dose, TID) uzrokuje nakupljanje pozitivnog naboja u silicijevom dioksidu upravljačke elektrode ili u izolacijskom oksidu tranzistora. Naboj na upravljačkoj elektrodi dovodi do promjena u naponu praga tranzistora, dok naboj u izolacijskom oksidu može dovesti do porasta struje curenja između uvoda i odvoda NMOS tranzistora. Ovi se efekti najčešće sprječavaju primjenom tranzistora s kružnom upravljačkom elektrodom (engl. enclosed layout transistors, ELT), čime se osigurava da sva struja teče ispod upravljačke elektrode.

Monolitni CMOS senzori projektirani u ovom radu proizvedeni su u TowerJazz 180 nm CMOS procesu. Ova tehnologija koristi male sakupljačke elektrode n-tipa. Sklopovlje je odvojeno od elektrode i zaštićeno dubokom implantacijom p-tipa kako podloga PMOS tranzistora ne bi sudjelovala u sakupljanju signalnog naboja. Epitaksijalni sloj p-tipa debljine 25-30  $\mu\text{m}$  koristi se kao sloj za detekciju. Visoka otpornost tog sloja pomaže osiromašenju oko sakupljačke elektrode, no da bi se postiglo potpuno osiromašenje epitaksijalnog sloja i zadovoljavajuća otpornost na neionizirajuće zračenje, potrebna je modifikacija procesa dodavanjem niskodopiranog sloja n-tipa preko cijele matrice piksela. Nakon dobrih rezultata na prototipima senzora u ovom modificiranom procesu, započinje projektiranje velikih detektora koji bi zadovoljili specifikacije eksperimenta ATLAS.

MALTA (engl. Monolithic from ALICE To ATLAS) je senzor koji sadrži matricu od  $512 \times 512$  piksela veličine  $36.4 \times 36.4 \mu\text{m}^2$ . Svaki piksel osim male sakupljačke elektrode promjera 2-3  $\mu\text{m}$  sadrži analogni dio sklopovlja, koji se sastoji od ulaznog pojačala i komparatora, te digitalnu logiku za očitavanje adrese piksela. Ulazno pojačalo temelji se na uvodskom sljedilu koje sakupljeni naboj prenosi s velikog kapaciteta na mali parazitni kapacitet, pri čemu dolazi do visokog naponskog pojačanja. Vrijeme odziva ovisi o sakupljenom naboju, a jedan od glavnih zahtjeva je osigurati dovoljno kratko vrijeme odziva kako bi se svaka detekcija mogla obaviti unutar 25 ns, što je ovom topologijom moguće postići uz disipaciju snage manju od 1  $\mu\text{W}$  po pikselu. Pojačalo je optimirano za prag detekcije od  $200 e^-$ , a pri tome u tranzijentnim simulacijama šuma pokazuje ukupni ekvivalentni šum na ulazu od tek  $7 e^-$ . Dimenzije tranzistora

optimirane su i na način da procesne varijacije što manje utječu na rasipanje praga detekcije, te Monte Carlo simulacije pokazuju standardnu devijaciju praga detekcije od samo  $8 e^-$ . Struje i naponi potrebni za rad pojačala generiraju se pomoću digitalno-analognih pretvornika, a kritični tranzistori u pojačalu i pretvornicima izvedeni su u topologiji s kružnom upravljačkom elektrodom radi otpornosti na ionizirajuće zračenje.

Digitalna elektronika za očitavanje koristi novi, asinkroni način prijenosa podataka unutar matrice piksela. Digitalni impulsi na izlazu komparatora koriste se u generiranju 22-bitnog uzorka kratkih impulsa trajanja do 2 ns, koji se asinkrono šalje niz stupac piksela i sadrži kodiranu adresu piksela u kojem je obavljena detekcija unutar stupca. Prednost asinkronog pristupa je činjenica da nema signala takta unutar velike matrice, što značajno smanjuje digitalnu potrošnju snage, a pritom omogućuje veći broj detekcija u jedinici vremena. Na periferiji čipa, signali iz svih stupaca spajaju se u jednu riječ od 40 bita, koja jednoznačno određuje adresu piksela unutar matrice, te se riječ sa izlaza čipa LVDS standardom šalje do vanjskih sustava za pohranu podataka. Zbog asinkronog prijenosa potrebno je voditi računa o tome da svi signali unutar riječi stignu do izlaza čipa u isto vrijeme, što znači da kapaciteti linija svih bitova u cijelom lancu prijenosa moraju biti potpuno izjednačeni.

Proizvedeni MALTA senzori okarakterizirani su u laboratoriju i u testiranjima zrakom čestica. Pokazuje se da su analogni ulazni sklopovi potpuno funkcionalni te da vremenski odziv odgovara simuliranim vrijednostima. Uz dovoljno nizak prag detekcije, preko 98% signala detektira se unutar 25 ns, čak i bez korekcije za trajanje propagacije impulsa niz stupac piksela od 8 ns. Srednja vrijednost ekvivalentnog šuma ulaznog pojačala također odgovara simulacijama, no primjećeno je da raspodjela šuma ne odgovara Gaussovoj raspodjeli, što se dovodi u vezu s malim dimenzijama pojedinih tranzistora u pojačalu i time uzrokovanog porasta šuma (engl. random telegraph signal noise, RTS) u pojedinim pikselima. Osim toga, rasipanje praga detekcije unutar matrice je znatno veće od simuliranih vrijednosti, što u kombinaciji s RTS šumom ograničava prag detekcije na iznad  $200 e^-$ . U testiranjima zrakom čestica zaključuje se da uz najniže moguće pragove detekcije senzor prije zračenja postiže visoku efikasnost detekcije od preko 97%, uniformnu po cijeloj površini piksela.

Nakon ozračenja neutronima do  $10^{15} n_{eq}/cm^2$  i x-zrakama do 70 Mrad, analogni i digitalni sklopovi su i dalje funkcionalni, uz nešto veći šum i rasipanje praga detekcije. Pojačanje ulaznog sklopa ne razlikuje se od onog prije zračenja zahvaljujući topologiji otpornoj na ionizirajuće zračenje. Međutim, testiranja zrakom čestica pokazuju znatan pad efikasnosti detekcije pri rubovima piksela, daleko od sakupljačke elektrode. Iako je senzor u modificiranom procesu potpuno osiromašen, gubitak efikasnosti povezan je s manjkom lateralnog električnog polja pri rubovima piksela, što dovodi do zarobljavanja nosilaca u zamkama uzrokovanim neionizirajućim zračenjem i do gubitka signala. Zbog toga maksimalna srednja efikasnost unutar piksela uz najniže dostižne pragove detekcije iznosi tek oko 80%.

Kako bi se poboljšala efikasnost detekcije nakon zračenja, pomoću TCAD simulacija razvijene su nove procesne promjene s ciljem povećanja lateralnog električnog polja. Pokazuje se da se uvođenjem dodatne duboke implantacije p-tipa ili uvođenjem razmaka u postojeću implantaciju n-tipa pri rubovima piksela električno polje te samim time nosioci bolje usmjeravaju prema sakupljačkoj elektrodi, te da je ukupni sakupljeni naboj nakon zračenja znatno veći. Zbog toga započinje projektiranje nove, manje verzije MALTA čipa s ovim procesnim promjenama, nazvane miniMALTA. Osim procesnih promjena, unutar matrice piksela povećane su dimenzije kritičnih tranzistora kako bi se suzbio RTS šum i dobilo veće pojačanje. Na periferiji čipa projektirana je i nova generacija digitalnog sklopovlja za očitavanje, koja sinkronizira asinkrone signale iz matrice i olakšava daljnje procesiranje podataka, zadržavajući pritom nisku digitalnu potrošnju snage. Sklop za sinkronizaciju temelji se na polju RAM memorijskih ćelija u koje se pohranjuje informacija o adresi piksela i vremenu detekcije. RAM memorija se zatim sinkrono očitava te se informacija sinkrono šalje s čipa.

Prvi rezultati mjerenja na ulaznom pojačalu novog miniMALTA čipa pokazuju znatno veće pojačanje zbog većeg izlaznog otpora na izlaznom čvoru pojačala, što znači da se uz iste postavke pojačala mogu postići niži pragovi detekcije. Osim toga, povećanje dimenzija tranzistora gotovo u potpunosti eliminira RTS šum čak i nakon ozračenja, što ponovno znači da je lakše postići niže pragove. Sklopovlje za sinkronizaciju također se pokazalo potpuno funkcionalnim te je moguće očitati točnu adresnu i vremensku informaciju pri svakoj detekciji. U testiranjima zrakom čestica prije zračenja, sektori čipa u kojima su implementirane procesne promjene uz niski prag detekcije od ispod  $200 e^-$  pokazuju efikasnost od preko 99%. Nakon ozračenja do  $10^{15} n_{eq}/cm^2$ , efikasnost u tim sektorima još uvijek iznosi oko 98%, što znači da povećanje lateralnog električnog polja uz niski prag detekcije dovodi to gotovo potpune efikasnosti detekcije čak i nakon zahtijevanih doza zračenja.

Nakon ovih rezultata, nastavlja se projektiranje sljedećih verzija velikih detektora u Tower-Jazz 180 nm tehnologiji. Dodatna poboljšanja ulaznih sklopova omogućit će još veće pojačanje i niži prag detekcije, a unutar svakog piksela dodano je i sklopovlje za podešavanje praga detekcije, čime će se smanjiti rasipanje praga unutar velike matrice. Uz smanjenje dimenzija piksela na oko 33  $\mu m$ , to bi trebalo dovesti do još više efikasnosti i još bolje otpornosti na zračenje. Poboljšanja će biti uključena u dva velika detektora s različitim vrstama digitalnih sklopova za očitavanje, koji će biti poslani na proizvodnju krajem 2019.

**Ključne riječi:** Aktivni piksel senzori, CMOS integrirani sklopovi, detektori čestica osjetljivi na položaj, efekti zračenja, otpornost (elektronike) na zračenje, poluvodički detektori, projektiranje poluvodičkih sklopova

# Contents

<b>1. Introduction</b>	1
1.1. Detectors in the high-energy physics experiments at CERN	1
1.2. Pixel detectors for the LHC High-Luminosity upgrade	6
<b>2. CMOS monolithic active pixel sensors</b>	10
2.1. Detection of particles in silicon	10
2.1.1. Energy loss of charged particles	10
2.1.2. Signal formation in the sensor	13
2.2. Radiation effects in the sensor – Non-ionising energy loss	16
2.3. Monolithic sensor concepts	19
2.3.1. Small collection electrode designs	19
2.3.2. Large collection electrode designs	21
2.3.3. Other approaches - DEPFET and SOI	22
2.4. Radiation effects in the electronics – Total ionising dose and single event effects	22
2.5. Front-end and readout concepts	25
<b>3. Design and characterisation of radiation-hard CMOS sensors</b>	30
3.1. Sensor technology	30
3.1.1. The standard TowerJazz 180 nm process	30
3.1.2. Designs in the modified TowerJazz process	31
3.2. Analogue front-end circuit	36
3.2.1. Principle of operation	36
3.2.2. Timing optimisation	40
3.2.3. Noise and mismatch	43
3.2.4. Considerations for radiation hardness	46
3.2.5. Bias generation using digital-to-analogue converters	46
3.3. Digital readout electronics	49
3.3.1. Asynchronous matrix readout	49
3.3.2. End-of-column readout logic	54

3.4.	Sensor characterisation before irradiation . . . . .	57
3.4.1.	Sensor and analogue performance in lab tests . . . . .	57
3.4.2.	Measurements on readout architecture . . . . .	62
3.4.3.	Beam test results . . . . .	68
3.5.	Performance of irradiated sensors . . . . .	70
3.5.1.	Sensor and front-end after irradiation . . . . .	70
3.5.2.	Efficiency in beam tests . . . . .	74
<b>4.</b>	<b>Optimisation of pixel matrix and readout electronics . . . . .</b>	<b>78</b>
4.1.	Process improvements for radiation hardness . . . . .	78
4.2.	Pixel matrix design changes . . . . .	80
4.3.	Synchronisation at the end-of-column . . . . .	81
4.3.1.	Random-access memory for synchronisation . . . . .	81
4.3.2.	Peripheral readout logic . . . . .	83
4.4.	Test results before and after irradiation . . . . .	85
<b>5.</b>	<b>Outlook for future design improvements . . . . .</b>	<b>100</b>
5.1.	Further optimisation of analogue front-end circuitry . . . . .	100
5.2.	In-pixel threshold tuning . . . . .	103
<b>6.</b>	<b>Conclusion . . . . .</b>	<b>107</b>
	<b>Bibliography . . . . .</b>	<b>109</b>
	<b>Biography . . . . .</b>	<b>117</b>
	<b>Životopis . . . . .</b>	<b>120</b>

# Chapter 1

## Introduction

### 1.1 Detectors in the high-energy physics experiments at CERN

The search for new physics at the Large Hadron Collider (LHC) at the European Organisation for Nuclear Research (CERN) relies on the detection of particles created in proton-proton and heavy ion collisions. Protons in two counter-rotating beams are accelerated through a complex of accelerators, shown in fig. 1.1 [1], reaching a beam energy of up to 6.5 TeV in the largest collider ring, the 27 km circumference LHC. Protons are produced by ionising hydrogen gas with an electric field. The kinetic energy of the protons is increased from about 100 keV up to 1.4 GeV in a linear accelerator (LINAC) using radio-frequency cavities and the Proton Synchrotron Booster (PSB) before being injected into the Proton Synchrotron (PS). The PS and the SPS (Super Proton Synchrotron) accelerate the protons to 25 GeV and 450 GeV, respectively, before the beams are finally injected into the LHC for further acceleration, from 450 GeV to 6.5 TeV per beam.

Superconducting magnets cooled to temperatures below 2 K and operating at magnetic field strengths above 8 T are used to bend the particles in the beam around the circular collider. The beams collide at four crossing points around which the four largest experiments, ATLAS [2], CMS [3], ALICE [4] and LHCb [5] are positioned. The number of events per second generated in the LHC collisions is given by:

$$N = L\sigma, \quad (1.1)$$

where  $\sigma$  is the cross-section for the event in question and  $L$  is the machine luminosity.  $L$  is defined only by the beam parameters and can be written as:

$$L = \frac{N_b^2 n_b f_{rev} \gamma_r}{4\pi \epsilon_n \beta_*} F, \quad (1.2)$$

where  $N_b$  is the number of particles per bunch,  $n_b$  the number of bunches per beam,  $f_{rev}$  the

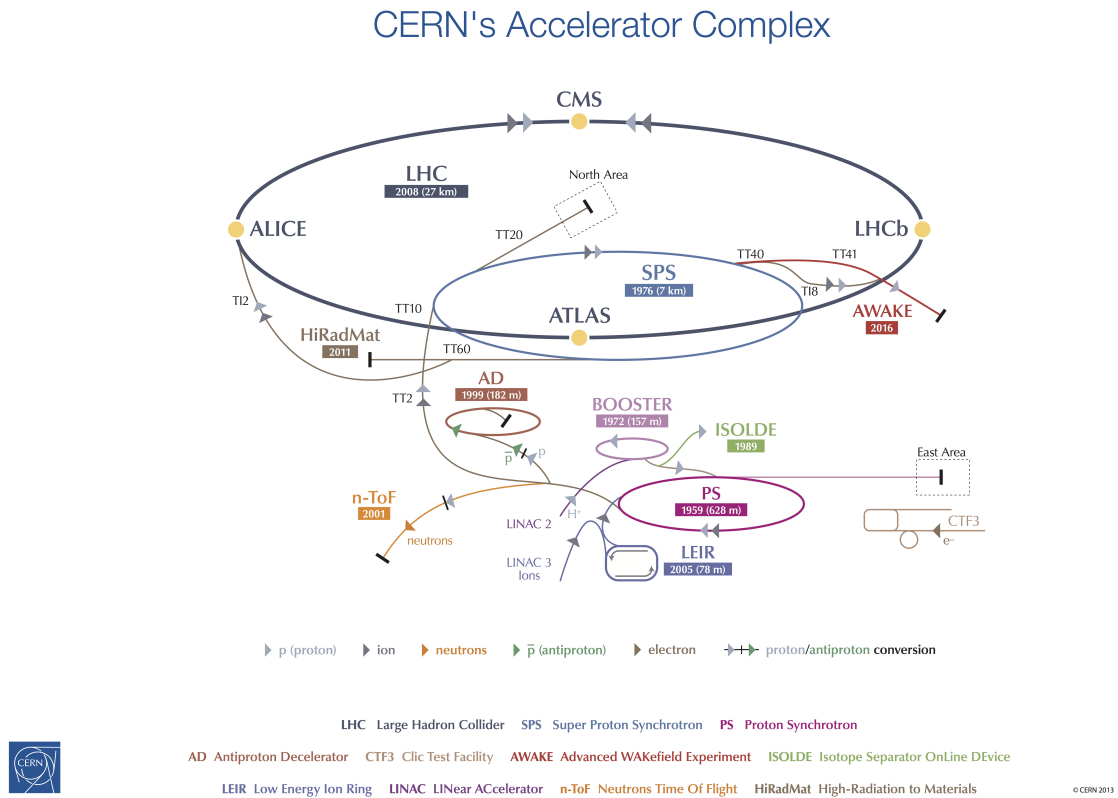


**Figure 1.1:** An overview of the accelerator complex at CERN and the experiments within it (reproduced from [1]).

revolution frequency,  $\gamma_f$  the relativistic gamma factor,  $\varepsilon_n$  the normalised transverse beam emittance,  $b_*$  the beta function at the collision point, and  $F$  the geometric luminosity reduction factor due to the crossing angle at the interaction point [6]. Since the interesting physics events (such as decays of the elusive Higgs boson) are very rare, the study and exploration of these events in the LHC collisions requires both high beam energies and high beam intensities. The two largest general-purpose experiments, ATLAS and CMS, operate with a peak luminosity of about  $L = 10^{34} \text{ cm}^{-2}\text{s}^{-1}$  for proton collisions, while the one dedicated ion experiment, ALICE, aims at a peak luminosity of  $L = 10^{27} \text{ cm}^{-2}\text{s}^{-1}$  for nominal lead-lead ion operation. Rather than having continuous beams, the protons are bunched together so that interactions between the two beams take place at discrete intervals, 25 ns apart, providing a bunch collision rate of 40 MHz. The particles created in these collisions as well as the decay products of particles with a short lifetime pass through a variety of detectors within the experiments, which provide information about the charge, momentum and energy of the created particles.

An overview of the detector systems will be given through the example of the ATLAS experiment, illustrated in fig. 1.2. The experiment consists of a series of detectors placed in concentric cylinders around the interaction point where the proton beams from the LHC collide. It can be divided into four major parts: the Inner Detector, the calorimeters, the Muon



Spectrometer and the magnet systems [7]. The two large superconducting magnet systems are used to bend charged particles so that their momenta can be measured. The inner solenoid magnet produces a uniform 2 T magnetic field surrounding the Inner Detector, while the outer toroidal magnetic field surrounds the calorimeters and the muon system.

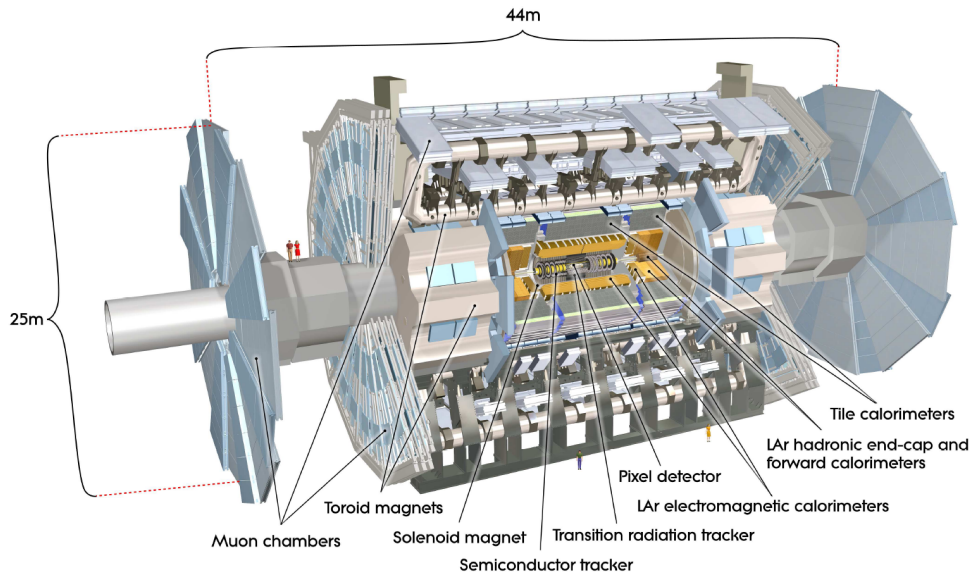


**Figure 1.2:** A cut-away view of the ATLAS experiment and its sub-parts (reproduced from [2]).

The Inner Detector itself consists of high-resolution semiconductor pixel and strip detectors in the inner part of the tracking volume, as well as straw-tube tracking detectors with the capability to generate and detect transition radiation in its outer part. The innermost pixel layer begins about 5 cm from the proton beam axis, and the Inner Detector extends to a radius of 1.2 metres as well as 6.2 metres in length along the beam pipe. Its basic function is to track charged particles by detecting their interaction with material at discrete points. The curvature of the particles' track due to the magnetic field present reveals the charge and momentum of the particles. Apart from track reconstruction, the precision tracking detectors, i.e. the pixels and semiconductor trackers (SCT), need to be able to reconstruct the interaction point of the particles from the beam (primary vertices) as well as the decay points of short-lived particles (secondary vertices) with a high resolution. This is achieved by a high granularity in the two-dimensionally segmented silicon pixel detectors used around the vertex region. The high granularity in the order 100  $\mu\text{m}$  over such a large area means that the number of readout channels in the Pixel Detector itself is very high, over 80 million, which is about 50% of the total readout channels of the whole experiment. The total of nearly 1750 pixel modules are arranged in three layers around the beam axis in the barrel region and on three disks perpendicular to the beam axis in the end-cap regions. The pixels in the barrel region provide a spatial resolution of around 10  $\mu\text{m}$  in the direction radial to the beam axis and 70  $\mu\text{m}$  in the direction along the beam axis for the impact parameter, as well as around 50  $\mu\text{m}$  in the radial direction for the reconstruction of

secondary vertices. The impact parameter is defined as the perpendicular distance of the closest approach of a reconstructed track to the primary vertex.

The Semiconductor Tracker (SCT) is the middle component of the Inner Detector and has a similar function to the Pixel Detector, but with long, narrow strips rather than small pixels, making coverage of a larger area more practical. The SCT is critical for the tracking in the plane perpendicular to the beam, since it measures particles over a much larger area than the Pixel Detector, with more sampled points and similar, albeit one-dimensional accuracy. The total number of readout channels in the SCT is approximately 6.3 million. The Transition Radiation Tracker (TRT) is the outermost component of the Inner Detector and is composed of drift tubes (straws), each 4 mm in diameter and up to 144 cm long. The TRT only provides information about the radial position, for which it has an intrinsic accuracy of 130  $\mu\text{m}$  per straw. Each straw is filled with gas that becomes ionised when a charged particle passes through, producing a current pulse in the wire. The pattern of "hit" straws allow the path of the particle to be determined. Ultra-relativistic charged particles produce transition radiation in the material between the straws, resulting in a much stronger signals in some straws and allowing the identification of the lightest charged particles, electrons and positrons. The total number of TRT readout channels is approximately 351 thousand. The expected transverse momentum resolution obtained with the complete Inner Detector is [8]:

$$\frac{\sigma_{pT}}{pT} = 0.03\% pT \text{ (GeV)} + 1.2\%. \quad (1.3)$$

The calorimeters are situated outside the solenoidal magnet that surrounds the Inner Detector. Their purpose is to measure the energy of particles by absorbing it. There are two basic calorimeter systems: an inner Electromagnetic Calorimeter and an outer Hadronic Calorimeter. Both are sampling calorimeters: they absorb energy in high-density metal and periodically sample the shape of the resulting particle shower, inferring the energy of the original particle from this measurement. The Electromagnetic (EM) Calorimeter absorbs energy from particles that interact electromagnetically, and its fine granularity and energy resolution are ideally suited for precision measurements on electrons and photons. The energy-absorbing materials are lead and steel, while liquid argon (LAr) is used as the sampling material. The Hadron Calorimeter absorbs energy from particles that pass through the EM Calorimeter, primarily hadrons. The main part of this calorimeter is the tile calorimeter placed directly outside the EM calorimeter envelope. The energy-absorbing material is steel, with scintillating tiles that sample the energy deposited. The coarser granularity of this part of the calorimeter is sufficient to satisfy the physics requirements. In the end-cap regions, the end-cap and forward calorimeters made of liquid argon, copper and tungsten complete the calorimeter system.

The Muon Spectrometer is a large tracking system designed to accurately measure the momentum of muons, which pass through all the other elements of the detector before reaching the

muon systems. It is based on the magnetic deflection of muon tracks in the large superconducting air-core toroid magnets, instrumented with separate high-precision tracking chambers and triggering chambers with a high time resolution. The precise measurement of the track coordinates in the principal bending direction of the magnetic field is provided by Monitored Drift Tubes (MDTs) and Cathode Strip Chamber (CSCs). The trigger chambers, made of Resistive Plate Chambers (RPCs) and Thin Gap Chambers (TGCs) provide bunch-crossing identification and measure the muon coordinate in the direction orthogonal to that determined by the precision-tracking chambers. In the barrel region, tracks are measured in chambers arranged in three cylindrical layers around the beam axis; in the transition and end-cap regions, the chambers are installed in planes perpendicular to the beam, also in three layers.

The principle of detecting different types of particles in the experiment is reiterated in fig. 1.3. Charged particles are tracked precisely within the Pixel/SCT Detectors and Transition Radiation Tracker of the Inner Detector and then absorbed in either the Electromagnetic or the Hadronic Calorimeter for energy measurement. Muons, which pass through all the other detector systems, are tracked in the Muon Spectrometer. Neutrinos are the only established stable particles that cannot be detected directly, and their presence is inferred by measuring a momentum imbalance among detected particles.

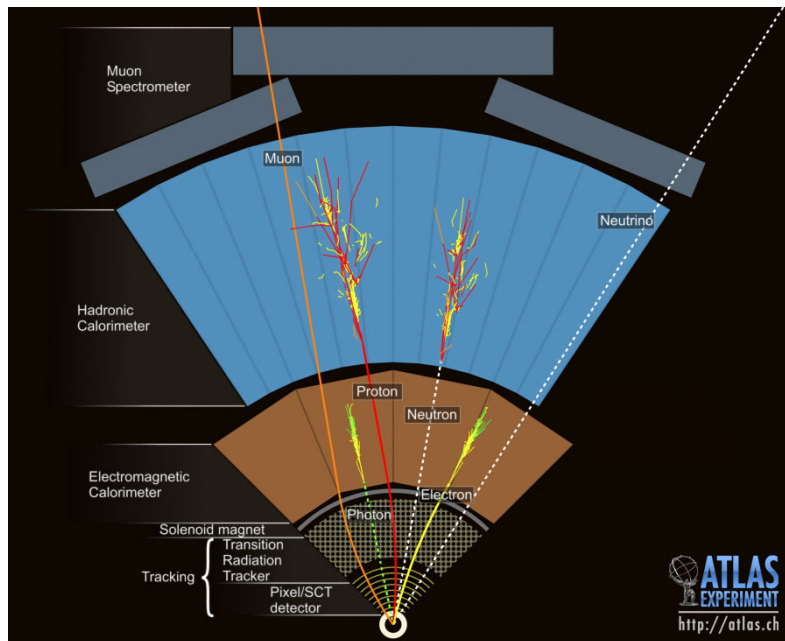


**Figure 1.3:** A cross-section through the various layers of detectors used in the ATLAS experiment.

The other large general-purpose detector, CMS, uses the same principles in particle detection, and is composed of an all-silicon tracker, an electromagnetic and hadronic calorimeter as well as a muon system. The principal difference between the two experiments is the magnet system, where CMS uses a single solenoid to generate the 4 T magnetic field penetrating all the detector layers.

## 1.2 Pixel detectors for the LHC High-Luminosity upgrade

After 2020, the statistical gain in running the accelerator without a significant luminosity increase beyond its design value will become marginal. Therefore, to maintain scientific progress and to explore its full capacity, the LHC will undergo a major upgrade during the long shut-down planned between 2023 and 2025 [9]. The timeline of the upgrade plans is shown in fig. 1.4. After 2025, the peak luminosity will be increased to more than  $5 \times 10^{34} \text{ cm}^{-2}\text{s}^{-1}$ , which is a factor of 5-7 higher than the current design value. When integrating the luminosity over the full operation time of the machine, this gives an integrated luminosity value of  $3000 \text{ fb}^{-1}$  that can be reached until 2035. This integrated luminosity is about ten times the expected luminosity reach of the first twelve years of the LHC lifetime. To cope with such an increase in luminosity, a number of systems related to the superconducting magnets, cryogenics and beam collimation will need to be upgraded. A number of detector systems will need to be upgraded as well, since the increased particle fluxes will result in higher detector occupancies and efficiency losses due to readout limitations at high hit rates. Another limitation is the increase in radiation damage over the full lifetime of the detectors, especially in the pixel detectors closest to the particle interaction points.

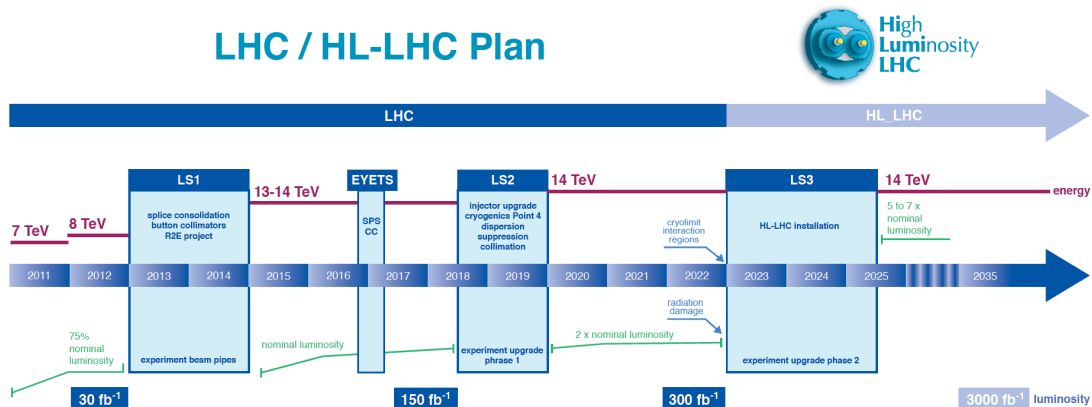


**Figure 1.4:** Timeline of the upgrade plans for the LHC. After the third long shut-down (LS3), the machine will be in the High-Luminosity configuration (reproduced from [9]).

The three-layer pixel system of the ATLAS detector, designed for an instantaneous luminosity of  $10^{34} \text{ cm}^{-2}\text{s}^{-1}$ , was already upgraded during the long shut-down in 2013-2014 (LS1) to cope with the gradually increasing luminosity until the LS3 upgrade. In order to retain the excellent secondary vertex reconstruction efficiency in the presence of high pile-up, a fourth pixel detector layer, called the Insertable B-Layer (IBL), was installed inside the three-layer pixel detector, about 3.3 cm from the beam line. As a result, the impact parameter resolution improved by nearly a factor of 2 for low transverse momentum tracks [10]. For the high-luminosity upgrade during LS3, the Inner Detector will be replaced by an all-silicon Inner Tracker (ITk) consisting of five layers of pixel and four layers of strip detectors [11].

Currently, all the experiments at the LHC use hybrid pixel detectors for the tracking of particles in the innermost layers. In this type of detector, the sensor part is produced on dedicated sensor grade silicon material, while the separate pixel readout chip is manufactured using a standard CMOS process. The traversing particle generates a signal in the sensor part, which is read out by the readout chip attached to the sensor by using the flip-chip bump-bonding technology. The readout cells are arranged in the same two-dimensional matrix structure of the pixel cells of the sensor, as shown in fig. 1.5a. A pixel unit cell of the sensor part together with the readout cell and the connecting solder bump is shown in fig. 1.5b.

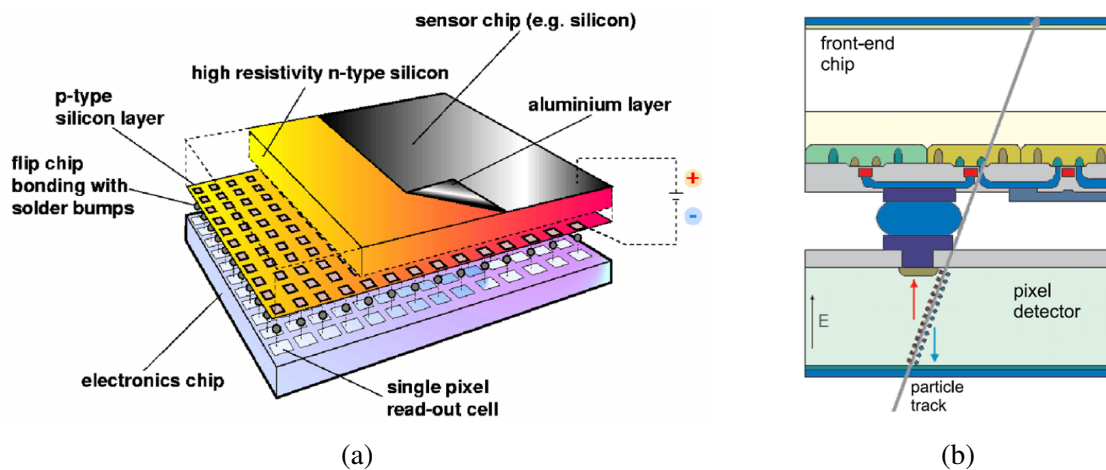


**Figure 1.5:** (a) A cut-away view and (b) one pixel cell of a hybrid pixel detector. The sensor chip is bump-bonded to the readout chip containing the electronics (reproduced from [12] and [13]).

The large signals collected from the sensor chip optimised for a high-radiation environment combined with the sophisticated analogue and digital functionality provided by the readout chip designed in technologies with small feature sizes results in a superior signal-to-noise ratio as well as comprehensive in-pixel signal processing, rendering the hybrid pixel detector principle the state-of-the-art technology for today's precision vertex detectors in particle physics [13]. Further advantages of hybrid pixels are high rate capability and large radiation tolerance while maintaining a very good spatial resolution.

The three layers of the current ATLAS Pixel Detector utilise planar sensors composed of an array of diodes placed on a low-doped n-type bulk bump-bonded to FE-I3 readout chips [14]. These chips were designed and fabricated in a commercial 250 nm technology and contain a matrix of  $18 \times 160$  pixels with a pixel size of  $50 \times 400 \mu\text{m}^2$ . Each chip contains 2880 readout channels with densely packed analogue and digital circuits, and uses radiation tolerant layout rules. On the other hand, the IBL modules use the FE-I4 readout chip [15], an evolution of the FE-I3 designed to cope with the high hit rates very close to the interaction point. The chip was fabricated in the IBM 130 nm technology that allows a high digital design density and radiation tolerance. The pixel array consists of  $80 \times 336$  pixels with a size of  $50 \times 250 \mu\text{m}^2$ . These are bump-bonded to planar silicon sensors in one type of modules or 3D silicon sensors in the other

type. The 3D sensors, where the electrodes fully penetrate the silicon substrate, were included for the first time in a large-scale collider experiment to provide superior radiation hardness close to the interaction point.

Despite good performance in the experiments thus far, the hybrid approach does have its disadvantages. The module assembly using the bumping and flip-chip technology is a complex process that drives the cost for large area detectors. The pixel pitches that are easily achievable are still rather large, in the order of 100  $\mu\text{m}$ . Moreover, the power consumption and hence the needed cooling power is high, resulting in a large material budget for large detector systems. This deteriorates the momentum and vertex measurement resolution due to the scattering of particles in the material.

To overcome these drawbacks, the next generation of R&D focuses on the development of monolithic active pixel sensors (MAPS). These detectors integrate the sensor and the read-out electronics inside the same silicon die, thus completely avoiding bump-bonding. CMOS monolithic active pixel sensors can be produced using commercial CMOS processes and can therefore be very cost effective. Moreover, the extremely low sensor capacitance that can be achieved with this approach allows lower power consumption compared to their hybrid counterparts, as described in the following chapters, which reduces the material budget and limits the probability for the particles to be scattered. So far, radiation hardness has been the main disadvantage of CMOS MAPS. However, recent developments in CMOS sensor processing, also detailed later on, carry the promise of improving the radiation hardness and making MAPS a promising technology even for the most extreme radiation environments, such as the pixel layers of the ATLAS experiment. Therefore, MAPS are being proposed as an alternative to hybrid pixel detectors in the outer pixel layers of the upgraded Inner Tracker, where the cost advantage would be significant due to the large areas that need to be covered.

The monolithic sensors described in this thesis were designed with the aim to meet the requirements of the outermost, fifth pixel layer in the ATLAS ITk. The performance figures in terms of particle rates, timing and radiation hardness after the high-luminosity upgrade are comparable to those for the innermost layer currently installed in the experiment. The main requirements are summarised in table 1.1. A detection efficiency higher than 97% at the end-of-life of the detector is required, with a time resolution of 25 ns in order to separate particles from different bunch crossings. Because of the high particle hit rates in the order of 1 MHz/mm<sup>2</sup>, the detectors need to be able to process large amounts of data in a short time period. The massive data processing inside the detector leads to high power consumption and puts a high demand on power delivery and cooling, which involves large mechanical constructions and an increase in material budget. Still, the total power consumption needs to remain below 500 mW/cm<sup>2</sup> in order to limit the total material budget at 2% of  $x/X_0$  (where  $X_0$  is the radiation length of the material, i.e. the mean path length over which a high-energy electron loses all but 1/e of

its energy). The ITk also introduces unprecedented radiation levels in terms of ionising dose (>50 Mrad even for the outermost layer during the detector lifetime) and non-ionising particle fluence (> $10^{15}$  1 MeV  $n_{\text{eq}}/\text{cm}^2$  for the outermost layer), which will be discussed in detail in the next chapter. A safety factor of 1.5 is often added on top of the reported values for radiation tolerance.

**Table 1.1:** Main performance requirements for the outermost pixel layer of the ATLAS ITk.

Requirement	Unit	Value
Detection efficiency	%	> 97
Time resolution	ns	25
Particle rate	MHz/mm <sup>2</sup>	1
Non-ionising radiation fluence	1 MeV $n_{\text{eq}}/\text{cm}^2$	$10^{15}$
Ionising radiation dose	Mrad	50
Power consumption	mW/cm <sup>2</sup>	< 500
Material budget	% of $x/X_0$	< 2

To achieve the desired tracking resolution, a small pixel size in the order of  $50 \times 50 \mu\text{m}^2$  is required, which can easily be achieved with the monolithic pixels described later on. In the case of a binary readout, where only the pattern of hit pixels is known, the position resolution of a detector  $\sigma_p$  has a direct dependence on the pixel size  $p$ . If only a single pixel registers a crossing particle, the position resolution is given by:

$$\sigma_p = \frac{p}{\sqrt{12}}. \quad (1.4)$$

The position resolution is improved in the case when several adjacent pixels register a hit, their number and topology depending on the impact position of the ionising particle [16]. A further improvement of the position resolution can be obtained by having analogue information about the signal generated in each pixel, in which case a center of gravity algorithm can be used for the reconstruction of the impact position.

# Chapter 2

## CMOS monolithic active pixel sensors

### 2.1 Detection of particles in silicon

The basic detection mechanism of silicon detectors is the generation and movement of mobile charges (electrons and holes) in a silicon p-n junction [17]. The number of ionised charges depends on the energy loss of the traversing particle within the material, which is described in the following section. The average number of electron-hole pairs generated by a constant amount of absorbed energy can be obtained by dividing the energy  $E$  by the average energy needed to produce an electron-hole pair,  $w$ :

$$N = \frac{E}{w} \quad (2.1)$$

In silicon,  $w = 3.6$  eV, which is more than three times the bandgap of 1.12 eV. The difference in energy is used to generate phonons, and since the fraction of energy used to generate e-h pairs and phonons is subject to fluctuations,  $N$  will vary by:

$$\langle \Delta N^2 \rangle = FN = F \frac{E}{w} \quad (2.2)$$

$F$  is the so-called Fano factor [18], which is in the order of 0.1 for most semiconductors and provides the ultimate limit of energy resolution in semiconductor detectors.

#### 2.1.1 Energy loss of charged particles

Moderately relativistic charged particles other than electrons lose energy in matter primarily by ionisation and atomic excitation [19]. The mean rate of energy loss (or stopping power) is given by the Bethe-Bloch equation,

$$-\frac{dE}{dx} = K_z^2 \frac{Z}{A} \frac{1}{\beta^2} \left[ \frac{1}{2} \ln \frac{2m_e c^2 \beta^2 \gamma^2 T_{max}}{I^2} - \beta^2 - \frac{\delta}{2} \right], \quad (2.3)$$



where  $z$  is the charge number of the incident particle,  $Z$  the atomic number of the absorber,  $A$  the atomic mass of the absorber,  $m_e$  the electron mass,  $c$  the speed of light,  $T_{max}$  the maximum kinetic energy which can be imparted to a free electron in a single collision,  $I$  the mean excitation energy,  $\delta$  the density-effect correction factor described in [20], and  $\beta$ ,  $\gamma$  and  $K$  are defined as follows:

$$\beta = \frac{v}{c}, \quad (2.4)$$

$$\gamma = \frac{1}{\sqrt{1 - \frac{v^2}{c^2}}}, \quad (2.5)$$

$$K = 4\pi N_A r_e^2 m_e c^2. \quad (2.6)$$

Here,  $v$  is the velocity of the incident particle,  $N_A$  is Avogadro's number and  $r_e$  the classical electron radius. With  $A$  in  $\text{g mol}^{-1}$  the units are  $\text{MeV g}^{-1} \text{cm}^2$ . An example of the stopping power for positive muons in copper as a function of momentum is shown in fig. 2.1.

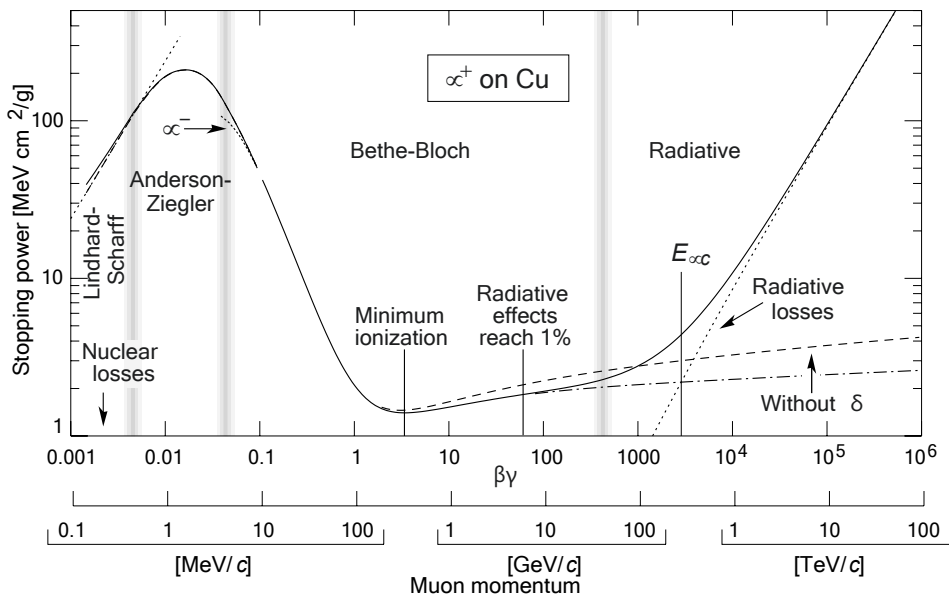


**Figure 2.1:** Stopping power ( $-dE/dx$ ) for positive muons in copper as a function of momentum (reproduced from [19]).

At lower energies (and lower momenta) various corrections have to be applied, while at higher energies radiative effects become important. In practice, most relativistic particles have mean energy loss rates close to the minimum, and are said to be minimum ionising particles (MIPs). However, the mean energy loss per unit absorber thickness given by the Bethe-Bloch equation is subject to statistical fluctuations because of the stochastic nature of the energy losses. The probability density function describing the distribution of energy loss  $\Delta$  in an absorber

thickness  $x$  is called the Landau distribution [21]. This probability density function  $f(\Delta/x)$  for 500 MeV pions in silicon of different thicknesses, normalised to 1 at the most probable value (MPV)  $\Delta_p/x$ , is shown in fig. 2.2. Note that the most probable energy loss is below the mean energy loss predicted by the Bethe-Bloch equation due to the long tail in the distribution (the weight of few high-loss events). It can also be observed that the most probable value decreases with decreasing silicon thickness, and for very thin layers the energy loss distributions are not well described by the classical Landau function, so other models are used [22].

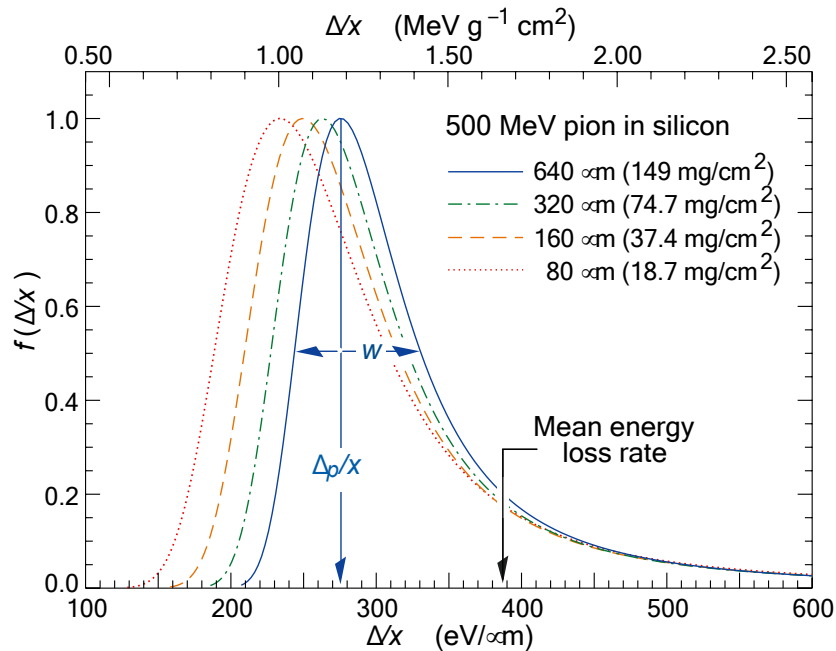


**Figure 2.2:** Normalised distribution of energy loss for 500 MeV pions in silicon of different thicknesses (reproduced from [19]).

Energy loss by electrons and positrons differs from loss by heavy particles because of the kinematics, spin, and the interaction of the incident electron with the electrons it ionises. At low energies, electrons lose energy mainly by ionisation, but the parameter  $I$  in the Bethe-Bloch equation needs to be modified based on a combination of experimental data and theoretical considerations [23]. At high energies (typically above a critical energy of a few tens of MeV in most materials), bremsstrahlung, i.e. radiation produced by the deceleration of electrons when deflected by the nuclei, becomes the dominant energy loss mechanism. The mean distance over which a high energy electron loses all but  $1/e$  of its energy by bremsstrahlung is defined as the radiation length  $X_0$ , which has been calculated and tabulated for different elements [24].

When a charged particle traverses a medium, it is deflected by many small-angle scatters, primarily caused by the Coulomb interaction between the particle and the nuclei. The scattering angle when leaving the material after a large number of interactions follows roughly a Gaussian

distribution with a root-mean-square (RMS) value of:

$$\theta_{plane}^{RMS} = \frac{13.6 \text{ MeV}}{\beta pc} z \sqrt{\frac{x}{X_0}} \left[ 1 + 0.038 \ln \frac{x}{X_0} \right], \quad (2.7)$$

where the angle  $\theta$  is expressed in rad, the particle momentum  $p$  in MeV. As mentioned earlier, this multiple scattering will have an impact on the position resolution of a silicon detector composed of multiple layers.

### 2.1.2 Signal formation in the sensor

In practically all silicon particle detectors, the basic building block of the sensor is a reverse-biased p-n junction. At the transition between the n-type and the p-type material, majority carriers from one side diffuse to the other side and recombine with the majority carriers producing a region depleted of free carriers [26]. The space charge in this depletion region causes an electric field to build up across the junction, as shown in fig. 2.3. The potential difference on

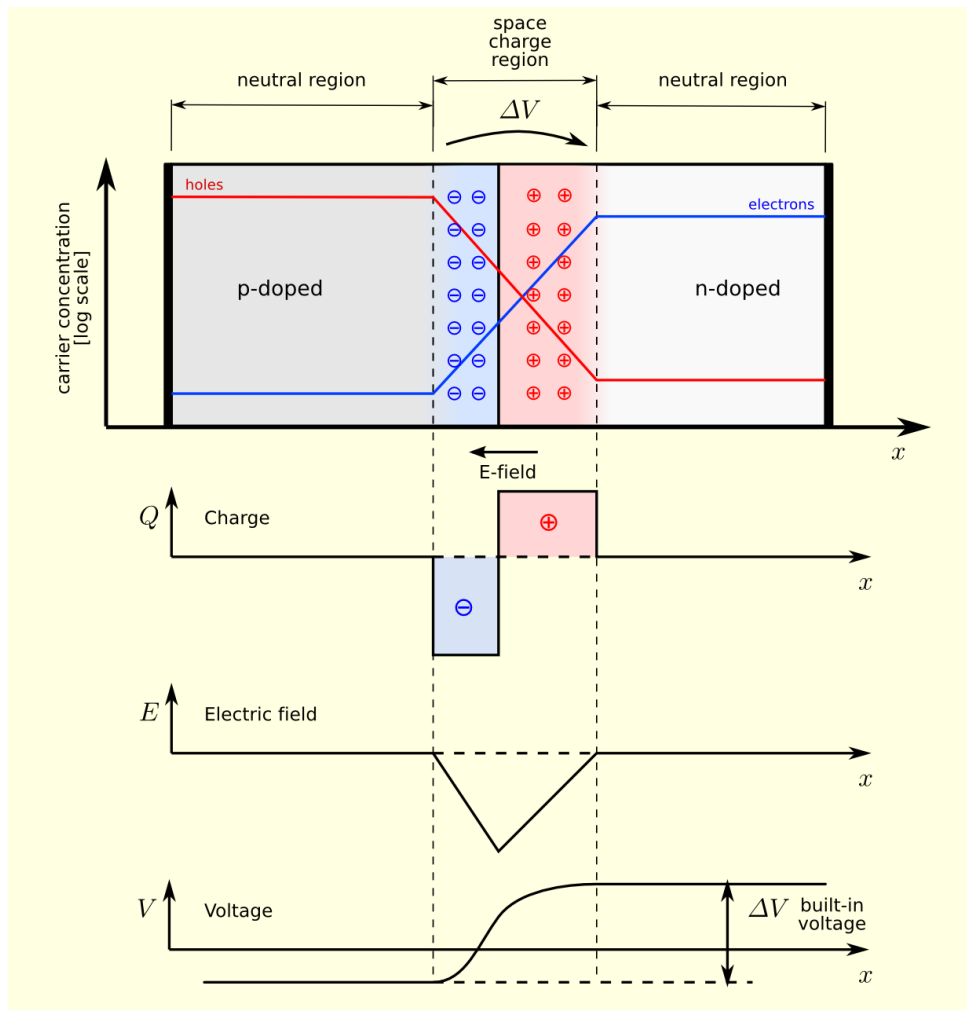


**Figure 2.3:** A p-n junction in thermal equilibrium with zero bias voltage applied. Plots for the charge density, the electric field, and the voltage are also reported (reproduced from [25]).

the two sides can be described by the so-called built-in voltage  $V_{bi}$  ( $\Delta V$  in fig. 2.3), which for an abrupt p-n junction in thermal equilibrium is given by:

$$V_{bi} = \frac{kT}{e} \ln \left( \frac{n_{0n} p_{0p}}{n_i^2} \right) \approx \frac{kT}{e} \ln \left( \frac{N_D N_A}{n_i^2} \right), \quad (2.8)$$

where  $n_{0n}$  and  $p_{0p}$  are the majority carrier concentrations on both sides, and in the case of complete ionisation they can be approximated by the donor and acceptor concentrations,  $N_D$  and  $N_A$ , respectively.  $k$  is the Boltzmann constant,  $T$  the temperature and  $e$  is the electron charge, while  $n_i$  is the intrinsic carrier concentration in silicon.

By applying a reverse bias  $V$  over the junction in addition to the built-in voltage, one can further remove majority carriers from each side and extend the depletion region. By solving the one dimensional Poisson equation, the width of the depletion region for a planar junction is obtained as the sum of the depletion region width on both sides:

$$W = x_n + x_p = \sqrt{\frac{2\epsilon_0\epsilon_{Si}}{e} \left( \frac{1}{N_D} + \frac{1}{N_A} \right) (V + V_{bi})}. \quad (2.9)$$

By assuming a reverse bias voltage significantly higher than the built-in voltage and a p-n junction with the n-side much more heavily doped than the p-side, this simplifies to:

$$W = \sqrt{\frac{2\epsilon_0\epsilon_{Si}}{eN_A} V}, \quad (2.10)$$

which is an expression widely used to calculate the depletion depth. In this case, the maximum electric field can be obtained as follows:

$$E_{max} = \frac{2V}{W} = \sqrt{\frac{2eN_A}{\epsilon_0\epsilon_{Si}}} V. \quad (2.11)$$

The resistivity  $\rho$  of a semiconductor is approximately inversely proportional to the doping concentration  $N_A$ , so from eq. 2.10 one can obtain:

$$W \sim \sqrt{\rho V}. \quad (2.12)$$

From these equations, it is obvious that applying a high reverse bias voltage will result in a wider depletion region and higher electric field, while having a lowly doped junction (high resistivity) also helps to increase the depletion region.

The reverse-biased p-n junction also constitutes a capacitance  $C$ . For a planar junction, this capacitance can be estimated using the well known formula for a parallel-plate capacitor:

$$C = \epsilon_0\epsilon_{Si} \frac{A}{d}, \quad (2.13)$$

where  $A$  is the area of the junction and  $d$  is to be replaced by the width of the depletion region. It

is important to note that a smaller junction area and a wider depletion region leads to a decrease in the sensor capacitance, which has a significant impact on the timing and noise performance of the detector, as will be discussed later on.

In the absence of radiation, a steady current still flows in a reverse-biased p-n junction. This so-called leakage current stems from the diffusion of carriers from undepleted areas into the depletion region as well as thermal carrier generation within the depletion region. The thermal generation current depends on the depletion volume and is often the dominant leakage current component. It can be calculated as:

$$J_{vol} \approx -e \frac{n_i}{\tau_g} W, \quad (2.14)$$

with  $J_{vol}$  being the volume leakage current per unit area and  $\tau_g$  the carrier generation lifetime. This current has an impact on the operating point of the electronics following the sensor (as discussed in later sections). Since it has an exponential temperature dependence (due to the temperature dependence of  $n_i$  and  $\tau_g$ ), a common way to minimise it and limit the influence on the detector is to operate the sensors at low temperature.

If the reverse bias is increased to sufficiently high values, there is a sharp increase in current referred to as breakdown. This is usually caused by impact ionisation in regions with high electric fields close to the junction, where highly energetic carriers can ionise new carriers in collisions with the lattice and cause carrier multiplication [27]. This process is called avalanche breakdown, and it is the voltage at which this breakdown occurs that usually limits the maximum operating voltage of a sensor.

One polarity of the signal charge generated by a traversing particle is collected by one electrode of the p-n junction. Charge generated inside the depletion region will quickly drift towards the collection electrode. If the sensor is not fully depleted, diffusion in the non-depleted areas also plays an important role in the charge collection process. According to the Ramo theorem [28], a signal is already detectable when the charge carriers of both polarities start moving, and not only when charge arrives to the collection electrode. The instantaneous current induced on an electrode by the movement of a charge  $e$  with a drift velocity  $v$  (which is often proportional to the electric field) is given by:

$$i = eE_w v, \quad (2.15)$$

where  $E_w$  is the so-called weighting field, which is different from the actual electric field in the sensor and is obtained by applying a unit potential to the electrode under consideration and zero potential to all other electrodes. To calculate the charge  $Q$  induced on an electrode by a charge  $e$  drifting in the time interval  $[t_1, t_2]$  from position  $x_1$  to  $x_2$ , one has to integrate 2.15 over the

time of charge collection:

$$Q = \int_{t_1}^{t_2} i(t) dt = e [\phi_w(x_1) - \phi_w(x_2)], \quad (2.16)$$

where  $\phi_w$  is the weighting potential, also obtained by raising the electrode under consideration to unit potential, setting all others to zero, and solving the Poisson equation [29].

This weighting potential is plotted in fig. 2.4 assuming an arbitrary sensor thickness of 1 in the y-direction, an infinitely wide electrode at  $y = 1$  and a collection electrode of different widths at  $y = 0$  on which the unit potential is applied. Fig. 2.4a shows the weighting potential for two infinite parallel plates, while fig. 2.4b and c show this potential for a collection electrode width of 1/3 and 1/10, respectively. The smaller the electrode, the larger the area where the weighting potential approaches zero, meaning that drift of carriers in this area will induce very little signal on the collection electrode. The closer the charge is to the electrode, the more signal it will induce, as seen by the increasing gradient of the weighting potential, and for small electrodes, most of the signal is induced in this last part of the drift path. Once all the charge has arrived to the collection electrode, the integral of the induced current is the total collected charge. The time it takes to collect the charge by drift in silicon sensors is typically in the order of a few nanoseconds.

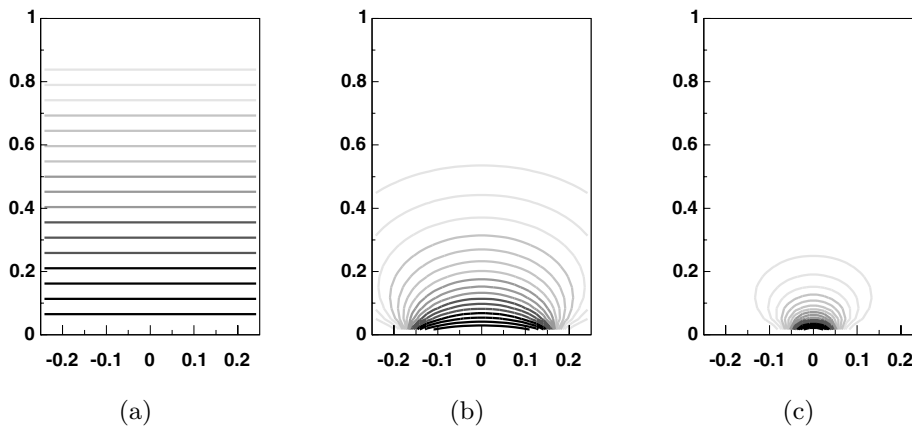


**Figure 2.4:** Weighting potential for (a) two infinite parallel plates and a collection electrode width of (b) 1/3 and (c) 1/10 times the sensor thickness (reproduced from [29]).

## 2.2 Radiation effects in the sensor – Non-ionising energy loss

When interacting with the silicon sensor material, the energy loss of highly energetic particles does not result exclusively in the generation of electron-hole pairs producing the electrical signal, but also with the displacement of nuclei out of their lattice position. This non-ionising energy loss component leads to the creation of defects in the crystal, which may be electrically active and change the electrical properties of the material. The primary lattice defects

initially created are vacancies and interstitials. A vacancy is the absence of an atom from its normal lattice position. If that displaced atom moves into a non-lattice position, the resulting defect is called an interstitial. A stable configuration of a vacancy and an adjacent interstitial is a secondary point defect known as a Frenkel pair [30]. Apart from point defects, the primary knock-on atom dislodged by the incident particle can displace many other atoms locally, thereby creating a disordered region with a high defect density, a so-called cluster defect. A depiction of the different types of lattice defects produced by an incident neutron with an energy in the order of 1 MeV is given in fig. 2.5 (reproduced from [31]).

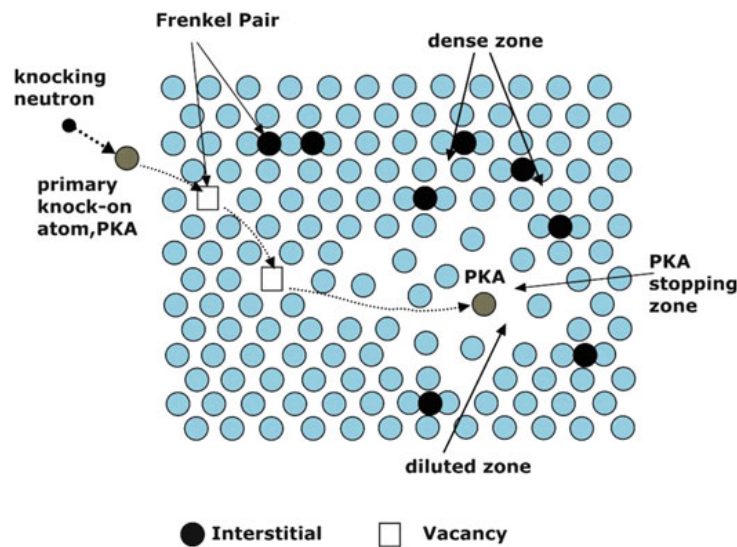


**Figure 2.5:** An example of defect generation in silicon by an impinging high-energy neutron [31].

Different types of particles interact differently with the silicon lattice. For example, charged particles will produce more point defects and less clusters than neutrons due to their electromagnetic interaction with the atom nuclei. To be able to compare the damage caused by different types of particles with different energies, the displacement damage is described through a quantity called non-ionising energy loss (NIEL), which relates the damage caused by a certain fluence of particles to the damage caused by a fluence of 1 MeV neutrons. The displacement damage is hence often described in terms of neutron equivalent fluence,  $n_{eq}/\text{cm}^2$ . The hardness factor  $\kappa$  is used to convert the damage caused by a certain type of particle with a certain energy to the damage caused by 1 MeV neutrons, and is e.g. equal to 0.62 for 24 GeV protons provided by the CERN-PS.

The net result of all the defects created in the material is the introduction of energy levels in the bandgap, which can give rise to a number of adverse effects. One of them is the increase in leakage current, since the energy levels in the bandgap act as generation-recombination centres. The radiation-induced energy levels near the middle of the bandgap can cause a significant increase in thermal generation rates, which is the main mechanism for leakage current increases

in silicon devices. This increase in volume generation current is proportional to the fluence.

Another effect is the trapping of carriers at a deep level, where a carrier can recombine and be lost for detection, or at a shallow level, where a carrier is temporarily captured at a defect centre and is later emitted to its band. This leads to a reduction in carrier lifetimes and consequently the diffusion length. Given a carrier lifetime  $\tau$ , an initial amount of generated charge  $Q_0$  will decay exponentially with time:

$$Q(t) = Q_0 e^{-t/\tau}. \quad (2.17)$$

Therefore, charge trapping in the sensor material can cause a reduction in sensor signal. Because of that, one of the main approaches to improve the radiation hardness of silicon sensors is to collect the charge by drift rather than diffusion, which strongly reduces the charge collection time and the probability for signal charge to be captured by radiation-induced traps.

A third important effect is the change in the effective doping concentration caused by charged defects. An example of this is shown in fig. 2.6. The acceptor-like traps in the n-type starting material alter the effective doping concentration (as well as the full depletion voltage) to the point where, after a fluence of around  $10^{12} \text{ n}_{\text{eq}}/\text{cm}^2$ , the material starts behaving like p-type. As a consequence of this type inversion (or space charge sign inversion), the pn-junction moves from the p+ side of the sensor to the n+ side and the space charge region grows from there [29].

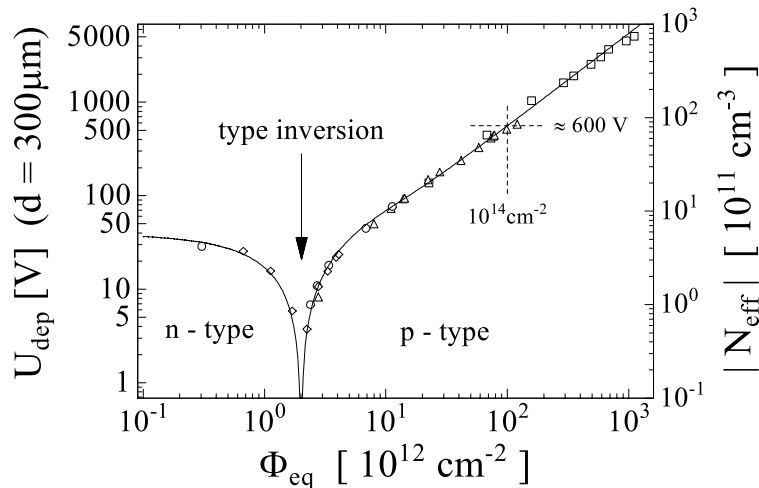


**Figure 2.6:** Full depletion voltage of a 300- $\mu\text{m}$ -thick silicon sensor and its absolute effective doping versus the normalised fluence (reproduced from [29]).

Note that all these effects can be counteracted to a certain extent by the recombination and rearrangement of defects over time, referred to as annealing. Several material properties, such as minority-carrier lifetime, diffusion length or leakage current show a recovery after either short-term or long-term annealing. These processes depend strongly on the temperature as well as the free carrier concentration within the device [32].



## 2.3 Monolithic sensor concepts

Monolithic active pixel sensors (MAPS) integrate the sensor and the readout electronics on the same chip. Fig. 2.7 shows a cross-section of a typical MAPS detector [33]. The n-well collection electrode on a p-type epitaxial layer collects the charge generated by the traversal of an ionising particle. The p-wells around the collection electrode host the in-pixel electronics consisting of NMOS transistors. In the small depletion region around the collection electrode, the generated charge is collected by drift, but the vast majority of the epitaxial layer remains undepleted and the signal charge is primarily collected by diffusion. In this case, the collection electrode occupies only a small fraction of the total pixel area, so this is referred to as a small collection electrode design. To enhance the depletion and achieve faster charge collection by drift, leading to better radiation tolerance, one can also place the front-end and readout electronics inside the collection electrode. In this case, the electrode containing the electronics will occupy most of the pixel area and this is called a large collection electrode design.

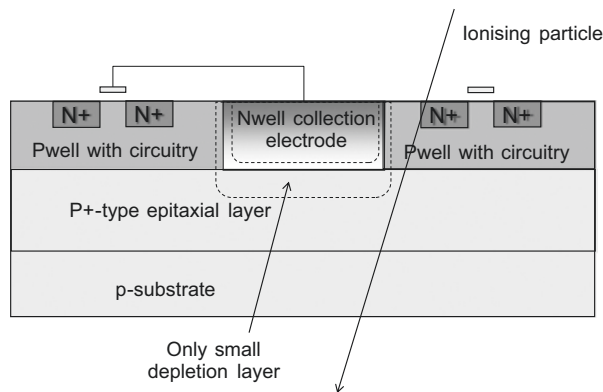


**Figure 2.7:** Cross-section of a typical MAPS detector (reproduced from [33]).

### 2.3.1 Small collection electrode designs

The main advantage of the small collection electrode approach is a low sensor capacitance, which can be in the order of a few femtofarads. This capacitance has far-reaching consequences for many design aspects, in particular the noise and power consumption of MAPS. The collection electrode is typically followed by an amplification stage, where the thermal noise in the channel of the input transistor is usually the dominant noise source [34]. Regardless of the operating region of this transistor, its thermal noise expressed as an equivalent series voltage is inversely proportional to the square root of its transconductance  $g_m$ . Since the voltage signal on the collection electrode with a capacitance  $C$  obtained by collecting a charge  $Q$  is given by

$$V = \frac{Q}{C}, \quad (2.18)$$

for the signal-to-noise ratio one can write:

$$\frac{S}{N} \sim \frac{Q}{C} \sqrt{g_m}. \quad (2.19)$$

In general,  $g_m$  is either proportional to the transistor bias current (in weak inversion) or to the square root of the bias current (in strong inversion). Assuming that this bias current dominates the overall power consumption  $P$ , eq. 2.19 can be rearranged to yield:

$$P \sim \left( \frac{S/N}{Q/C} \right)^{2m}, \quad (2.20)$$

where  $1 \leq m \leq 2$  depending on the operation region of the input transistor. Conversely, the thermal noise of the input device in strong inversion in an open-loop circuit with a flat frequency response over a certain bandwidth, expressed as an equivalent noise charge (i.e. the input charge fluctuation required to cause the voltage noise observed at the output), can be written as:

$$ENC_{thermal}^2 \sim \frac{4 kT C^2}{3 g_m \tau}, \quad (2.21)$$

where  $k$  is the Boltzmann constant,  $T$  the temperature and  $\tau$  the shaping time of the circuit. As the noise scales linearly with the capacitance, a low capacitance is key for achieving an optimal low-noise performance. All these equations illustrate the interdependence between the sensor capacitance, power consumption, noise and timing in MAPS. One can conclude that a small sensor capacitance and a large  $Q/C$  ratio are crucial to achieve a low power consumption for a given bandwidth and signal-to-noise ratio.

The cross-section shown in fig. 2.7 contains only NMOS transistors in the readout electronics. However, MAPS often have to contain more complex circuitry for signal processing. If PMOS transistors are used, the n-wells hosting these transistors normally compete with the collection electrode in the charge collection process, thereby causing the loss of signal charge. To avoid this, a deep p-well can be used to shield the n-wells of the transistors from the substrate, thus allowing the use of full complementary CMOS logic in the pixel (see fig. 2.8).

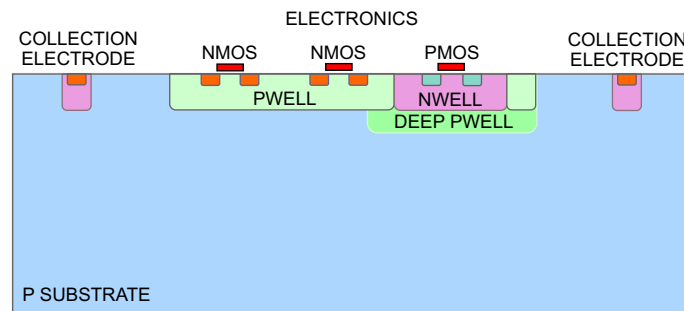


**Figure 2.8:** Cross-section of a small collection electrode design. A deep p-well is used to shield the n-wells of PMOS transistors, allowing full CMOS in the pixel.

However, with a small collection electrode, reaching full depletion under the deep p-well is still difficult, unless the area of the deep p-well and the circuitry inside it is very small. To increase the depletion region and the drift component in the charge collection, thereby increasing the radiation tolerance, more recent devices use a high-resistivity substrate or epitaxial layer [35]. This can increase the amount of collected charge while maintaining a low capacitance, leading to a higher  $Q/C$  and better  $S/N$ . Another way to enhance the charge collection is by applying a high negative voltage to the p-type substrate with respect to the collection electrode. However, this voltage is limited by the breakdown voltage of transistor junctions in standard CMOS processes, and is typically in the range of only several volts. An option is to AC-couple the collection electrode to the following amplifying stage and apply a high positive voltage to the electrode itself, but this has some penalty in sensor capacitance. Changes in the standard fabrication process can also be employed to optimise the sensor for particle detection in high-radiation environments, which will be discussed more in detail in the following chapters.

### 2.3.2 Large collection electrode designs

The large collection electrode approach places the front-end and readout circuitry inside a deep n-well collection electrode, as depicted in fig. 2.9. Since the transistor junctions are now isolated from the p-type substrate, a high reverse bias voltage in the order of 50-100 V can be applied to the collection diode [36]. The lowly doped junction combined with the high reverse voltage induces a large depleted area where charge is collected by drift, resulting in a fast charge collection and high radiation tolerance.

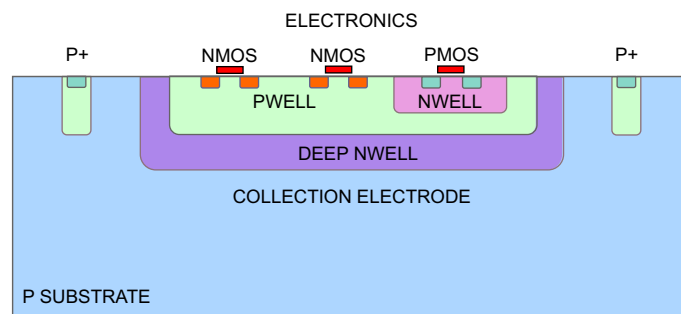


**Figure 2.9:** Cross-section of a large collection electrode high voltage design.

The drawback of a large collection electrode is a large input capacitance in the order of hundreds of femtofarads, mainly because of the junction capacitance between the deep n-well and the p-well housing the electronics. For this reason, to achieve a high  $Q/C$  one has to either limit the area and complexity of the readout circuit to achieve a smaller capacitance, or increase the collected charge e.g. by using thick high-resistivity substrates for the sensitive layer. A high

signal is needed to overcome the higher noise levels due to the large input capacitance, thereby achieving a high  $S/N$ .

Another potential problem in this approach is the risk of coupling circuit signals into the collection electrode. The bulk of all NMOS transistors is capacitively coupled to the deep n-well and therefore to the sensor cathode, so any disturbance in the p-well caused by the in-pixel digital logic can cause an unwanted signal at the collection node. Therefore, special care needs to be taken in the design of the electronics to reduce this crosstalk to acceptable levels.

### **2.3.3 Other approaches - DEPFET and SOI**

Another structure used in monolithic pixel sensors is the so-called depleted field-effect transistor (DEPFET) [37]. The DEPFET is essentially a PMOS transistor on top of an n-type depleted substrate with a backside junction. Charge generated in the sensor is collected in a potential well under the PMOS channel, and can modulate the source-drain current of the PMOS transistor just as much as a change in the gate voltage. This provides an internal amplification of the signal charge. The small collection electrode capacitance allows low-noise operation. The sensor can be read out by sampling the voltage on the PMOS source or by integrating the drain current. DEPFETs are already used in high-energy physics experiments, but limited radiation hardness due to damage in the MOS structure oxide and a complex development and fabrication of these devices make them less attractive for high-radiation environments.

MAPS have also been fabricated in SOI technology [38]. These devices are composed of a thick, high-resistivity substrate for the sensing part (under the buried oxide) and a thin silicon layer for CMOS circuits. Due to the high bias voltages applied to deplete the sensor, the so-called back-gate effect has traditionally caused problems by affecting the operation of transistors in the front-end and readout electronics. However, this can be mitigated using additional process steps such as implanting a buried p-well under the buried oxide. Good performance of SOI pixels in a particle beam has been demonstrated, and further improvements are being developed for radiation hardness, which has been limited due to the accumulation of radiation-induced charge in the buried oxide affecting the sensor and electronics.

## **2.4 Radiation effects in the electronics – Total ionising dose and single event effects**

The front-end and readout electronics are mainly affected by ionising radiation because of the damage in the surface oxide layers and at the Si-SiO<sub>2</sub> interface. The damage is described through a quantity called total ionising dose (TID) and is measured in units of rad. TID is known to lead to two types of defects in dielectrics: trapped charges and interface states. The trapped

charges are mainly holes, which can get trapped permanently near the Si-SiO<sub>2</sub> interface due to their very low mobility in the oxide. Interface states are dangling Si bonds which introduce energy states in the silicon band gap, at the interface [39].

The radiation-induced positive trapped charge built up in the gate oxide causes a shift in the threshold voltage of transistors in the front-end and readout circuitry [40]. In the case of NMOS transistors, the threshold voltage is decreased, which consequently leads to an increase in the leakage current of the device. A similar effect can be observed in the shallow trench isolation oxide of MOS devices, where the radiation-induced positive charge can open a conductive channel even when the main transistor is turned off, again leading to a leakage current flow between source and drain. This is particularly noticeable when the width of the transistor is very small, and is known as the radiation-induced narrow channel effect (RINCE) [41].

An example of threshold voltage decrease in NMOS transistors in the TowerJazz 180 nm CMOS technology is shown in fig. 2.10. All the measured transistors have a minimal gate length of 0.18  $\mu\text{m}$ . The most affected structure is the minimum width NMOS transistor with a threshold shift of about 40 mV after 10 Mrad of TID, while the structures wider than 1  $\mu\text{m}$  show only a marginal threshold shift [42]. Even in the narrow devices, the threshold shift starts to saturate after a few megarads, which can be explained by interface states starting to contribute significantly to the charge balance at the transistor edge and compensating the effect of positive trapped charge.

Note that, like with displacement damage, short-term annealing can be helpful to reverse the effects of TID, as evidenced by the last point in the plot taken after 24 hours of annealing.

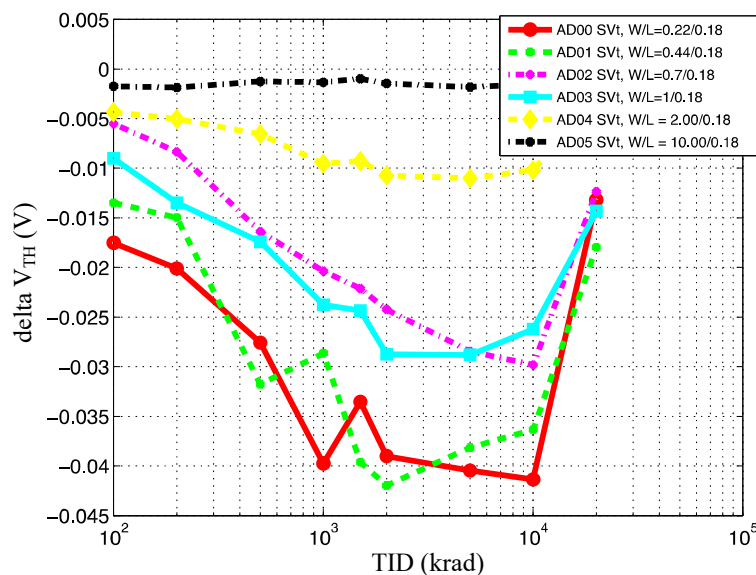


**Figure 2.10:** Threshold voltage shift as a function of TID for NMOS transistors with different gate width for a minimal gate length of 0.18  $\mu\text{m}$ . The points taken at  $2 \times 10^4$  krad correspond to 24 h of annealing (reproduced from [42]).

The ultra-thin gate oxide of deep submicron technologies is inherently more tolerant to total ionising dose effects, since for an oxide thickness below  $\sim 5$  nm tunnelling becomes more and more effective to neutralise the radiation-induced positive charge [43]. Therefore, it is the radiation-induced charge trapping in the field oxide that ultimately limits the radiation tolerance of conventional CMOS circuits. Nevertheless, this issue can be mitigated by employing hardness-by-design layout techniques.

One such technique is replacing standard, open-layout NMOS transistors with more advanced layout structures, most commonly enclosed layout transistors (ELT) [44, 45]. The layout of such transistors is shown in fig. 2.11 [46]. The closed gate ensures that all source-to-drain current flows underneath the gate, thus eliminating any leakage path underneath the field oxide or along the active area edge. On the other hand, the p+ guard ring implemented around the bottom transistor prevents inter-transistor leakage between the two.

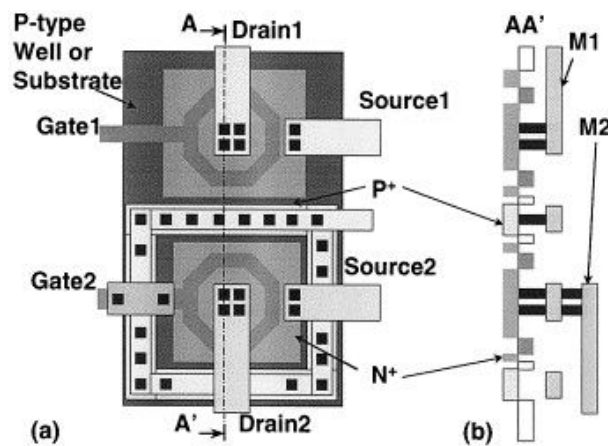


**Figure 2.11:** (a) Layout and (b) cross-section of two enclosed layout NMOS transistors with a p+ guard ring (reproduced from [46]).

Apart from the cumulative radiation effects described thus far, the passing of a single particle can also induce transient phenomena known as single-event effects. A single-event upset (SEU) occurs when a digital circuit, usually a memory cell, is disturbed by the charge generation from a passing ion to the point of changing logic state [47]. This can cause a corruption in the configuration or data bits of a detector, and is usually mitigated by triplicating the critical memory cells and requiring at least two of them to change state.

Charge deposition by a particle near a transistor source or drain can also cause single-event latchup. This is a process where the charge triggers the intrinsic bipolar junction transistors present in CMOS well structures to conduct a large current, which can cause damage or even destruction to the circuitry. This can be prevented by reducing the resistance between the transistor source/drain and the bulk contact, which means placing well taps in close proximity to the transistors.

## 2.5 Front-end and readout concepts

The signal charge collected by the sensor can be quite small, about a few femtocoulombs in a typical high-energy tracking detector, so the sensor signal must be amplified [48]. This is typically done using an in-pixel charge-sensitive preamplifier. In early active pixel sensor readout architectures, this amplifier was often as simple as a source follower buffer, such as the one used in the standard 3-transistor structure for a rolling shutter readout [49]. The principle of this simple readout architecture is illustrated in fig. 2.12. Transistor M1 resets the sensor diode to a reverse bias and is switched off to integrate the sensor charge on the gate of transistor M2, which is the input of a source follower. M3 acts as a row selection switch, while the column selection switch and the source follower current source are located outside the pixel [50]. This way, the matrix of pixels is read out one pixel at a time, and further amplification and hit discrimination is performed at the chip periphery.

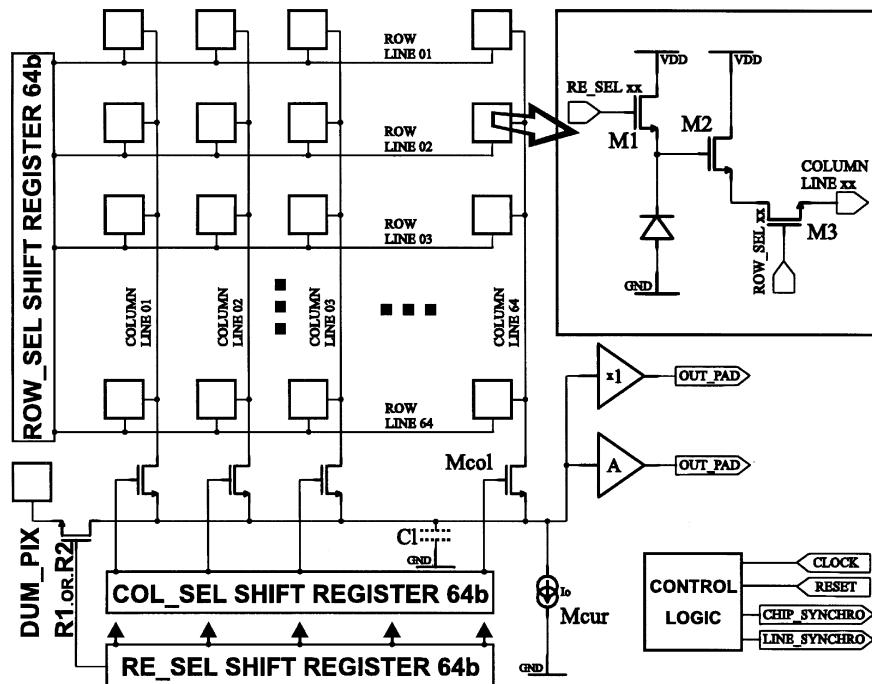


**Figure 2.12:** Simplified diagram of the rolling shutter readout of a pixel matrix and the 3-transistor structure inside the pixel (reproduced from [50]).

More advanced readout architectures integrate more features inside the pixel, including amplification, shaping and discrimination. A block diagram of the in-pixel front-end electronics typically implemented in active pixel sensors today is shown in fig. 2.13. As mentioned, the amplification stage is usually implemented as a charge-sensitive preamplifier with a feedback capacitor and an additional feedback path to define the DC point of the input, which can be a resistor or a MOSFET operated in the linear region. The charge-to-voltage conversion gain of

such a circuit can be obtained as follows:

$$\frac{V_{OUT}}{Q_{IN}} = -\frac{1}{C_f} \frac{1}{1 + \frac{1}{A} + \frac{C_{in}}{AC_f}}, \quad (2.22)$$

where  $C_{in}$  is the total input capacitance given by the detector capacitance plus the transistor and stray capacitances of the preamplifier, while  $A$  is the finite open-loop voltage gain of the amplifier.

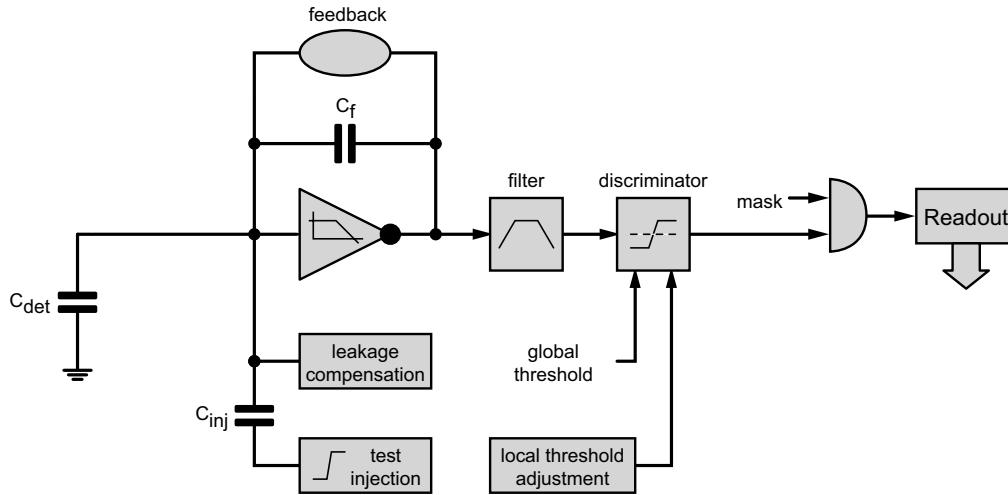


**Figure 2.13:** Block diagram of a generic in-pixel front-end circuit.

Therefore, apart from a careful choice of the feedback capacitor value, the design of the preamplifier is crucial to achieve a high gain and high bandwidth while maintaining a low power consumption. Single-ended cascoded amplifiers such as the direct cascode or folded cascode topology [51] are popular choices for the implementation of this preamplifier. As already mentioned in sect. 2.3.1, a high transconductance  $g_m$  of the input device is desirable in both cases, as this helps to achieve a high gain-bandwidth product and low noise. Even so, for radiation-hard applications a PMOS input transistor is usually a better choice, regardless of the penalty on  $g_m$ , because it avoids problems with leakage currents after irradiation which are present in NMOS devices.

The increase in sensor leakage current after irradiation also needs to be taken into account, since it can affect the DC operating point if the preamplifier is DC-coupled to the sensor. Several leakage compensation schemes have been used, the most popular being the Krummenacher feedback scheme [52] shown in fig. 2.14. The circuit compares the DC-value of the preamplifier output to a reference voltage  $V_{REF}$ . When a positive charge is deposited at the input node, the output goes negative and the complete bias current  $2I_B$  is steered through M1b while M1a is turned off. The input node is therefore discharged with a net current of  $I_B$ , independent of  $I_{LEAK}$ .



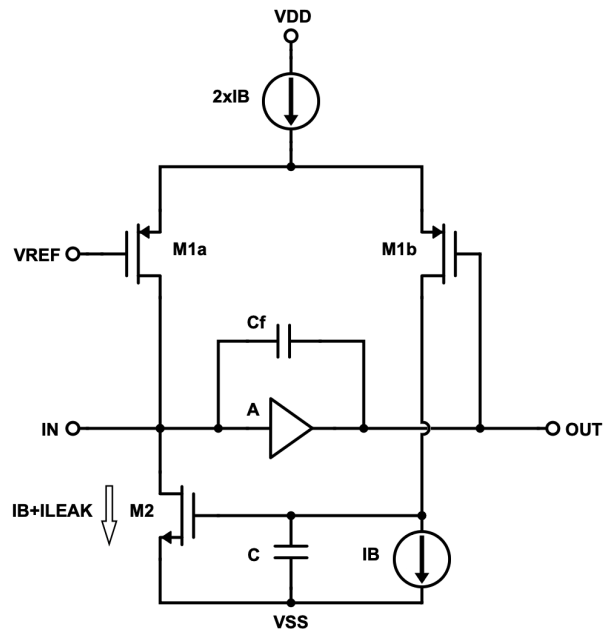


**Figure 2.14:** Krummenacher feedback circuit used for leakage current compensation.

A band-pass filter (or shaper) is often included as part of the front-end circuit to limit the bandwidth of the preamplifier output signal, reducing the low- and high-frequency noise contributions. This shaper can be a cascade of several low-pass and high-pass stages. Higher order filters lead to shorter pulses for a given peaking time, which can be useful in high-rate applications, where the baseline must be restored quickly to avoid pile-up and limit the so-called dead time of the circuit.

The shaper is usually followed by a discriminator with an adjustable threshold, which can be implemented for instance as a differential pair with a voltage offset between the two inputs [51]. When the analogue signal exceeds this threshold, the discriminator produces a digital pulse at its output and the pixel is deemed to have "fired". The threshold can be controlled globally or, if need be, locally with a per-pixel threshold adjustment. The latter can be used to improve the threshold uniformity of pixels within a large matrix.

The front-end often contains additional features for testing and ease of operation. The possibility of capacitively injecting a test pulse to the input of the preamplifier is a useful feature to check the threshold and noise levels of the front-end without having to use a particle beam. Another common practice is to include the possibility of masking a pixel, i.e. disabling its output if it generates an excessive noise hit rate because of e.g. a broken front-end or a bad sensor cell.

Readout circuitry is used to further process the digital hit signals of the discriminators in the pixel and/or at the chip periphery. The discriminators immediately perform a zero-suppression, meaning that only the pixels with hits above a certain charge are read out. This is the basis for all event-driven readout architectures most commonly used for particle detection. The main

objective of the readout circuit is to provide the correct addresses of fired pixels within the pixel matrix. The easiest way to achieve this is to connect the discriminator outputs directly to the chip periphery and assign the pixel address there before sending it off-chip. However, the number of routing lines required to connect each pixel to the periphery becomes too large for large matrices. To reduce the number of required connections, pixels can be grouped together to employ a parallel hit transfer mechanism from the pixels to hit buffers at the periphery, which is called a parallel-pixel-to-buffer architecture [53].

Another approach is to assign the address inside the pixel and transmit the address information as quickly as possible to the periphery according to some priority scheme. This scheme can be implemented e.g. by using a column-based priority encoder [54] or a token logic, where a token signal passes from pixel to pixel, and the first pixel to receive the token is the first one to be read out. In high-energy physics applications, it is often not enough to obtain the address of hit pixels using a binary readout, but it is also necessary to have analogue information about the pulse amplitude. This is commonly done by measuring the time-over-threshold (ToT), i.e. the pulse width at the output of the discriminator. This pulse width corresponds to the amplitude of the analogue pulse at the output of the preamplifier/shaper, which in turn corresponds to the amount of charge deposited by a particle in the sensor. The time-over-threshold is typically encoded by storing the value of a counter at the rising and the falling edge of the discriminator pulse. At the LHC, the clock frequency of the counters is synchronised with the frequency of the particle bunch crossings and is equal to 40 MHz. This approach is used for example in the well-known column drain architecture [55, 56] developed for the CMS experiment. A schematic of the in-pixel logic used in this type of architecture is sketched in fig. 2.15.

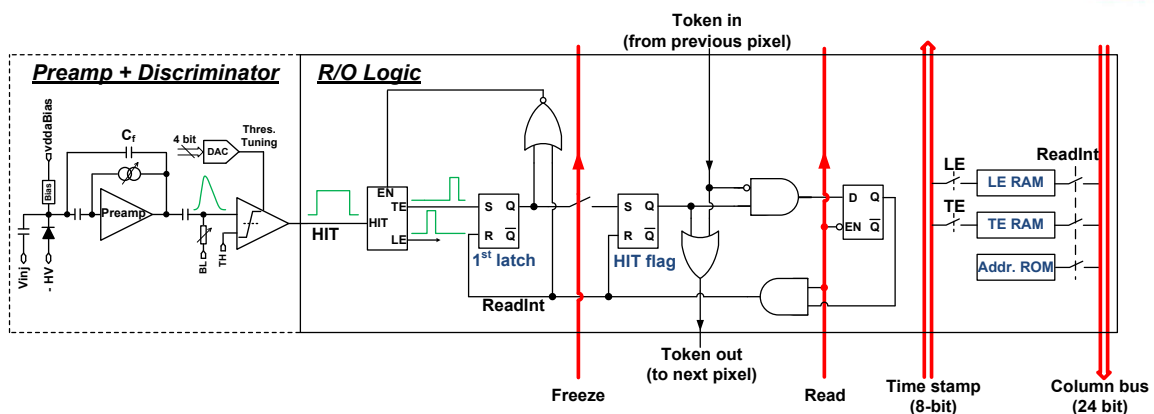


**Figure 2.15:** Front-end and in-pixel logic used in the column-drain readout architecture. An 8-bit time-stamp is stored for the leading and trailing edge of the discriminator.

The discriminator output is sampled by an edge-detector and the hit information is latched on the trailing edge. This disables the detection of new hits and asserts a hit flag, which in turn quickly sends a token signal down the column. In the next clock cycle, the peripheral readout

logic freezes the assertion of new hit flags within the column and sends a read signal to the pixel which sent the token. This read signal is used to send the contents of the in-pixel RAM/ROM memories down the column. These memories contain the 8-bit timestamps for the leading and trailing edge as well as the 8-bit address of the pixel within the column. Once the data has been read, the in-pixel latches are reset and the logic is ready to detect a new hit.

A different approach is to transmit the pixel address bits asynchronously down the column [57]. This avoids the clock propagation over the pixel matrix and reduces the digital power consumption. Since the delay of the leading edge of the discriminator pulse also depends on the deposited charge (the preamplifier reacts faster in case of a large sensor signal), this timing difference (called time walk) can also be used to obtain analogue information, e.g. by adding a time-stamp at the chip periphery. This approach will be discussed in much more detail in the following chapters.

In the experiments at the LHC, most of the data from pixel detectors does not contain relevant information, since interesting physics processes are very rare. A selection of potentially interesting events is made by other detectors of the experiment in a process which can take several microseconds. After that, a trigger signal is sent to the pixel chips and only the triggered data is sent off-chip [58]. Therefore, the pixel chips need to be able to store the hit data during this trigger latency and be capable of performing a triggered readout once this trigger signal arrives.

# Chapter 3

## Design and characterisation of radiation-hard CMOS sensors

### 3.1 Sensor technology

#### 3.1.1 The standard TowerJazz 180 nm process

The monolithic CMOS sensors described in this work were fabricated in the TowerJazz 180 nm CMOS process which was also used for the upgrade of the Inner Tracking System of the ALICE experiment [59]. The sensors in this technology implement a small collection electrode to achieve a small sensor capacitance, as described in sect. 2.3.1. A cross-section of a pixel in the standard TowerJazz 180 nm process is shown in fig. 3.1 [60]. The charge generated in the sensor is collected by the small n-well collection electrode. The electrode is separated from the in-pixel electronics by several microns to reduce the lateral capacitance to the wells. The n-wells of PMOS transistors are shielded by a deep p-well so that they do not compete with the collection electrode in the charge collection. This allows the use of full CMOS and therefore more complex readout circuitry in the pixel. The technology uses a 3 nm gate oxide thickness and follows the general trend observed in many deep submicron CMOS technologies for increased total ionising dose tolerance with decreasing gate oxide thicknesses [61].

The foundry also allows the use of different starting materials for the sensor, which means that, for applications in a high-radiation environment, a high-resistivity p-type epitaxial layer can be used to enhance the depletion around the collection electrode [62]. The designs discussed in the following sections use a 25-30  $\mu\text{m}$  thick epitaxial layer with a resistivity of over 1  $\text{k}\Omega\text{cm}$ . To further increase the depletion zone and further reduce the sensor capacitance, a reverse bias of up to 6 V is applied to the p-type substrate of the sensor. Since the bulks of NMOS transistors see the same reverse voltage applied to the substrate, this bias is limited by the breakdown of the source/drain junctions of NMOS transistors, which occurs at around 8 V.

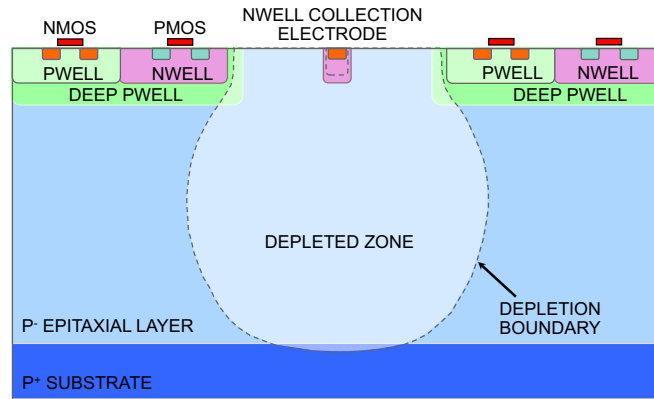


**Figure 3.1:** Cross-section of a pixel in the standard TowerJazz 180 nm process (reproduced from [60]).

However, even with reverse bias, it is difficult to deplete the areas under the deep p-well, near the pixel edges, and achieve full depletion of the sensitive layer. The signal charge generated outside the depleted area is still collected primarily by diffusion, which results in a moderate tolerance to non-ionising radiation of up to  $10^{13}$   $n_{eq}/cm^2$ . This is sufficient for the modest ALICE requirements, but for a radiation tolerance up to  $10^{15}$   $n_{eq}/cm^2$  and beyond, for more demanding applications, a drift field and depletion is required over the full sensitive layer. Increasing the collection electrode helps to laterally extend the depletion region, but brings a significant capacitance penalty. Reducing the area of the in-pixel electronics also helps to create a potential gradient, but this limits the amount of circuitry one can implement inside the pixel. Therefore, a process modification has been introduced to achieve full depletion of the epitaxial layer.

### 3.1.2 Designs in the modified TowerJazz process

The idea behind achieving full depletion of the sensitive layer combined with a low capacitance collection electrode is to implement a large or even planar junction separate from the collection electrode. In this case, a low-dose deep n-type implant is used over the full pixel to create a planar junction in the epitaxial layer, below the wells containing circuitry. This is depicted in fig. 3.2. The depletion starts from the junction and immediately extends over the full pixel area. The epitaxial layer is fully depleted even without reverse sensor bias. The n-type implant is sufficiently low-dose to be fully depleted up to the n-well collection electrode for reverse bias voltages of a few volts, and maintain a sensor capacitance of only a few femtofarads. This also means that the collection electrodes in a pixel matrix are mutually isolated. The depletion layer now also separates and isolates the p-wells containing the electronics from the substrate, which means that they can be biased independently. The potential barrier created by the n- implant is sufficient to apply a reverse substrate voltage of above 20 V for a 25  $\mu m$  thick epitaxial layer, while still avoiding punchthrough between the p-wells and the substrate. This further increases the electric fields in the sensitive region and potentially leads to a faster charge collection.

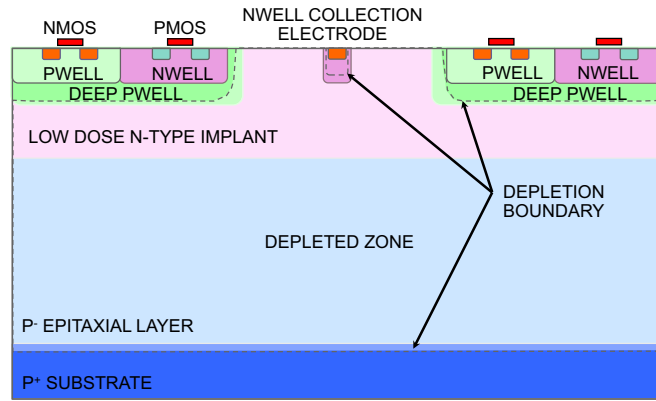


**Figure 3.2:** Cross-section of a pixel in the modified process [60]. The additional n-type implant allows full depletion of the sensitive layer.

Another advantage of this approach is that, apart from defining the region of the n-implant over the pixel matrix, the process modification does not require any layout changes in the design of the sensor or the circuitry. Therefore, the same design can be produced in both the standard and the modified process, allowing a direct comparison between the two.

The Investigator chip [63] was produced to characterise the performance of monolithic CMOS sensors implemented in the TowerJazz technology. The chip consists of a collection of pixel sub-matrices which differ among each other in terms of a few parameters, some of which affect the shape and extension of the depleted region: pixel size, electrode size, electrode-to-deep-p-well distance. The analogue voltage signals from the collection electrodes are read out using source follower buffers. A number of these chips have been characterised with a  $^{90}\text{Sr}$  radioactive source, which emits electrons that traverse the sensor and generate a signal similar to the response to minimum ionising particles [64]. Fig. 3.3 compares the signal amplitudes and rise times of signals at the collection electrode for a  $50 \times 50 \mu\text{m}^2$  pixel size on an unirradiated sample, a sample irradiated to a fluence of  $10^{14} \text{ n}_{\text{eq}}/\text{cm}^2$  and a sample irradiated to a fluence of  $10^{15} \text{ n}_{\text{eq}}/\text{cm}^2$ . All samples shown were produced using the modified process and were tested at a substrate bias of  $-6 \text{ V}$ .

The curves in fig. 3.3a show the Landau spectra of the  $^{90}\text{Sr}$  source. In all cases, the peak of Landau distribution is clearly separated from the noise peak located close to  $0 \text{ mV}$  of amplitude. The red curve shows very good signal response and a signal loss of less than 20% after a fluence of  $10^{15} \text{ n}_{\text{eq}}/\text{cm}^2$ , much in contrast to a sensor in the standard process after this irradiation fluence, from which no useful signal could be extracted anymore. The sensor maintains a fast signal response even after a fluence of  $10^{15} \text{ n}_{\text{eq}}/\text{cm}^2$ , as seen in fig. 3.3b. The time spread of only  $\sigma = 2.78 \text{ ns}$  is less than even the unirradiated sensor of the standard process, which gave  $\sigma = 4.6 \text{ ns}$ . Note that the rise time includes the charge collection time, but is also limited by the speed of the source followers used to read out the signals.

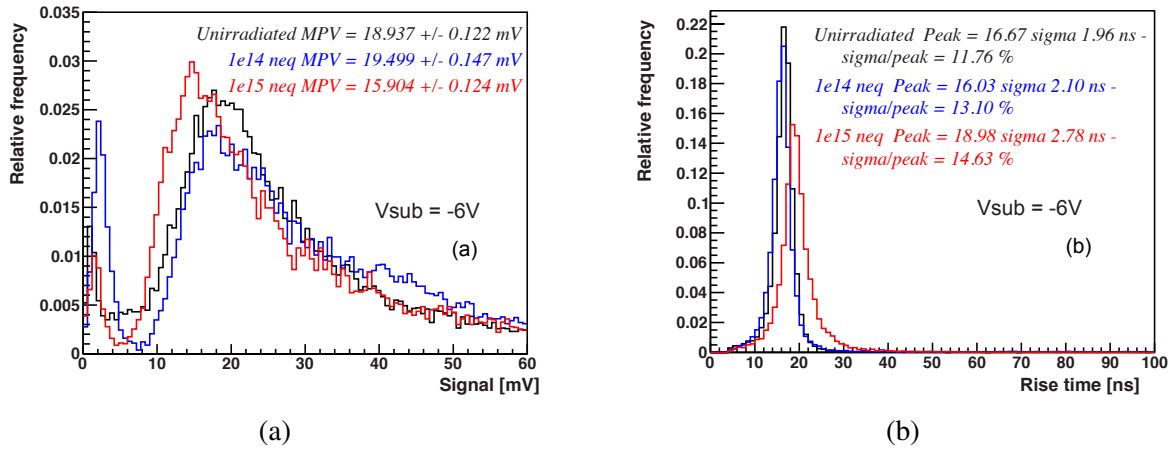


**Figure 3.3:** Signal response of a sensor produced in the modified process before irradiation (black curve), after  $10^{14} n_{eq}/cm^2$  (blue curve) and after  $10^{15} n_{eq}/cm^2$  (red curve). Fig. (a) shows the amplitude distribution for  $^{90}Sr$  source tests and fig. (b) shows the signal rise time [65].

The detection efficiency of the sensor is measured in a particle beam [65]. The chip is placed between several reference detectors (a so-called beam telescope) which provide a  $9 \mu m$  position resolution for hits on the sensor surface. The efficiency is calculated as the ratio of the number of events with telescope tracks and a corresponding sensor hit to the number of all events with a telescope track. The detection threshold is set as low as possible while remaining above the noise levels. For each of the measured Investigator sub-matrices, a  $2 \times 2$  pixel group is read out and the efficiency is plotted as a function of the hit position. The main results for samples produced in the modified process are shown in figure 3.4. After correcting for edge effects due to the telescope resolution, for unirradiated  $50 \times 50 \mu m^2$  pixels with a  $3 \mu m$  electrode diameter and  $18.5 \mu m$  electrode-to-deep-p-well spacing, the efficiency is found to be  $98.5\% \pm 0.5\%$  (stat.)  $\pm 0.5\%$  (syst.). For  $10^{15} n_{eq}/cm^2$  irradiated sensors with a  $3 \mu m$  electrode and  $3 \mu m$  spacing, the measured efficiency is  $98.5\% \pm 1.5\%$  (stat.)  $\pm 1.2\%$  (syst.) for a pixel size of  $25 \times 25 \mu m^2$ . In both cases, the efficiency is uniform across the pixel surface. This suggests a negligible loss in detection efficiency of sensors in the modified process even after irradiation to  $10^{15} n_{eq}/cm^2$ .

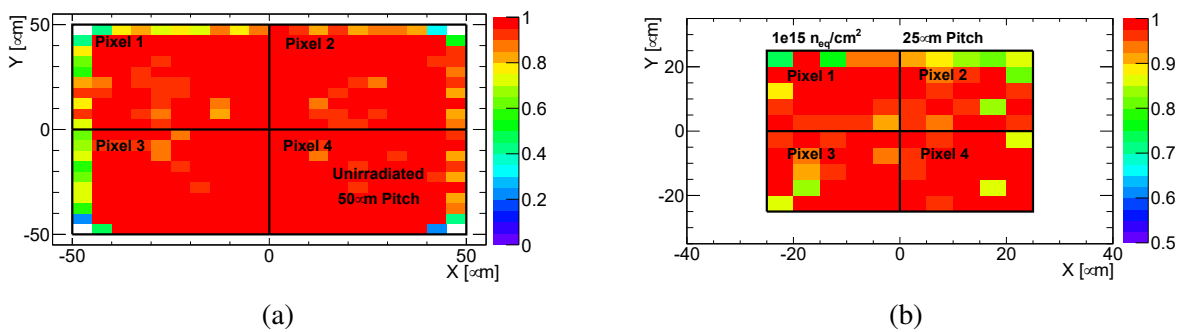


**Figure 3.4:** Detection efficiency across the  $2 \times 2$  pixel group for: (a) unirradiated  $50 \times 50 \mu m^2$  pixel with  $3 \mu m$  electrode and  $18.5 \mu m$  spacing, (b)  $10^{15} n_{eq}/cm^2$  irradiated  $25 \times 25 \mu m^2$  pixel with  $3 \mu m$  electrode and  $3 \mu m$  spacing.

These encouraging measurement results prompted the design of full-scale prototypes in the modified TowerJazz 180 nm process, which would meet the requirements of the outer pixel layers in the ATLAS experiment in terms of detection efficiency, position and time resolution, power consumption and radiation hardness. This would prove that monolithic CMOS sensors are a feasible option for particle detection even in the most demanding environments with extreme radiation levels.

The MALTA chip (short for "Monolithic from ALICE To ATLAS") is the largest monolithic CMOS sensor designed to meet the ATLAS requirements. It contains a matrix of  $512 \times 512$  pixels with a size of  $36.4 \times 36.4 \mu\text{m}^2$ . The total chip size is around  $2 \times 2 \text{ cm}^2$ . The layout of the full chip is shown in fig. 3.5. Apart from the large pixel matrix, the chip contains several blocks to ease the operation of the chip and interface it with the outside world. The digital periphery contains parts of the readout logic as well as the configuration registers used to tune the various settings available on the chip. In the case of bias currents and voltages for the front-end preamplifier, the register values are converted to the desired current or voltage values using digital-to-analogue converters (DACs). The digital address and timing information of hit pixels is transmitted off-chip through a 40-bit parallel output, which uses either a low-voltage differential signal (LVDS) standard or a full-swing 1.8 V CMOS standard. The LVDS drivers [66] designed to operate up to 5 Gb/s ensure robust data transmission to off-chip data acquisition systems, while the CMOS input/output pads offer the possibility of chaining multiple chips together and transmitting the hit data between chips.

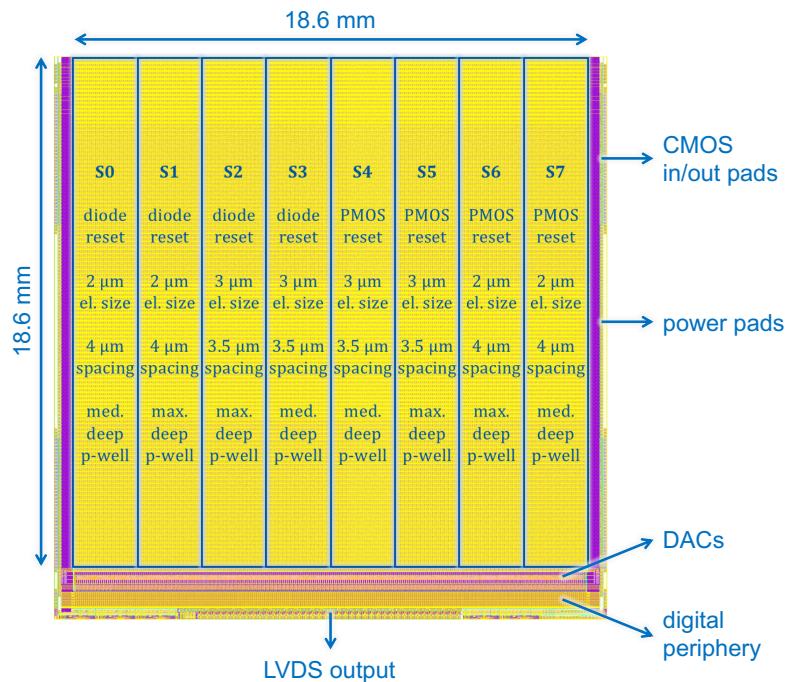


**Figure 3.5:** Layout and main building blocks of the MALTA chip. The pixel matrix is divided into 8 sectors with different sensor and front-end designs.



The pixel matrix itself is divided into 8 sectors with slightly different sensor and front-end preamplifier designs. The sectors differ in the size of the collection electrode, which varies from 2 to 3  $\mu\text{m}$  in diameter and the spacing from the electrode to the surrounding deep p-well containing the electronics, which varies between 3.5 and 4  $\mu\text{m}$ . Another important difference between the sectors is the deep p-well coverage inside the pixel. Specifically, since the deep p-well is strictly needed only under the n-wells of PMOS transistors, half of the sectors implement a "medium" deep p-well layout, where the deep p-well has been removed in areas with only NMOS transistors which are still in the vicinity of the collection electrode. The other sectors have a more conventional "maximum" deep p-well layout, where all transistors, NMOS and PMOS, have a deep p-well underneath them. In terms of front-end design, the only difference is the circuit used to reset the voltage of the collection electrode, which uses either a diode or a PMOS transistor, as further described in the next section.

The in-pixel circuitry in MALTA is divided into an analogue part, which contains the front-end preamplifier and discriminator, and a digital part, which contains the logic for reading out the pixel matrix. The layout of a pixel is seen in fig. 3.6. As mentioned, the small collection electrode in the middle is separated from the circuitry by up to 4  $\mu\text{m}$ . The analogue and digital regions are also well separated and shielded from each other with metals to avoid any crosstalk. For the same reason, different power domains are used to provide the supply voltage to the two regions. The designs implemented in both domains will be discussed in detail in the following sections.

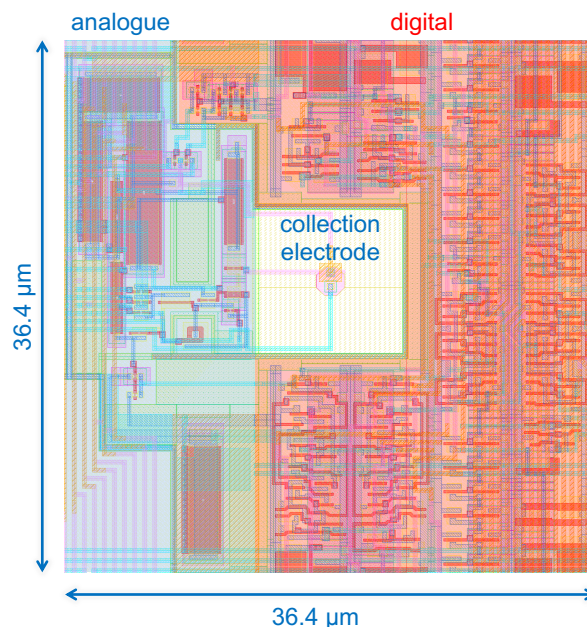


**Figure 3.6:** Layout of a pixel in the MALTA chip. The analogue and digital part are separated and shielded from each other and the collection electrode to avoid crosstalk.

## 3.2 Analogue front-end circuit

### 3.2.1 Principle of operation

The analogue part of the front-end circuitry implemented in MALTA contains the circuit to reset the voltage of the collection electrode after a particle detection, a fast, low-power shaper-amplifier and a simple discriminator. The front-end employs what is called a continuous reset of the input node, i.e. the collection electrode, which means that the reset is not applied periodically to the pixels, but that the reset circuit is continuously active. Two different implementations of this continuous reset are present in the different sectors of MALTA.

A diode reset, shown in fig. 3.7a, uses the diode D1 to reset the collection electrode voltage (node *IN*). When no charge is collected by the electrode, D1 is biased by the leakage current of the sensor diode D0, which is typically in the order of femtoamps before irradiation. The voltage of the electrode is then defined as the DAC voltage  $V_{RESET\_D}$  minus the voltage drop across the reset diode, which is typically around 500 mV. When a particle is detected, the n-well electrode collects electrons and its voltage will drop by  $\Delta V = Q/C$ . This will cause the reset diode to conduct more current and slowly charge the input node back up to its original value, which can take several hundreds of microseconds.

The PMOS reset, shown in fig. 3.7b, uses a PMOS current mirror to perform the reset of the input node. In this case, the DAC current  $I_{RESET}$  defines the current used to charge the input back up to its baseline. This current has to be larger than the leakage current of the sensor diode. In steady-state conditions, M1 is forced to conduct the leakage current of the sensor, which causes it to work in the linear region, and the voltage on the electrode is close to the DAC voltage  $V_{RESET\_P}$ . After some charge is collected and the drain-source voltage of M1 becomes large enough to push it into saturation, the input node is reset with a constant current  $I_{RESET} - I_{LEAK}$ .

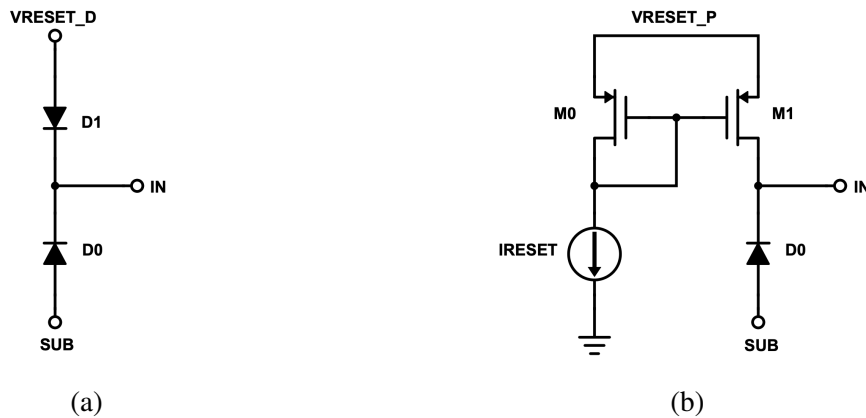


**Figure 3.7:** Two implementations of the circuit used to reset the voltage of the collection electrode (node *IN*): (a) diode reset, (b) PMOS reset.

The advantage of the diode reset is its simple implementation and low capacitance penalty, since it can be implemented as a small p+ implant inside the collection electrode. However, the conductance and hence the reset current changes significantly depending on the voltage developed by the collected charge. The PMOS reset limits this current to  $I_{RESET}$  and therefore offers more control, but at the expense of more area and a larger input capacitance due to the relatively large PMOS transistor and the metal connection to its drain.

The small electrode capacitance and high  $Q/C$  means that the voltage difference developed on the electrode by collecting the charge deposited by a particle can already be quite large. In the case of a 25  $\mu\text{m}$  thick sensitive layer, the most probable value of the Landau distribution for charge deposited by a minimum ionising particle is around 1500  $e^-$ . With a total electrode capacitance of 5 fF this means a voltage step of around 50 mV. This offers the possibility of using an open-loop voltage amplifier as the first amplification stage, instead of the conventional charge-sensitive amplifier scheme with a feedback capacitor. This can simplify the design somewhat and reduce the area required by the preamplifier/shaper circuitry.

The front-end amplifier designed for MALTA is an evolution of the front-end used in the ALPIDE chip for the ALICE upgrade [67]. The operating principle of this amplifier is illustrated in fig. 3.8. The input node (gate of transistor M1) is connected directly to the collection electrode. When the input voltage drops because of the collected charge, M1 acts as a source follower biased by the current  $I_{BIAS}$ . Therefore, a charge  $Q_S$  is transferred from a large capacitor  $C_S$  to a small capacitor  $C_{OUT\_A}$ . Ideally, for the voltage on  $OUT_A$  one can write:

$$\Delta V_{OUT\_A} = \frac{Q_S}{C_{OUT\_A}} = \frac{C_S}{C_{OUT\_A}} \Delta V_{IN} = \frac{C_S}{C_{OUT\_A}} \frac{Q_{IN}}{C_{IN}}. \quad (3.1)$$

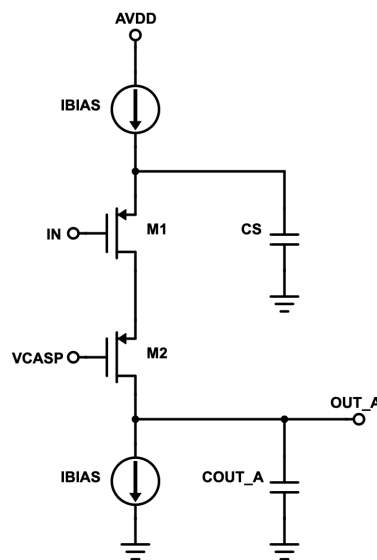


**Figure 3.8:** The operating principle of the MALTA front-end preamplifier.

This means that a high gain is obtained when  $C_S \gg C_{OUT\_A}$ . In the actual circuit,  $C_S$  is implemented as a large PMOS transistor with its source, drain and bulk connected together (using the capacitance of the MOS structure in inversion), while  $C_{OUT\_A}$  includes only the parasitic capacitances of transistors connecting to it. The full schematic of the actual front-end amplifier and discriminator is shown in fig. 3.9. M0 is the current source providing the  $I_{BIAS}$  current of the input source follower M1. M1 is placed in its own n-well together with the capacitor  $C_S$  to provide a source follower gain close to 1. Transistors M5 and M6 provide a low-frequency feedback to define the baseline voltage of  $OUT_A$  and the return to baseline after a particle hit. The bias voltage  $V_{CASN}$  and the gate-source voltage of transistor M6 conducting the current  $I_{THR}$  define the DC voltage on  $OUT_A$ . The gate voltage of M3 (node  $GN$ ) is adjusted in a way that it sinks the current  $I_{BIAS} + I_{THR}$ . M2 is a cascode transistor used to prevent capacitive coupling between the analogue output  $OUT_A$  and the input, avoiding the Miller effect, and its gate can be connected to the same  $GN$  node. When a particle crosses the sensor, the voltage on  $OUT_A$  rises, eventually forcing M6 out of saturation and forcing  $I_{THR}$  to charge up the  $GN$  node. This results in a current increase through M3, which discharges the  $OUT_A$  node and brings it back to its baseline value. Note that here the capacitance  $C_S$  plays the role of not only the source capacitance of the follower determining the gain, but also the gate capacitance of M3 determining the return to baseline. The shape of the output signal can therefore be influenced by  $I_{BIAS}$ ,  $I_{THR}$  and the value of  $C_S$  in a way that the whole circuit acts as a band-pass filter with a certain shaping time. Therefore, no additional shaping is needed after the  $OUT_A$  node. An additional feature to shorten the analogue pulse duration on  $OUT_A$  for high input charges is the clipping transistor M4, which starts conducting only when the  $OUT_A$  voltage is above a certain value. This value can be controlled using the  $V_{CLIP}$  bias voltage.

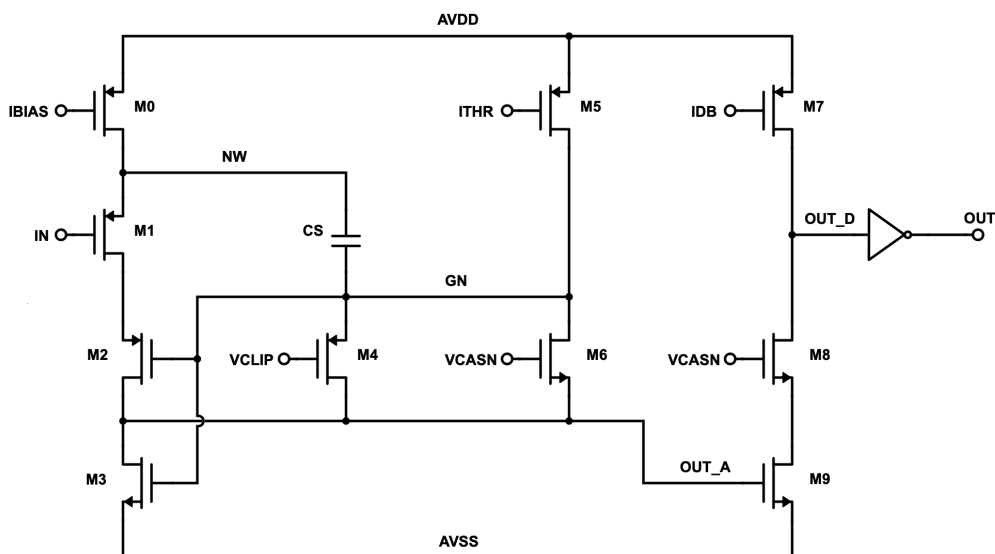


**Figure 3.9:** Schematic of the actual front-end circuit implemented in MALTA.

Transistors from M7 to M9 form a simple discriminator, which can be viewed as a common-source amplifier with a high gain. In steady-state conditions, the baseline voltage on  $OUT_A$  sets the DC current of M9 and the whole discriminator branch. M8 is again a cascode transistor to reduce the Miller effect from the discriminator output  $OUT_D$  to the amplifier output  $OUT_A$ . M7 is biased to provide a current  $I_{DB}$  higher than the DC current of the branch, but is pushed out of saturation while  $OUT_D$  is close to the supply voltage of 1.8 V. During the transient, when the  $OUT_A$  voltage increases, the current drawn by M9 increases to the point where it becomes larger than  $I_{DB}$  and starts discharging the  $OUT_D$  node. As the signal on  $OUT_A$  returns to its baseline value,  $OUT_D$  will be charged up again by the  $I_{DB}$  current. The threshold of the discriminator is therefore controlled by the combination of the DC current setting in the branch (so indirectly by  $V_{CASN}$ ) and the  $I_{DB}$  current setting. When the  $OUT_D$  voltage drops below the threshold voltage of the following inverter during the transient, a digital pulse is produced at the output of the front-end.

The additional features implemented in the analogue part include pixel masking and test pulse injection. The possibility of masking a pixel front-end is realised by adding three parallel NMOS transistors between to source of transistor M9 in the discriminator stage and the analogue ground  $AVSS$ . The gates of these transistors are connected to digital signals used to address the pixels that need to be masked. The addressing is done in a way that an address line is provided for each of the 512 columns, rows, but also diagonals in the pixel matrix. By tying one line in each of the three dimensions to ground, the three NMOS transistors in a single pixel will be disabled and the discriminator output will be permanently tied to a high level, so the front-end will never generate an output pulse. In other words, pixels at the intersections of the vertical, horizontal and diagonal masking lines tied to ground will be deactivated. In the case of masking multiple pixels, there is a chance of masking pixels which do not need to be masked simply because they are located on the intersection of lines tied to ground. The diagonal coordinate is needed to reduce the number of these unintentionally masked "ghost" pixels.

In a similar fashion one can select the pixels which are enabled for test pulse injection. Here a diagonal line is not needed and the pixel is selected only by column and row selection bits. The logic involved is depicted in fig 3.10. The digital  $V_{PULSE}$  signal is propagated only to the selected pixels, where two PMOS switches are tying the output of the pulsing circuit to one of the two preset DC voltage levels:  $V_{HIGH}$  or  $V_{LOW}$ . On the rising edge of  $V_{PULSE}$ , transistor M0 is switched off and M1 is switched on, so the output signal is a voltage step with an amplitude of  $V_{HIGH} - V_{LOW}$ . This signal is then capacitively coupled to the input node of the front-end through a 230 aF metal-to-metal capacitor  $C_C$ . The amount of injected charge can then be calculated as:

$$Q_{IN} = C_{IN}\Delta V_{IN} = C_{IN}\frac{C_C}{C_{IN} + C_C}\Delta V_{OUT} \approx C_C(V_{HIGH} - V_{LOW}). \quad (3.2)$$

The injected charge is therefore roughly  $1.43 e^-$  per mV of difference between the  $V_{HIGH}$  and  $V_{LOW}$  DAC values.

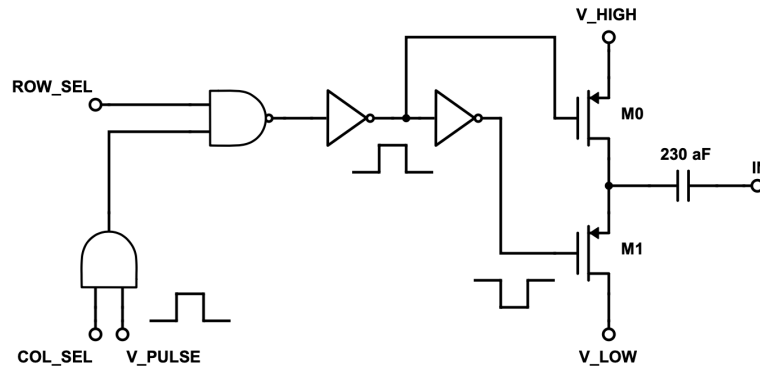


**Figure 3.10:** Circuitry used to capacitively inject a test pulse to the input of the front-end.

### 3.2.2 Timing optimisation

One of the major changes in the front-end amplifier compared to the one in ALPIDE is that a much faster signal rise time at the amplifier output needs to be achieved in order to meet the ATLAS requirement for the 25 ns time resolution. Therefore, the shaping time of the front-end has to be decreased from several microseconds to around 25 ns, which has far-reaching consequences for several design parameters, such as power consumption, noise and mismatch. To be able to achieve such a fast rise time, the total analogue power consumption has to be increased by about an order of magnitude, since the  $I_{BIAS}$  current in the main branch needs to be around 500 nA to achieve a sufficiently large transconductance  $g_m$  of the input device M1. Since this transconductance controls the current used to charge the  $OUT_A$  node in the initial moments after a particle hit, until  $C_S$  is discharged, the dimensioning of M1 is also critical: it needs to have a high  $W/L$  ratio for a high  $g_m$  and a total gate area large enough to avoid random telegraph signal noise (RTS). However, the gate area must also remain small enough not to dominate the input capacitance.

If M3 is made small enough, another effect becomes important, and that is the coupling from the M1 source (node  $NW$ ) to the M3 gate (node  $GN$ ) through the large capacitance  $C_S$ . When the voltage at the input drops,  $NW$  follows and via this coupling causes the  $V_{GS}$  of M3 to drop by several millivolts, effectively switching off M3 and again providing more current to charge  $OUT_A$ . Because of this, the  $g_m$  of M3 also becomes important, so a large width of the device is desirable. However, all the devices connecting to  $OUT_A$  need to be kept quite narrow in order to limit the increase of the parasitic capacitance on this node, which deteriorates not only the gain but also the timing of the amplifier. For the same reason, the width of the discriminator

input M9 must not be increased too much, even though the high  $g_m$  of this device is favourable for the time response of the discriminator stage.

Keeping all this in mind, the transistors in the front-end are dimensioned to give the best possible timing performance for a 500 nA bias current. Note that the total power consumption of the front-end is some 10% higher due to the additional DC current in the second branch ( $I_{THR}$  is typically only a few nA) and the discriminator branch (typically a few tens of nA). However, with a supply voltage of 1.8 V, this still gives less than 1  $\mu\text{W}$  of analogue power consumption per pixel, which is far below any specification and at least an order of magnitude below large collection electrode designs with similar shaping times [68]. The total analogue power consumption is then around 75  $\text{mW}/\text{cm}^2$ . A simulation of the transient waveforms at the input, analogue output and discriminated output of the front-end with the charge threshold set to 200  $e^-$  is shown in fig. 3.11. This threshold has been chosen to maintain full detection efficiency with a Landau peak of around 1500  $e^-$ , taking into account potential charge sharing between 4 pixels and some charge loss after irradiation. The solid line shows the response for a collected charge of 300  $e^-$ , the dashed line for a charge of 3000  $e^-$ . The simulation was performed by modelling the input signal as a trapezoidal current pulse with a width of 1 ns, assuming a charge collection time around that value. The sensor is modelled as a leakage current source in parallel

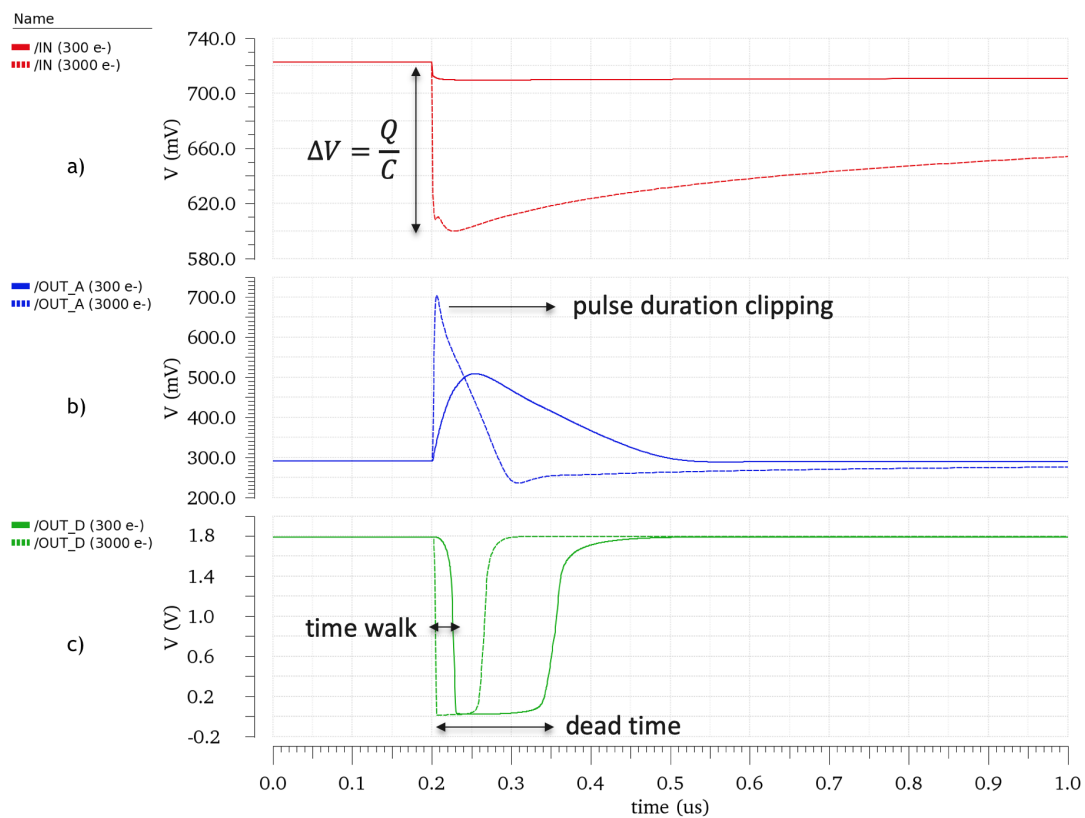


**Figure 3.11:** Simulated transient response of the MALTA analogue front-end circuit: (a) signals at the sensing node, (b) signals at the output of the amplifier, (c) signals at the output of the discriminator.



with a capacitance of 2.5 fF, which is a value previously measured on prototype chips [69]. The simulation also takes into account all the parasitic routing capacitances, which have been extracted from the pixel layout.

The red curves show that the initial voltage step at the input is proportional to the charge, and after the charge is collected the input node is slowly reset to its initial voltage (in this case with a diode). The blue curves show the amplified signals at  $OUT_A$ . Notice that the pulse duration is actually shorter for an input charge of  $3000 e^-$ , which is a result of the signal clipping mechanism described earlier. When the signals exceed a certain voltage level for which  $I_{M9} > I_{DB}$ , the discriminator fires, as seen in the green curves showing the discriminator output signals. Here one can observe two quantities important to describe the timing characteristics of a pixel front-end. One is the dead time, which is basically the duration of the discriminated pulse. During this time, the front-end is insensitive to any new particle hits within the same pixel, since they will not produce a new pulse and therefore will not be detected. Avoiding this analogue pile-up is the main reason to limit the duration of the discriminator pulse. For the simulated front-end settings, the maximum pulse duration is around 200 ns, which results in negligible pile-up rates for hit rates in the outer pixel layers of ATLAS. The other important quantity is the time walk, which describes the time difference in the leading edge of the discriminator pulse for different amounts of charge collected. If no correction is made for it, the time walk is the number that determines the time resolution of the front-end, and one would like to keep it below 25 ns for this application. The red curve in figure 3.12 shows the simulated time walk curve, i.e. the delay of the discriminator leading edge versus the collected charge.

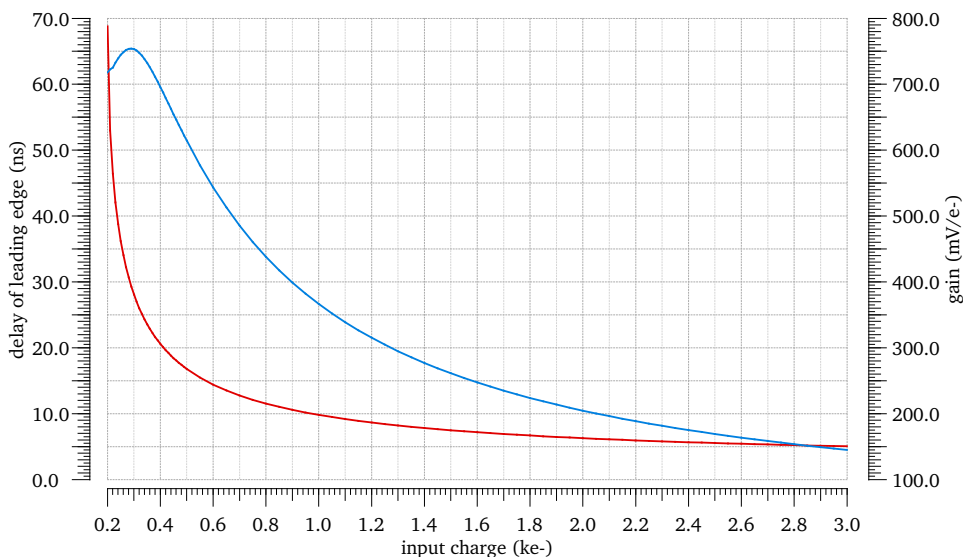


**Figure 3.12:** Simulated time-walk and gain curve for the front-end. The in-time threshold extracted from the red curve is  $285 e^-$ .



For charges very close to the threshold, this delay exceeds the 25 ns mark, but in this simulation, already 85  $e^-$  above the threshold the delay is within 25 ns of the minimum possible delay. This means that all charges above 285  $e^-$  will be detected within the required time window. This in-time threshold is a number often used to summarise the timing performance of detectors at the LHC. Again, with a most probable charge deposition value of 1500  $e^-$ , an in-time threshold of 285  $e^-$  should give very close to full in-time efficiency for the detector.

The blue curve in 3.12 shown the gain of the amplifier expressed in mV per  $e^-$  of input charge. The circuit has a non-linear gain characteristic and the analogue output saturates already above approximately 300  $e^-$  of input charge for these settings, partly due to the clipping transistor starting to conduct significant current. The gain is high enough to be able to achieve the desired low operating charge thresholds by tuning the discriminator threshold, even down to 100  $e^-$ , which would even further improve the in-time efficiency of the circuit.

### 3.2.3 Noise and mismatch

Equation 2.21 discussed in sect. 2.3.1 concerning the thermal noise of the input transistor is also valid for this circuit. The small sensor capacitance and high transconductance of the input device inherently provide a good noise performance. The current sources are all made narrow and long to reduce their noise contributions. To check which devices contribute to the total noise seen at the output of the amplifier, a linearised AC noise analysis is performed at threshold. Note that even with the non-linear transfer function evidenced by fig. 3.12, this analysis gives fairly accurate results for charges close to threshold. The results are summarised in table 3.1.

**Table 3.1:** Simulated noise contributions of transistors in the front-end.

Device	Noise type	Noise contribution (mV <sub>RMS</sub> )	Percentage of total (%)
M1	thermal noise	3.29	38.21
M3	thermal noise	2.83	28.09
M3	1/f noise	2.34	19.19
D1	shot noise	1.18	4.87
M6	thermal noise	1.09	4.17
M5	thermal noise	1	3.52

The thermal noise of the input device M1 is indeed the dominant contributor. Apart from the thermal noise, the 1/f noise (attributed to imperfections and the generation/recombination of charge carriers in the channel) of M3 also has a non-negligible contribution due to the gain mechanism described earlier. D1 represents the shot noise of the reset diode, which is associated with fluctuations when a current flows across a p-n junction, and is proportional to the

current flowing through the device, in this case the sensor leakage current. The simulation was performed with a leakage current of 10 pA, which is an overestimation before irradiation, but the leakage current of irradiated sensors might even exceed that value, especially at room temperature, where the shot noise could become the dominant contributor. To include the shot noise of the sensor diode, one also needs to multiply this value by roughly  $\sqrt{2}$ . The RMS value of the total equivalent noise voltage on  $OUT_A$  is calculated to be 5.22 mV. When compared to the signal amplitude at threshold, which is simulated to be 143.59 mV, a signal-to-noise ratio of 27.5 is obtained.

For a more accurate estimation of the equivalent noise charge referred back to the input and the  $S/N$ , a transient noise simulation can also be performed. By sweeping the input charge around threshold, running multiple simulations for each charge and looking at the probability of a discriminator hit occurring for a given charge, a noise S-curve shown in fig. 3.13 is obtained. This curve is essentially the integral of the Gaussian noise distribution around threshold. Therefore, the 50% value of the probability curve gives the mean threshold value, while the RMS of the normal noise distribution represents the ENC. As expected, the mean threshold value is close to  $200 e^-$ , while the ENC is around  $7 e^-$ . This gives an  $S/N$  of 28.8, which matches the results of the linearised analysis fairly well. One can conclude that an even lower operating threshold than  $200 e^-$  should indeed be possible, since with any threshold larger than  $10\sigma$  of the noise one should expect close to no noise hits even in a large pixel matrix.

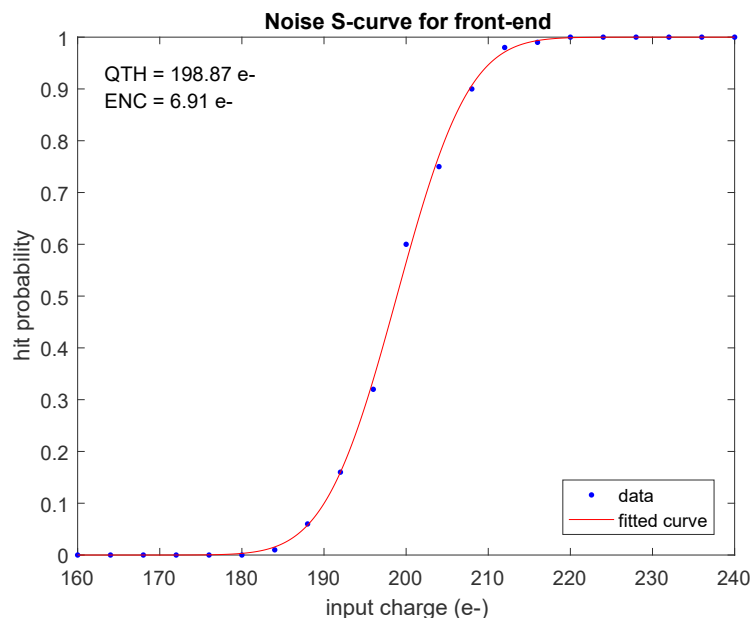


**Figure 3.13:** Simulated noise S-curve for the front-end. The RMS value of the fit yields an equivalent noise charge of around  $7 e^-$ .

A similar type of S-curve can be obtained when simulating the pixel-to-pixel differences between front-ends due to random process variations and transistor mismatch. The mismatch

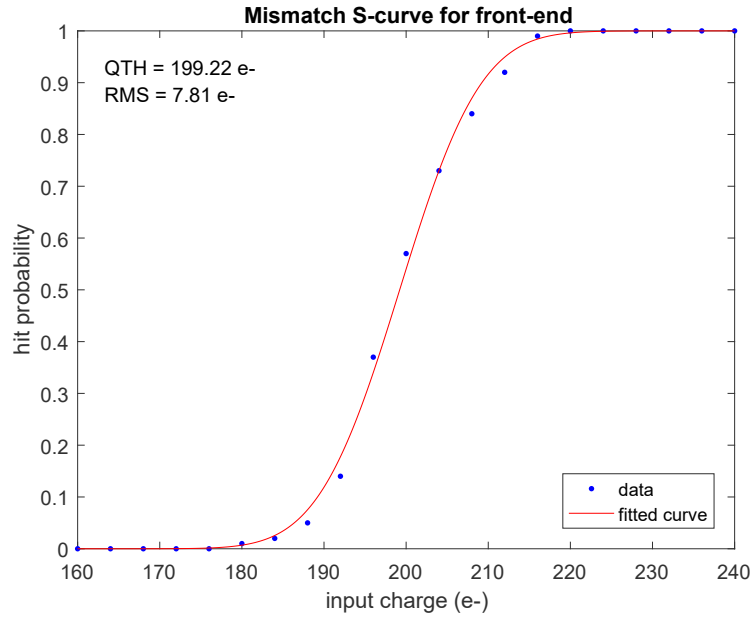


**Figure 3.14:** Simulated mismatch S-curve for the front-end. The RMS value of the fit yields around  $8 e^-$  of threshold variation at a  $200 e^-$  threshold.

S-curve obtained in Monte Carlo simulations using the models for threshold voltage variation provided by the foundry is shown in fig. 3.14. In this case, the RMS value of the curve represents the charge threshold variation between pixels and is close to  $8 e^-$  in this simulation. To obtain such a low threshold variation, special care needs to be taken of the sizing of critical devices. From theory, it is well-known that the threshold voltage variation  $\sigma_{V_{TH}}$  of transistors scales with  $1/\sqrt{WL}$  [70]. Therefore, to reduce the total variation in the circuit one has to increase the total area of critical devices. In the case of the front-end discussed here, these devices are mainly M5 and M6. The  $I_{THR}$  current of M5 has a big influence on the gain of the amplifier, and both these devices are defining the DC current of the discriminator and hence its switching threshold. This is made even more prominent by the fact that these two devices work with very low currents and in weak inversion, where the conversion from threshold voltage variation to current variation is exponential. For this reason, M5 is by far the largest transistor in the front-end layout with a total area of  $20 \mu\text{m}^2$ . M6 should not be increased to that extent because of the capacitance penalty on  $OUT_A$ , but an area of  $1 \mu\text{m}^2$  is a good trade-off. This leaves M3 and M9 as the dominant sources of charge threshold variation, but again, these have to be kept quite small not to load the  $OUT_A$  node too much.

Since the simulated threshold variation is already very low and comparable to the noise levels, the decision has been made not to include any per-pixel threshold tuning capabilities in the pixel matrix. Therefore, only the global threshold value of the chip can be tuned using the various DAC settings for the front-end.

### 3.2.4 Considerations for radiation hardness

As mentioned earlier, to keep the front-end functional even after high non-ionising fluences, one has to make sure that the input stages of the front-end can operate in a wide range of sensor leakage currents. The expected leakage current values after irradiation to  $10^{15}$  n<sub>eq</sub>/cm<sup>2</sup> are in the range of several hundreds of picoamps at room temperature. Even though the detectors are operated at a low temperature of  $-30^{\circ}$ , this needs to be taken into account during the design. In particular, the range of the  $I_{RESET}$  current used in the sectors with PMOS reset needs to be high enough to go beyond these leakage values. As for the diode reset, for high leakage currents the reset diode becomes highly conductive and can reset the input signal too quickly, clipping the voltage signal and effectively causing part of the signal to be lost. At a leakage current of 100 pA, however, the loss in signal because of this clipping effect is only about 5%, so at low temperatures this is not an issue. The  $V_{RESET\_D}$  voltage also provides a handle to tune the DC voltage at the front-end input, giving sufficient margin to keep all transistors in the first branch in saturation for a wide range of sensor leakage currents.

As far as tolerance to ionising radiation is concerned, it is important to make sure that transistor leakage currents induced by positive trapped charge in the field oxide do not affect the operation of the circuit significantly. The changes in drain current are not likely to affect the behaviour of devices conducting currents of tens or hundreds of nanoamps. However, since the  $I_{THR}$  current can be even below 1 nA, M5 and M6 are again the devices most sensitive to TID. Leakage current increases in the order of 100 pA have been measured for minimum size NMOS transistors in the TowerJazz 180 nm technology after 20 Mrad of TID [71]. The expected ATLAS levels are a factor of 3-4 higher than that, so the M6 NMOS transistor in the sensitive  $I_{THR}$  branch could well be affected. Because of that, this transistor is implemented with an enclosed layout. This introduces an additional constraint on the sizing of this device, since the width is no longer independent of the length. Therefore, quite a wide device has to be used to limit its threshold voltage variation, which increases the capacitance on the analogue output and brings a slight penalty in terms of speed. A p+ guard ring is also added around the device to prevent any leakage to neighbouring devices, which more or less doubles the area required for this transistor. However, it is a necessary step to ensure sufficient radiation hardness of the front-end up to the required 50 Mrad of TID.

### 3.2.5 Bias generation using digital-to-analogue converters

The current and voltage biases for the front-end are generated using 7-bit digital-to-analogue converters. The basic operating principle of the current DACs is shown in fig. 3.15. A reference current  $I_{REF}$  of 140 nA is generated using a simple current generator with a diode-connected PMOS transistor M0 in series with a 60 k $\Omega$  resistor. This current is then mirrored to 127 DAC

units. Each unit contains a transmission gate switch, S1, which is open or closed depending on the desired DAC code. The 7-bit code is stored in registers at the digital chip periphery, and is thermometer encoded to close the number of switches corresponding to the decimal value of the binary code. The configuration registers are triplicated to prevent single-event upsets. All 127 units are connected to the drain of a diode-connected NMOS transistor M2, so the current of all units where S1 is closed is summed up and mirrored to one or two more stages. The mirroring ratio in these stages determines the final range and current step (or least significant bit, LSB) of a particular DAC. All NMOS transistors in these mirroring stages have an enclosed layout to avoid leakage problems after TID. For the same reason, all the current sources in the front-end are PMOS transistors, so the last mirroring stage contains the PMOS transistor M4, whose gate/drain is then connected to the gates of current sources within the pixel matrix. Even though the DAC uses its own power supply domain, the source of this last PMOS is connected to the analogue supply of the matrix in order to avoid any current variation due to the voltage drop along the supply lines in the matrix. Since the power pads are distributed along the left and right side of the matrix, the vertical voltage drop between rows should be negligible. However, with a current consumption of 500 nA/pixel and a width of 8.5  $\mu\text{m}$  available for the horizontal metal lines used for power supply routing, a voltage drop of around 6 mV is estimated, which could cause a significant current and charge threshold mismatch. Therefore, compensation for power supply voltage drop by means of using the matrix supply domain for the last mirroring stage is necessary to avoid a systematic threshold gradient along the matrix width.

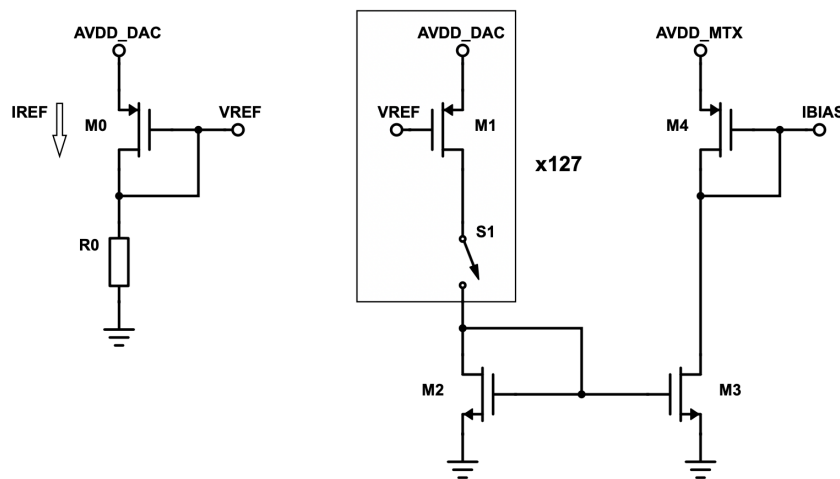


**Figure 3.15:** Operating principle of the current DACs in MALTA. The reference current is mirrored with a certain ratio to give the desired bias current values.

The voltage DACs are implemented as a string of resistors connected between power supply and ground, as seen in fig. 3.16. This gives an LSB of  $1.8/127 = 14.2$  mV for all the voltages. Again, the DAC code is stored in triplicated registers, but this time one-hot encoded to close only one out of the 128 switches, thus choosing the desired voltage value within the resistive

divider. This voltage is either connected directly to the transistor gates within the pixel matrix, or buffered with a source follower in case a significant current needs to be provided (like e.g. the reset voltages which need to be able to source the full sensor leakage current for all pixels).

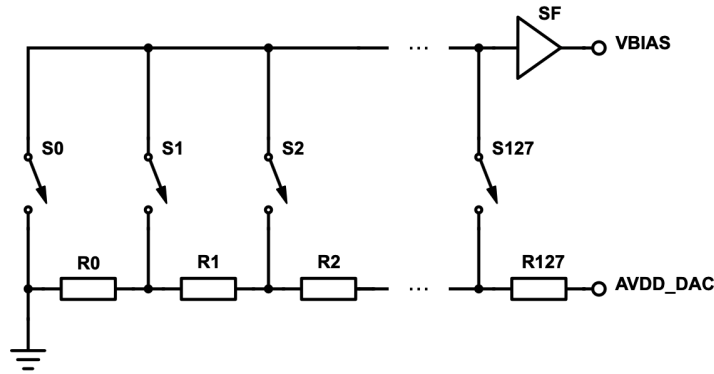


**Figure 3.16:** Operating principle of the voltage DACs in MALTA. Some of the voltages are buffered with a source follower before connecting to the pixel matrix.

An exception among the voltage biases is the  $V_{CASN}$  voltage for M6 in the front-end. For this voltage, a compensation for voltage drops along the ground line is needed, since with the same  $V_{CASN}$  over the full matrix this would cause a difference in the  $V_{GS}$  of transistor M9 in the front-end, resulting in a significant threshold gradient for the discriminator. A simple circuit implemented to carry out this compensation is shown in fig. 3.17. An  $I_{CASN}$  current is used generate the  $V_{CASN}$  voltage through two diode-connected NMOS transistors. Both the power supply and ground of the circuit are connected to the analogue supply and ground of the matrix. With appropriate dimensioning of the transistors in the circuit and assuming  $I_{CASN} \gg I_{THR}$ , the generated  $V_{CASN}$  will adjust the steady-state current in the discriminator stage of the front-end to approximately match  $I_{CASN}$  regardless of any voltage drops on the ground line. For this to

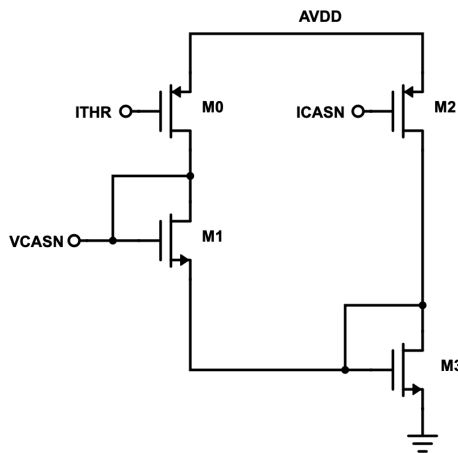


**Figure 3.17:** Circuit used to generate the  $V_{CASN}$  bias voltage from the  $I_{CASN}$  current.

work, M1 and M3 in the biasing circuit need to see the same bulk voltage as the corresponding transistors in the front-end, and hence their bulks need to be connected to the p-well potential of the matrix. This way, the DC current and threshold of the discriminator will not change significantly with voltage gradients on the ground line nor changes in the p-well bias.

An additional safety feature implemented for all DACs is the possibility to monitor and/or override the internal DAC values through a special set of pads. This allows to measure the current and voltage values generated by the DACs to perform e.g. DAC linearity checks. It also allows to force the currents and voltages externally in case of a problem in the operation of the DACs or the configuring logic.

## 3.3 Digital readout electronics

### 3.3.1 Asynchronous matrix readout

The MALTA chip uses a novel asynchronous digital readout architecture without propagating a clock to the pixel matrix in order to reduce the digital power consumption. For the readout, the  $512 \times 512$  pixels in MALTA are organised in double columns, and within a double column in sets of 2 (columns) by 8 (rows). Alternating sets of 16 pixels are connected to two output buses per double column, as depicted in fig. 3.18 [57]. When a discriminator of a pixel within a set of 16 pixels is fired, it activates a reference or hit signal, the one line out of 16 corresponding to the hit pixel, and the 5-bit group address corresponding to the set of 16 pixels where the hit was detected. A pulse with a length programmable to 0.5, 0.75, 1 or 2 ns is transmitted in parallel on every line which needs to transmit a logic one. The delay in the transmission line is matched between the different lines on the bus, and the total number of lines per bus is 22 (1+16+5). In case charge is shared between two or more pixels in a group, a hit arbitration is performed within the group to ensure that the hit data of all fired pixels is transmitted correctly. If the discriminators of two pixels fire simultaneously, two corresponding lines are activated and only one word is transmitted on the bus. If the pixels receive a sufficiently different amount of charge and the discriminators react one after the other, two words are transmitted sequentially over the bus, guaranteeing sufficient separation of the pulses on the bus for proper transmission. The groups of 16 pixels in a double column are alternated between the two output buses (red and blue in fig. 3.18) to prevent data collisions if a particle hits at or near the boundary between two different groups. Data is transmitted almost instantaneously, and is therefore available at the periphery only a few nanoseconds after the hit took place. The readout of each double column is completely independent of the others, so that multiple columns can transmit data at the same time. This massive parallelism in the matrix provides a very high bandwidth necessary for high-rate applications [72].

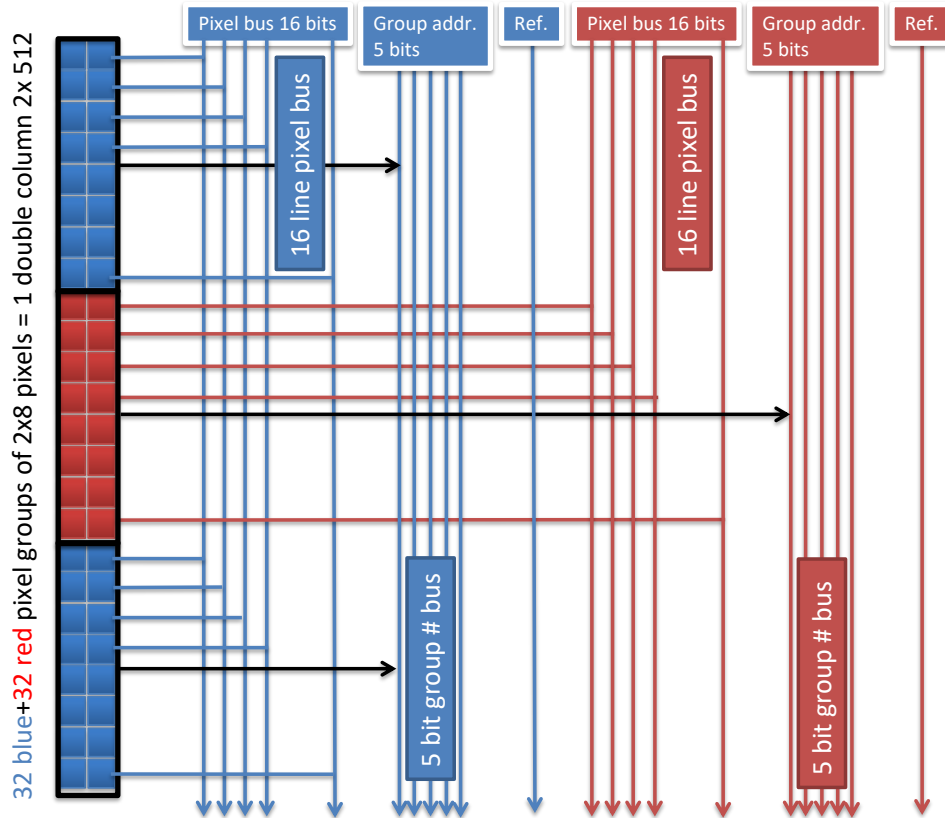


**Figure 3.18:** Organisation of a double column in the MALTA digital readout architecture [57].

Knowing the average number of bits toggling to be 4.5 (1 reference bit, 1 pixel bit and an average 2.5 out of the 5 group bits), one can calculate the power consumption needed to transmit the matrix data for a given hit rate. An example of this is shown in table 3.2, where the digital power consumption is calculated for the expected hit rates in different layers of the ATLAS ITk [73]. The energy needed to toggle 1 cm of line can be calculated as  $CV^2$ , which in this technology yields 6.5 pJ/cm. Multiplying this by the expected hit rates and average number of toggles gives an estimate of the total digital power consumption needed for the asynchronous readout of the MALTA matrix.

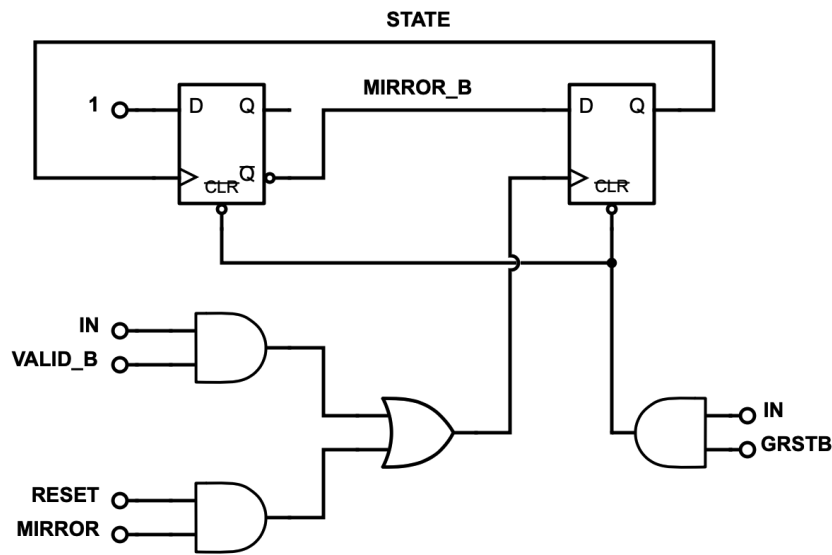
**Table 3.2:** Matrix readout power calculated for different hit rates (reproduced from [73]).

Layer	Pixel hit rate (MHz/mm <sup>2</sup> )	Power/bit (mW/cm <sup>2</sup> )	Matrix readout power (mW/cm <sup>2</sup> )
0	27.2	17.7	79.6
1	8.4	5.4	24.6
2	1.72	1.1	5.0
3	1.16	0.8	3.4
4	0.84	0.5	2.5

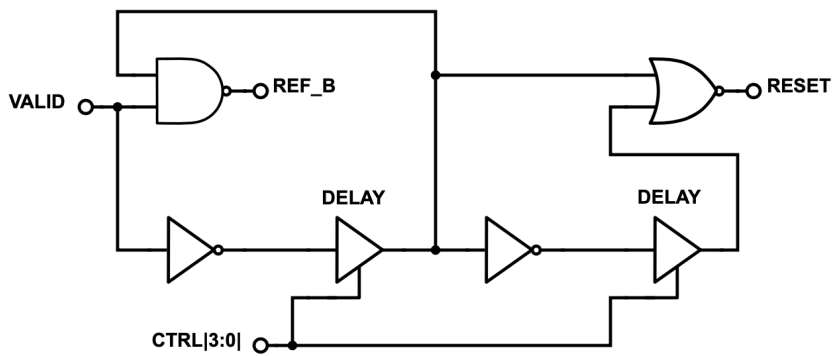


For comparison, the power needed to transmit a 40 MHz clock over 1 cm<sup>2</sup> with a pixel pitch of 36.4 μm using the same calculation is found to be 36 mW/cm<sup>2</sup>. This doubles if the clock signals are transmitted differentially, which is often the case to achieve better robustness of the signal transmission. It is evident that the power for the clock transmission itself is comparable to the readout power even for the highest hit rates in the innermost pixel layers, and is more than an order of magnitude higher than the readout power in the outer layers. Therefore, the asynchronous approach does provide a significant power reduction.

The in-pixel logic used for the generation of the transmitted pulses and for hit arbitration in case of multiple hits in a group is shown in fig. 3.19. When the front-end detects a hit and produces an output pulse (node *IN* for the digital readout logic), a logic one will be latched by the D flip-flop on the right in the double flip-flop structure shown in fig. 3.19a, since the initial value of the *RESET*, *MIRROR* and *VALID* signals is 0. The *STATE* signal goes to a high level and a logic one is latched by left flip-flop, causing *MIRROR* to go to a high level as well. The



(a)



(b)

**Figure 3.19:** A simplified view of the in-pixel readout logic implemented in MALTA: (a) double flip-flop structure for hit arbitration (b) pulse generator circuit used to generate the reference pulse.

*VALID* signal is in common for all the pixels within a group of 16, and goes to a high level if any of the *STATE* signals for the 16 pixels are high, disabling the latching of further hits until the first hit is read out. It also starts the generation of the reference pulse in the circuit shown in fig. 3.19b. The *VALID* signal is inverted, delayed and then combined with the original signal to obtain a short pulse on *REF\_B*, which is the inverted version of the reference pulse transmitted down the column. The procedure is repeated once more to obtain a similar pulse on *RESET* immediately after the reference pulse. The duration of the reference and *RESET* pulses can be tuned using 4 control bits which act on the number of delay stages used within the delay cells, resulting in a pulse width between 500 ps and 2 ns. The reference pulse is combined with the *STATE* signals from all 16 pixels, generating the 16-bit pixel address, as well as 5 hard-wired group bits fixed for each of the 32 groups, which generates the 5-bit group address. Once the *RESET* pulse is generated, the and/or logic in fig. 3.19a will cause the *MIRROR\_B* signal, now a logic zero, to be latched by the flip-flop on the right, effectively resetting the *STATE* signal. The *MIRROR* signal will be reset as soon as the input signal goes down, and at this point the in-pixel logic will be ready to detect a new hit.

Note that if another pixel is fired within the same group and within a time window of around 1 ns with respect to the first fired pixel (typically because of two pixels collecting a similar amount of charge and their discriminators firing nearly simultaneously), the *STATE* signal will be generated for both pixels, and the two pixel address pulses will be sent with the same reference signal, as one data word. If the delay between input signals is larger than 1 ns, the *VALID* signal from the first hit will have already blocked the generation of the *STATE* signal for the second hit, so this hit has to be read out in the next read cycle, with a second reference pulse. This is the case in the simulation shown in fig. 3.20. The second front-end output, *IN*[1], fires 1.5 ns after the first one, *IN*[0]. Therefore, the *STATE*[0] signal goes high first, closely followed by *MIRROR*[0] and *VALID*. Because *VALID* is high, another *STATE* signal can not be generated, and the *VALID* starts the pulse generation circuit, producing the *REF* reference pulse. This is combined with *STATE*[0] to produce the pixel address bit *PIX*[0], as well as the hard-wired group bits to produce the binary encoded group address. As the simulation is performed for group number 31, all five group bits will produce a pulse (only *GROUP*[0] is shown). The width of the pulses is set to 1 ns. The *RESET* signal will cause the *VALID* signal to go to a low level, now allowing the generation of the *STATE*[1] signal for the second fired pixel. Again, the correct pixel address, *PIX*[1] is transmitted, and the *STATE* and *VALID* signals are back to their initial value. The *MIRROR* signals will be reset with the falling edge of the input signal, which in this case occurs after 100 ns, outside the simulation window.

The pulses generated in the pixel are transmitted down the column using a special buffering structure, shown in fig. 3.21. The input in this case is any one of the 22 reference/address bits from the pixels (the buffering structure is the same for all the bits). As mentioned, there are two

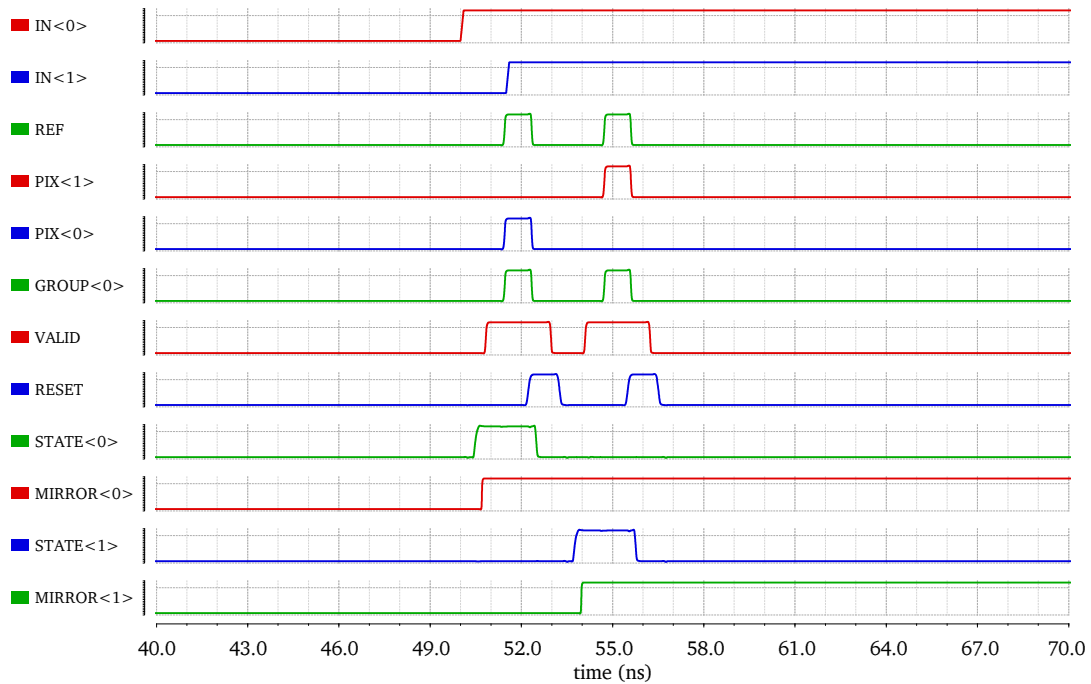


**Figure 3.20:** An analogue simulation of the signals in the in-pixel readout logic in the case of two pixel hits within the same group separated in time by 1.5 ns. Two reference signals of 1 ns width are sent down the column.

separate 22-bit buses for alternating groups of pixels: the "blue" groups (A) or the "red" groups (B). In each "blue" group, the pulse is injected into one input of a NAND gate, while the other input is used to propagate pulses coming from higher up within the matrix. The output of this gate is then inverted in the next "red" group to achieve the correct polarity of the signals when they reach the next "blue" group. The procedure is repeated over the full height of the column, and is analogous for pulses generated in the "red" groups.

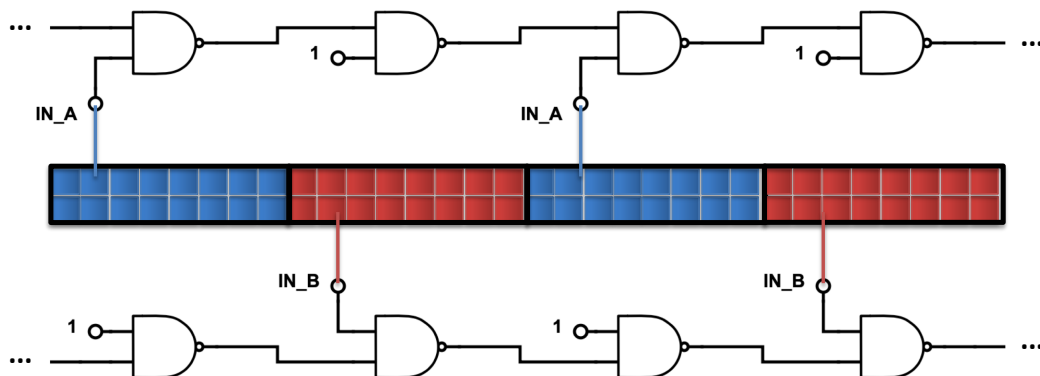


**Figure 3.21:** Chain of NAND gates used to buffer the signals down the column.

A critical goal in the signal propagation down the column is to preserve the pulse width and the alignment of pulses on different lines of the bus. To achieve that, a special routing structure

needs to be used to exactly balance the capacitances at the output of each NAND gate. This means not only using routing lines of the same width and length, but also distributing them equally over the different metal layers, since different layers will see a different capacitance e.g. to the top metal used for power routing. Even a small difference in capacitance causes a delay difference between different bits which accumulates over the full height of the matrix and can cause pulses of the same word to reach the end-of-column significantly misaligned in time. Another concern is that if neighbouring lines are transmitting pulses simultaneously, they effectively see a smaller capacitance compared to other lines. Because of that, one has to make sure that neighbouring pixels, which could transmit simultaneous signals if they belong to the same cluster caused by charge sharing, never use neighbouring lines for the transmission. In the case of the group bits, the appearance of simultaneous pulses on the lines can not be avoided, so these lines are shielded from one another. To avoid the deformation of pulses during the transmission, one not only needs to balance the capacitances on the outputs of different NAND gates, but also the delay of the rising and falling edge of the signals. If this is not the case, the pulses could be significantly stretched or could even disappear completely by the time they reach the end-of-column, depending on which edge has a smaller propagation delay. This is the reason for using inverting gates (NAND instead of AND) in the transmission, and also why the simple inversion in the opposite groups is done using the same NAND gates with one input tied to a high level. This way, the rising edge in one NAND stage becomes the falling edge in the next, so the edge delays are balanced by design and do not rely on the sizing of the gates. In this case, changes in propagation delay caused by reverse bias on the bulks of NMOS transistors do not deform the pulses either.

Extraction of the routing capacitances from the layout of two consecutive groups shows a maximal capacitance difference between lines of less than 3%, resulting in a simulated maximal delay difference of around 150 ps over the full column height. On the other hand, the maximal deformation of the pulse width over the full column is only around 30 ps. As for the time it takes transmit a pulse over the full column, from the top group to the bottom of the matrix, this value is simulated to range from 7.2 ns without reverse bias on the p-well up to around 8 ns with a p-well bias of  $-1.8$  V.

### **3.3.2 End-of-column readout logic**

At the end-of-column, in the digital chip periphery, signals from the two buses for the "red" and "blue" groups are merged onto a common bus. For the case of simultaneous pulses on the two buses, an arbitration logic similar to the one in the pixel is implemented to give priority to one of the buses and delay pulses from the other bus. A delay counter bit is added to the address bits, which transmits a pulse together with the delayed address pulses to signify that there were simultaneous hits. This is done to be able to trace back the information about the time of arrival

of hits more precisely in case they need to be delayed. Since the MALTA architecture does not encode time-over-threshold information, but uses a so-called binary readout of the matrix, the time of arrival of hits can be useful to obtain relative information about the charge collected by pixels within a cluster (because of time walk, hits from pixels collecting a high charge will arrive before hits from pixels collecting charge values close to threshold). This is why it is important to keep track of the delays using the delay counter during this time-ordering process. An additional feature is the inclusion of another 2-bit counter running at 40 MHz used as a bunch crossing identifier (BCID). This allows the hits to be timestamped and resolved within 4 bunch crossings (100 ns), which can be a useful feature to test the timing properties of the chip. Finally, a group identifier bit is added to the data word, which indicates whether the hits came from a "red" group or a "blue" group.

This process of merging and delaying pulses is repeated in a binary tree-like structure, as shown in fig. 3.22, until hits from the full pixel matrix are merged onto a single bus. In each level, a double-column identifier bit is added, so that the final data word unambiguously contains the address of the hit pixel. In the second level, the delay counter is also expanded to 3 bits, increasing every time a pulse is delayed, which means that a pulse can be delayed by a maximum of 8 times in the 9 levels of merging. An additional tenth merger level is added for the possibility to merge signals coming from multiple chips (as mentioned, data can be transmitted from chip to chip through the CMOS data pads). Here, a 4-bit chip identifier is added, so that theoretically up to 16 chips can be connected together. This creates the final 40-bit output data word of MALTA, which contains 1 reference bit, 16 bits for pixel address, 5 for the group address, 1 group identifier bit, 3 bits for the delay counter, 8 for the double-column address, 2 for the BCID and 4 for the chip address. This is summarised in table 3.3. 40 parallel LVDS drivers are used to transmit the 40 signals off-chip. The drivers are designed to operate at up to 5 Gb/s with a peak-to-peak jitter below 30 ps, and are more than capable of transmitting even the shortest 500 ps wide pulses.

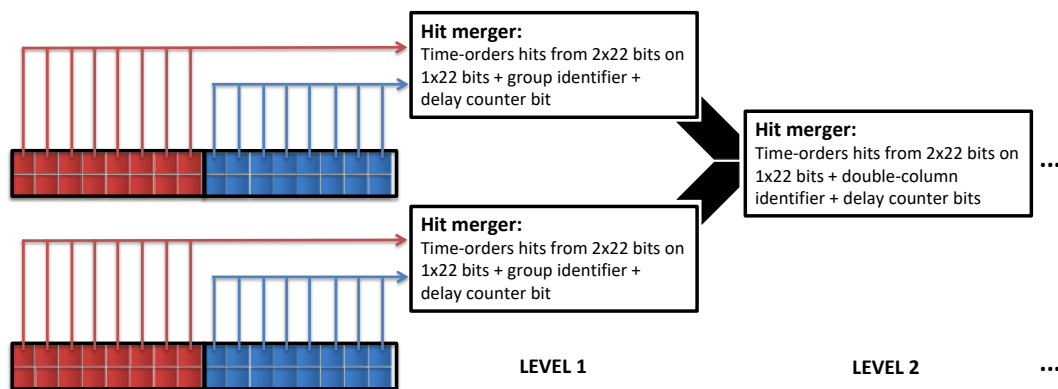


**Figure 3.22:** Organisation of the hit merging circuitry at the end-of-column.

**Table 3.3:** Bits of the final output word of MALTA.

Bits	Contents
0	Reference
1-16	Pixel address
17-21	Group address
22	Group identifier
23-25	Delay counter
26-33	Double-column address
34-35	BCID counter
36-39	Chip identifier

A simplified view of the logic used to merge and time-sort the reference pulses coming from the matrix is depicted in fig. 3.23. Two flip-flops are reserved for pulses coming from each of the two buses ("red" and "blue", A and B). This is done to be able to store consecutive pulses from a single bus in case the other bus has priority and data from it is being transmitted further. A toggle signal chooses the flip-flop used to latch the signals from each bus. This alternating storage allows the transmission of up to 6 consecutive pulses coming simultaneously from both buses before the logic is saturated. Similarly to the in-pixel logic, if any of the *STATE* signals

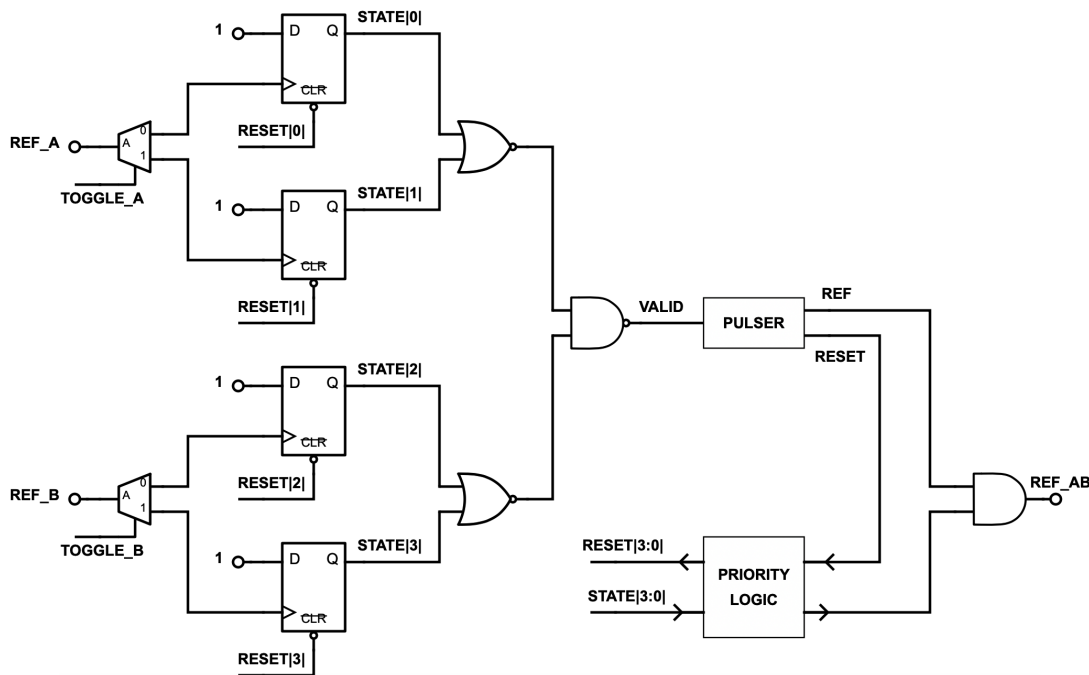


**Figure 3.23:** A simplified view of the logic used to merge and time-sort the incoming reference signals at the end-of-column.

is activated by latching an incoming reference signal, the *VALID* signal goes high and starts the pulse generator, which is the same as the one used in the pixel and shown in fig. 3.19b. The generated reference pulse is combined with a *STATE* signal chosen by the priority logic and transmitted to the next merger level. The priority logic also makes sure that the *RESET* signal resets the correct flip-flop, namely the one that was given priority for transmission. After that, the flip-flop is ready to latch another incoming pulse. The same logic is used to merge all the other address bits and transmit them to the next merger level.

As a backup feature, a much more simple way of merging the hits from the matrix is also included in the peripheral readout logic. This consists of a binary tree of OR gates for each bit, which basically merge all the pulses coming from the full pixel matrix, but without any arbitration in case of simultaneous hits. For reasonably low hit rates, this provides the same functionality as the more complicated merger logic. However, in the case of simultaneous hits appearing on multiple buses, combining the address bits with an OR gate will cause a corruption in the address data. Therefore, for high hit rates this mode of operation could cause data loss and hence a loss in detection efficiency.

## 3.4 Sensor characterisation before irradiation

### 3.4.1 Sensor and analogue performance in lab tests

The fabricated MALTA chips have been extensively tested in lab measurements and beam tests. The chips are wirebonded to a printed circuit board (PCB) and the LVDS data output is connected to an FPGA board used as a data acquisition system and interfaced with a computer where the data is stored.

An early test is to plot the I-V characteristics of the sensor. As already explained, in the modified process the additional n- layer isolates the p-wells of the electronics inside the pixel matrix from the p-type substrate of the sensor. Therefore, the two can be connected to different potentials, namely *PWELL* and *SUB*. However, if the difference between the two potentials is too large, the n- layer does not provide a sufficient potential barrier and a significant current flow can occur between the p-wells and the substrate. This is referred to as punchthrough. The I-V curves at room temperature, i.e. the currents measured on the *PWELL* and *SUB* nodes versus the reverse *SUB* voltage, and also for several reverse *PWELL* voltages, are plotted in fig. 3.24. At low absolute values of the *SUB* voltage, the leakage current is close to constant and is equal to about 4  $\mu\text{A}$  for the substrate and 100  $\mu\text{A}$  for the p-well at a p-well voltage of -6 V. Note that this includes not only the leakage current of the sensor diode, but also any other leakage between various wells on the whole chip. Above an absolute substrate voltage of around 25 V, a sharp increase in the *SUB* current and a sharp decrease (and change of sign) in

the *PWELL* current can be observed. This indicates that there is a current flow between the two nodes, which marks the onset of punchthrough. This typically happens at lower voltages than the breakdown voltage of the sensor junction, so in this case it is the punchthrough that limits the maximal sensor voltage that can be applied.

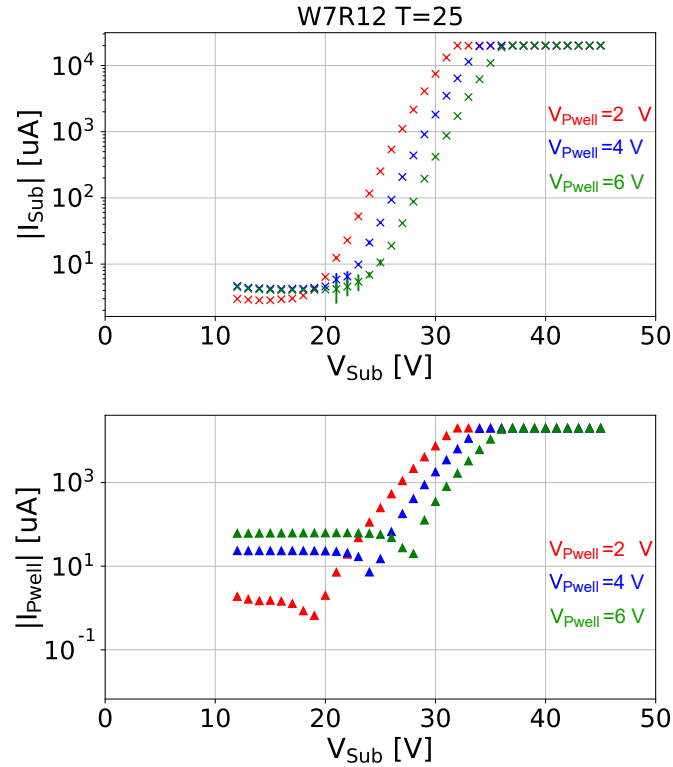


**Figure 3.24:** Sensor leakage current measured on the *SUB* and *PWELL* nodes with varying *SUB* voltage.

To test the performance of the analogue front-end, a special set of pixels has been included on the side of the matrix, which allows the monitoring of the analogue output signals ( $OUT_A$ ) of the front-end amplifier. The output signals are buffered and connected to a pad using two stages of source followers with a gain close to 1 and with a marginal effect on the  $OUT_A$  capacitance. The bias currents of the followers are adjusted to obtain a fast rise time, and the waveforms are monitored on an oscilloscope with a low-capacitance active probe, so as not to distort the signals. These monitoring pixels are available for both variations of the front-end circuit, namely the one with a diode reset and the one with a PMOS reset. Fig. 3.25 shows the amplitude distributions of the analogue output signals for the two flavours obtained during an exposure of the chip to an  $^{55}\text{Fe}$  radioactive source. The  $^{55}\text{Fe}$  isotope decays by emitting x-rays of two characteristic energy peaks: a K- $\alpha$  peak at 5.9 keV and a K- $\beta$  peak at 6.49 keV with a probability about 10 times lower than the K- $\alpha$ . These x-rays deposit a localised charge of  $1640 e^-$  and  $1800 e^-$  in the silicon sensor, respectively. The two peaks can clearly be seen in both amplitude distributions. For this measurement, the clipping transistor in the front-end



has been deactivated not to saturate the gain of the amplifier prematurely. The  $V_{RESET\_D}$  and  $V_{RESET\_P}$  settings were optimised for the highest gain, and all other settings were kept the same for the sake of comparison. Both the  $SUB$  and  $PWELL$  voltages were kept at  $-6$  V for this test. The K- $\alpha$  peak is shifted from about 406 mV in the diode reset sector to about 353 mV in the PMOS reset sector. This means that, for the same deposited charge of  $1640 e^-$ , the front-end with diode reset produces a factor of 1.15 higher signal than the one with PMOS reset, as expected due to the higher input capacitance introduced by the reset PMOS transistor.

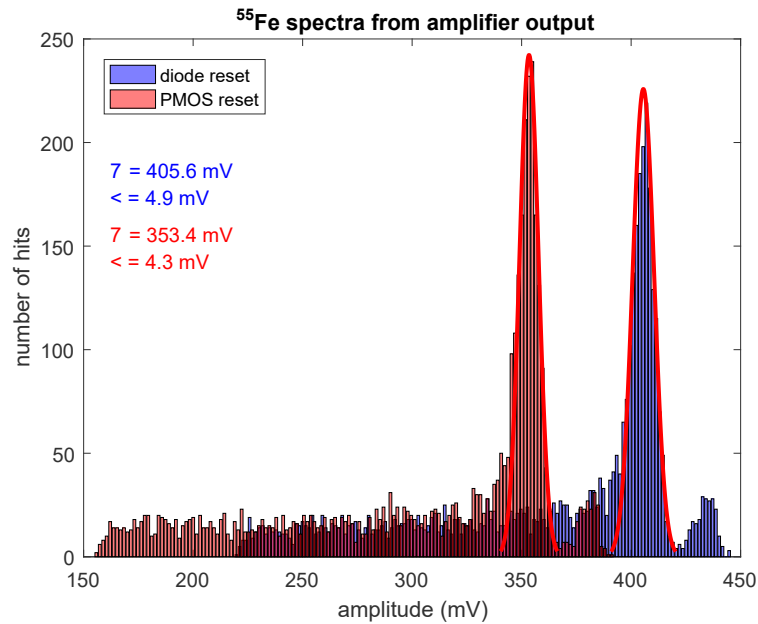


**Figure 3.25:**  $^{55}\text{Fe}$  source spectra obtained from the monitored analogue outputs of front-ends with diode and PMOS reset.

The width of the amplitude peak gives an estimation of the noise and the energy resolution of the front-end. After correcting for the Fano factor, which describes the resolution of the sensor itself (as mentioned in sect. 2.1), an RMS noise value of around  $14 e^-$  is obtained for both sectors. This is higher than the simulated noise values for the front-end, which is not surprising given that this includes the noise of the following buffer stages and the entire measurement setup. This converts to an energy resolution of about 120 eV full-width-half-maximum (FWHM) for the front-end, which is still in the same order as the resolution given by the sensor itself.

Another interesting measurement to be performed using the analogue monitoring pixels is to obtain the time walk curve of the front-end amplification stage, shown in fig. 3.26. This time, the waveforms are collected while exposing the chip to a  $^{90}\text{Sr}$  radioactive source, which emits electrons that generate a signal similar to the response to minimum ionising particles. Therefore, the expected most probable value of charge deposition for the  $25 \mu\text{m}$  thick epitaxial layer of the chip is around  $1500 e^-$ . The charge threshold setting of the front-ends with diode

reset during this measurement was around  $210 e^-$ . The  $y$ -axis shows the time it takes for the analogue signals to reach the discriminator threshold, while the  $x$ -axis gives the amplitude of the analogue pulse. One obtains a curve very similar to the simulated one shown in fig. 3.12, this time plotted versus signal amplitude rather than collected charge. The most probable amplitude value obtained by the most probable charge deposition of the MIP is around 500 mV. Looking at lower charge and amplitude values, signals above  $\sim 130$  mV of amplitude arrive within a window of 25 ns, which corresponds to an in-time threshold of about  $300 e^-$  for the front-end settings used. Around 5% of the hits in this plot are out of time ( $>25$  ns), but these are mostly hits caused by charge sharing, where the neighbouring pixels receive the majority of the charge, and therefore do not mean a direct loss of in-time efficiency. Note that the measurement does not include the delay of the discrimination stage, but since this delay is negligible already a few tens of electrons above threshold, the simulated number of  $285 e^-$  for the in-time threshold at a charge threshold of  $200 e^-$  matches the measurement results quite well.

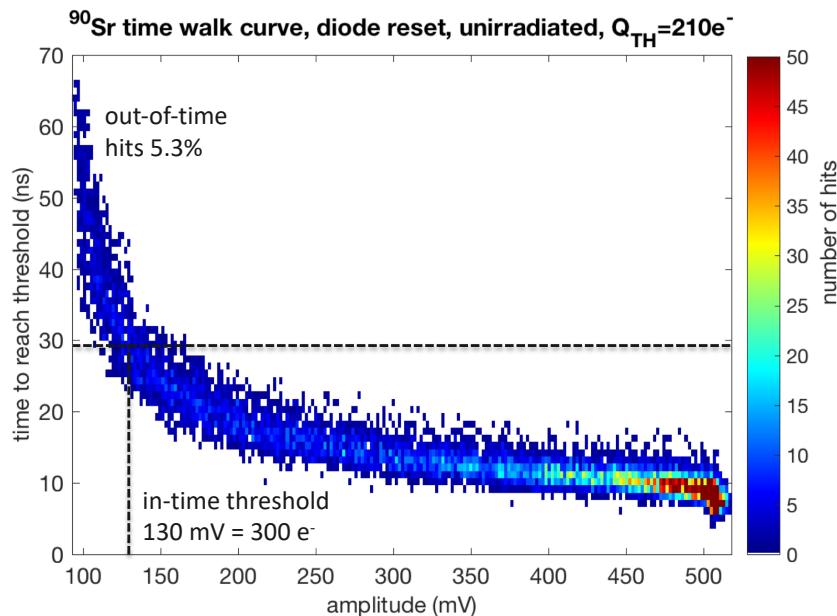


**Figure 3.26:** Time walk curve taken from a monitored analogue output during a  $^{90}\text{Sr}$  source test.

The pulse injection circuitry described in sect. 3.2.1 can be used to characterise the threshold and noise distributions of a multitude of pixels within the pixel matrix. By injecting different amounts of charge to a given pixel, one can obtain the noise S-curve of the pixel front-end (the simulated one is shown in fig. 3.13). This is done by setting the  $V_{HIGH}$  voltage to its maximum value and sweeping the  $V_{LOW}$  voltage, each time injecting a given number of test pulses and checking how many of the pulses were recorded by the FPGA readout. The transition between 100% of hits detected and no hits detected gives the threshold and noise of a particular pixel front-end. Note that due to a problem in the clock distribution in the configuration part of the digital periphery, the DAC values could not be configured reliably, so the measurement was

done by using an external power supply to force the value of the  $V_{LOW}$  voltage. Similarly, all the other DAC values used to tune the settings of the front-end were forced externally.

The results of this kind of threshold scan on nearly 3000 pixels with a diode reset are shown in fig. 3.27. Fig. 3.27b shows an example of an S-curve injecting a test pulse 1000 times for each value of  $V_{LOW}$ . The 50% value of the fit gives the threshold in millivolts of  $V_{LOW}$ , while the RMS gives the noise. This is then converted to electrons using the known value of the pulse injection capacitance. A distribution of the thresholds for different pixels with an  $I_{DB}$  voltage corresponding to a DAC code of around 10 is shown in fig. 3.27a.  $I_{DB}$ , which controls the discriminator threshold, is used as the main parameter to vary the charge threshold of the front-end, with all the other parameters set to achieve the highest gain. A distinction is made between the threshold distributions for different sectors, since the sectors with the "medium" deep p-well layout show a somewhat higher threshold than their "maximum" deep p-well counterparts, likely due to a larger input capacitance, because the n- region around the electrode is more difficult to deplete without any deep p-well nearby. The two sectors show a mean threshold value of 302 and 273  $e^-$  respectively. The  $I_{CASN}$  current and hence the  $V_{CASN}$  voltage are set to their lowest value for this scan, resulting in the lowest possible analogue baseline voltage. Increasing these values provides an additional handle to further lower the threshold if needed. However, it is noticeable that the threshold dispersion between the pixels is quite large, with an RMS value of around 34  $e^-$  for both sectors. This is a factor of 4 higher than the simulated value shown in fig. 3.14. The exact reasons for this large discrepancy are still under investigation, but it is likely that the mismatch models used for the simulation are somewhat optimistic in predicting the variations in the actual circuit. In particular, there are indications that the variation of the output conductance of transistor M3, which affects the gain of the front-end circuit, is significantly underestimated in the simulations, which will be discussed more in detail in sect. 5.1. In any case, a much higher than expected threshold variation in the order of 30  $e^-$  prevents

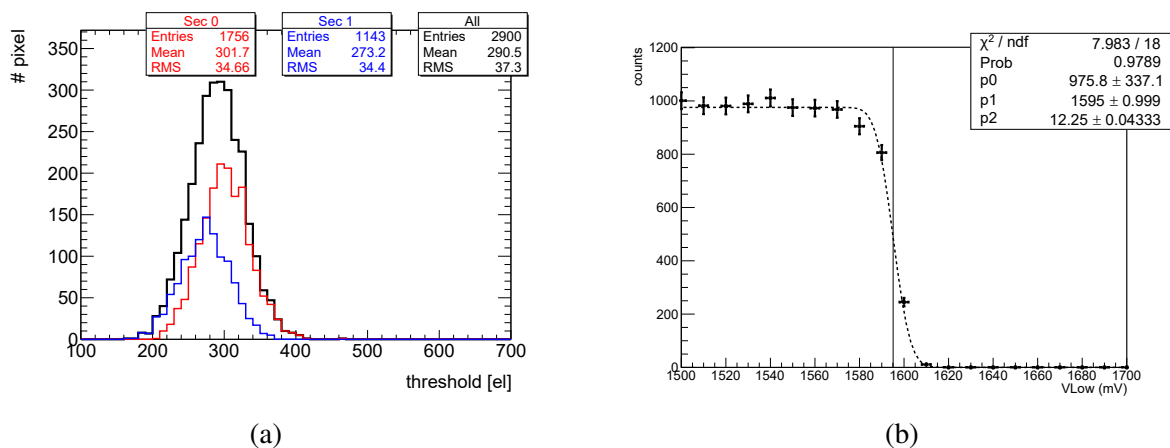


**Figure 3.27:** Threshold scan obtained using the in-pixel pulse injection circuit: (a) threshold distributions for two different sectors (b) example of an S-curve for a single pixel.

comfortable operation of the chip well below  $300 e^-$  of threshold, since the number of pixels with very low thresholds causing an excessive noise hit rate becomes large.

The noise distribution for the pixels obtained from the S-curve fits is shown in fig. 3.28. The mean noise value of around  $8 e^-$  matches the simulations in fig. 3.13 quite well. However, the noise does not quite follow a Gaussian distribution as one should expect. A small number of pixels shows a noise value well above  $10 e^-$ , which introduces a long tail in the noise distribution. A possible reason for this is RTS noise, which has been linked to the small dimensions of transistor M3 in the front-end. The trapping and de-trapping of carriers from a single trap, which is the cause of RTS noise, can be modelled as a voltage step on the M3 gate. Because of the high voltage gain from the gate of this device to the analogue output of the front-end, a small voltage step can cause significant noise on the  $OUT_A$  node. As a result, at charge thresholds below  $300 e^-$  a number of pixels needs to be masked in order to prevent a high noise hit rate. However, the configuration problems mentioned earlier also prevent the reliable masking of pixels. Due to the combination of all the effects described above, operating the chip reliably at the desired low thresholds of  $100\text{-}200 e^-$  is difficult, and one is forced to work with somewhat higher thresholds to contain the noise rates.

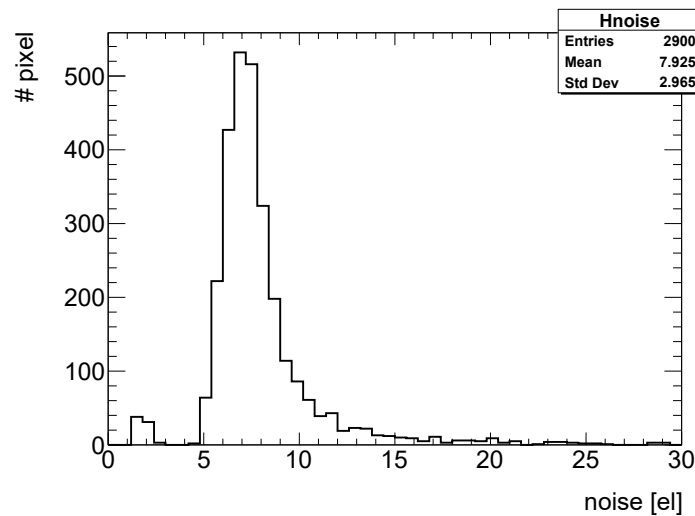


**Figure 3.28:** Noise distribution obtained using the in-pixel pulse injection circuit. The tail in the distribution is caused by random telegraph signal noise (RTS).

### 3.4.2 Measurements on readout architecture

The 40-bit digital chip output of the MALTA is read using a Virtex VC707 FPGA evaluation board. The 500 ps to 2 ns wide asynchronous output pulses are oversampled using a 320 MHz clock. The clock is shifted by 8 different phase values ( $45^\circ$ ,  $90^\circ$  etc.), and each of the 8 shifted clock signals is used to sample each of the MALTA outputs. This gives an effective sampling

frequency of 2.56 GHz, which is more than enough to sample the pulses if the pulse width is set to 1 ns or 2 ns. The duration of a sampling window is then around 390 ps, which gives the time resolution achievable using this readout system. A higher oversampling clock frequency can be used if one wants to work with the smallest possible pulse widths and obtain an even better time resolution. To test the functionality of the asynchronous oversampling firmware, another FPGA board was used to implement a transmitter which emulates the 1 ns wide pulses coming from MALTA. An example of sampling 300 of these pulses from the MALTA emulator on 36 bits, in this case with a 500 MHz clock used for testing, is shown in fig. 3.29a. Each pulse typically takes up 3-4 sampling windows and the pulses are aligned to within 2 windows. This alignment can be improved further by adjusting the delays of the delay modules added for each bit, achieving a near perfect timing alignment, as seen in fig. 3.29b. This delay correction ensures that the data words are read correctly even if there is a slight misalignment between the signals due to a capacitance difference stemming from e.g. different line lengths on the PCB or different paths within the FPGA.

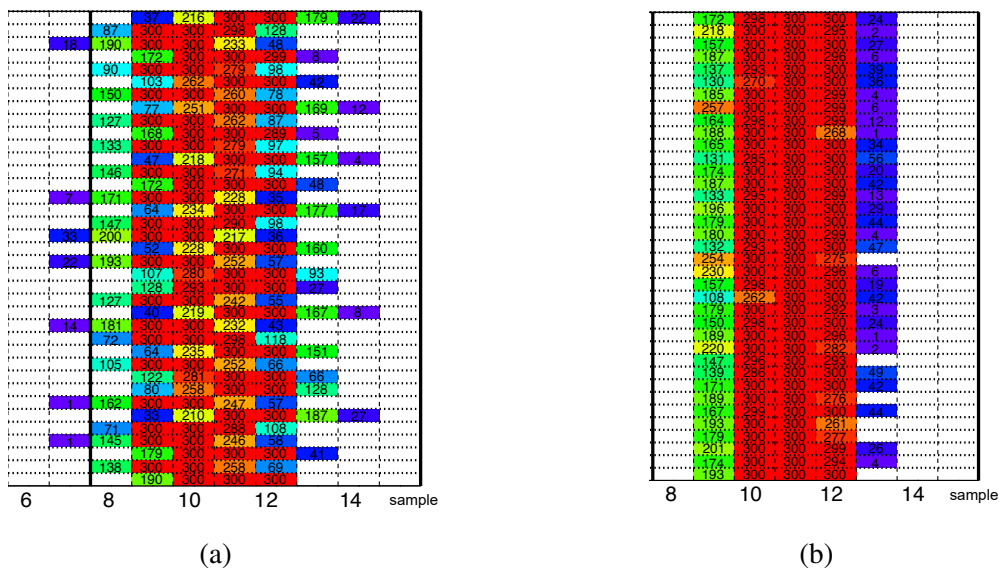


**Figure 3.29:** An example of sampling 300 pulses of 1 ns pulse width on 36 bits in the asynchronous oversampling firmware (a) before delay correction and (b) after delay correction.

With all this in mind, one can use the oversampling firmware not just to read out the address data coming from the chip, but also as a time-to-digital converter (TDC) to perform timing measurements on the MALTA pulses with a binning of 390 ps. One such measurement is the calculation of the propagation delay of the signals down the column. By injecting a test pulse to pixels at the top, middle and bottom of a column and measuring the delay between the three resulting reference pulses, the total delay, which includes the propagation of the test pulse up the column and the propagation of the signals down the column, can be obtained. The test pulse going up the column is buffered in every group of  $2 \times 8$  pixels using a buffer with a higher propagation delay than the NAND gates used to send the signals down the column. However,

assuming a simulated ratio between the two delays, one can calculate the signal propagation delay itself. Fig. 3.30a shows the analogue output of one pulsed pixel together with the three reference signals at the chip output seen on the oscilloscope. Note that due to problems in configuring the merger circuitry at the end-of-column, the backup option employing the OR logic was used to read out the matrix signals in this and subsequent measurements. Using the oversampling firmware, a distribution of the time of arrival of the three reference pulses is obtained after injecting the test pulse to the same pixels several thousands of times. Fig. 3.30b shows these distributions with respect to a fixed trigger signal coming from the FPGA, which marks the beginning of the data acquisition window. The mean timing difference between the reference pulse of the pixel at the bottom of the matrix (row 511, shown with the red curve) and the pixel at the top of the matrix (row 0, shown with the blue curve) is measured to be around 25 ns [74]. The total simulated delay for the test pulse propagation together with the signal propagation is 24.3 ns at a p-well bias of  $-1.8$  V. The measurement result matches the simulation result quite well, and the small discrepancy between the numbers can be caused by the fact that the measurement was taken at a p-well bias of  $-6$  V, where the simulation models are no longer completely reliable. Therefore, the simulated value of the signal propagation delay down the column of around 8 ns gives a good match to the measured delays. The RMS value of the distributions gives an estimation of the total timing jitter of the readout system. This includes the jitter of the analogue front-end, the on-chip readout chain as well as the jitter of the trigger signal sent from the FPGA. The RMS is found to be 330 ps, which means that the readout system itself can indeed achieve a sub-nanosecond time resolution.

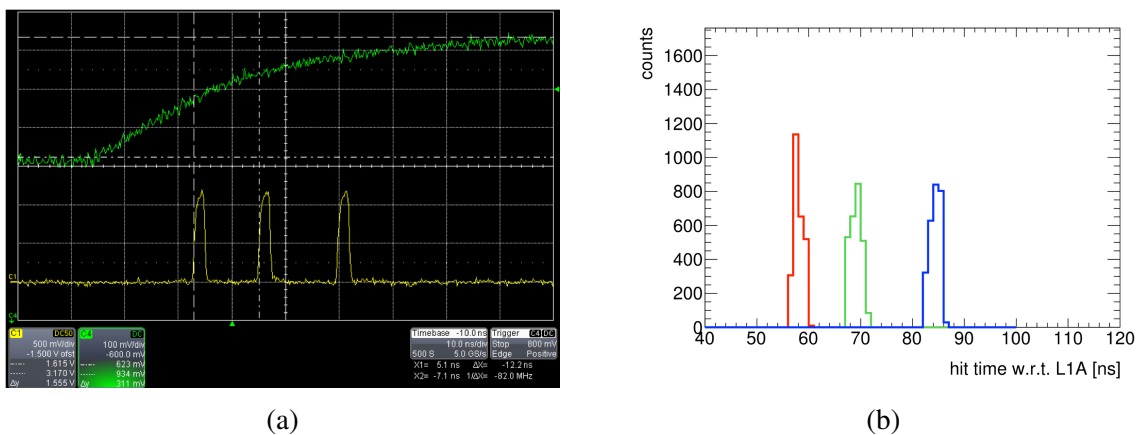


**Figure 3.30:** Output signals after injecting a test pulse to pixels on the top, middle, and bottom of a column: (a) analogue output of a pixel and reference signal seen on the oscilloscope, (b) distribution of the arrival time of reference pulses sampled by the firmware (reproduced from [74]).

To achieve an even higher timing precision in sampling the MALTA signals, another readout system has been developed using the picoTDC time-to-digital converter chip [75]. This chip interfaced with the MALTA can sample 4 out of the 40 LVDS output signals with a binning of 12 ps. Fig. 3.31 shows a measurement performed using this system to obtain the distribution of

the pulse width of the MALTA reference signal in different double columns of the chip. A mean pulse width value of 2.28 ns is obtained with an RMS value of only 30 ps, showing an excellent uniformity of the reference pulses generated in different double columns of the MALTA.

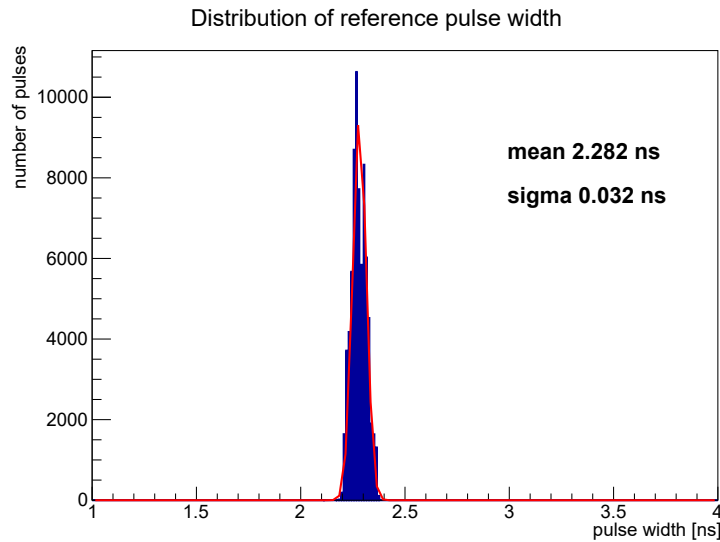


**Figure 3.31:** Pulse width distribution obtained by sampling the MALTA reference signal with the picoTDC chip.

The asynchronous oversampling readout can also be used to check the timing alignment of the pulses on different bits of the MALTA output word. An example of timing distributions of pulses on 36 bits of the output word (the chip ID is not used when testing a single chip) injecting a test pulse to the same pixel 200 times is shown in fig. 3.32. The pulse width is set to 1 ns, but the pulses take up 4 sampling windows because they are stretched slightly by the OR logic at the periphery, which does not have a balanced delay on the rising and falling edge, as well as the delay modules in the FPGA. Nevertheless, the signals on all the outputs when pulsing this particular pixel are aligned to within one sampling window of 390 ps. 200 pulses are detected on all the outputs corresponding to the address of this pixel (the reference line, a pixel address line, all 5 group address lines, the group identifier line and a column address line). As the changing of the BCID counter is uncorrelated with the time when the test pulses are injected, the expected number of pulses on each of the two bits is 100, and the slight difference between the two is well within the statistical variations on this counter value.

The alignment of signals on all bits has been checked systematically by injecting test pulses to multiple pixels within the matrix and repeating the previous measurement. The delay values of all bits with respect to the reference signal are plotted in fig. 3.33. The majority of pixel and group bits arrive an average  $\sim 200$  ps earlier than the reference signal, which is due to the fact that the capacitive load on the reference signal at the periphery is somewhat larger than other bits, since the reference is used by a lot of the peripheral logic and hence connects to a



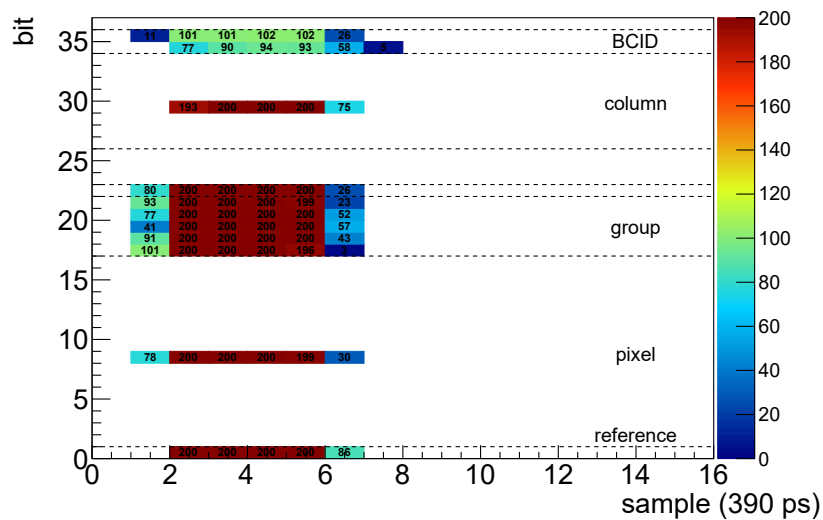


**Figure 3.32:** Timing distribution of 36 bits of the MALTA word after pulsing a single pixel 200 times. The signals are aligned within one sampling window of 390 ps.

large number of gates. The column address and BCID bits are generated at the periphery using the reference signal itself, so they are close to perfectly aligned with the reference. Since the merger logic is disabled, the delay counter bits are not used. One thing to note is that two pixel lines and two group lines have a distribution significantly wider than the other bits, and their delay with respect to the reference signal is as large as  $-600$  ps in some cases. This has been traced back to capacitive coupling between the two pixel lines and the two group lines in the routing structure within the matrix. The group lines are shielded from each other, but are not fully shielded from two of the pixel lines, resulting in a lower effective capacitance and smaller delay when those pixel lines are active at the same time as the group lines. This is the cause of the bimodal distributions on bits 11, 13, 17 and 18 in fig. 3.33. Even though the firmware is still capable of recording these pulses and assigning them to the correct data word, this capacitive coupling will be corrected in future designs by adding a shielding line between the pixel and group lines.

Another interesting timing measurement that can be obtained using the full readout chain is a time walk measurement similar to the one performed using the analogue monitoring pixels, but this time including the delay of the discriminators and the propagation delay of the signals down the column. By measuring the delay of the MALTA output signals with respect to a fast trigger signal (in this case provided by a scintillator), one can obtain the timing distribution of hits coming from the matrix and accurately measure the in-time efficiency (assuming a near-100% overall detection efficiency). Such a timing distribution during a  $^{90}\text{Sr}$  source test with the mean charge threshold set to around  $300 e^-$  is shown in fig. 3.34a. To avoid the influence of small charges shared between pixels, only the leading signals of clusters are included in this



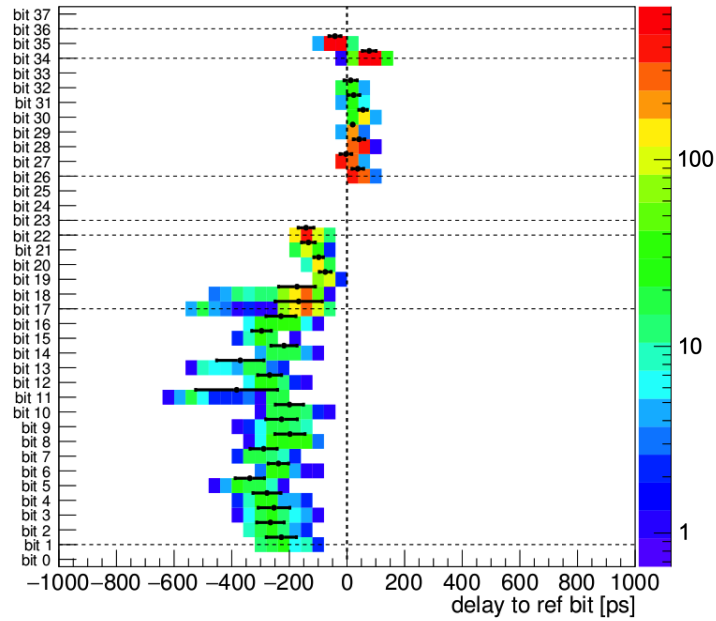


**Figure 3.33:** Timing distribution of the 36 bits scanning pixels from different groups and columns. The bimodal distribution in bits 11, 13, 17 and 18 stems from capacitive coupling between pixel and group lines.

calculation. By checking the fraction of hits within any given 25 ns window and finding the maximum of this fraction, the maximum in-time efficiency of the sensor is obtained. As shown in fig. 3.34b, this number reaches 98% for this threshold setting [72]. Note that this number is reached without any correction for the  $\sim 8$  ns of signal propagation delay down the column. In principle, having measured this propagation delay, one could use the group address to correct for this delay, which would likely result in full in-time efficiency, especially at thresholds even lower than  $300 e^-$ .

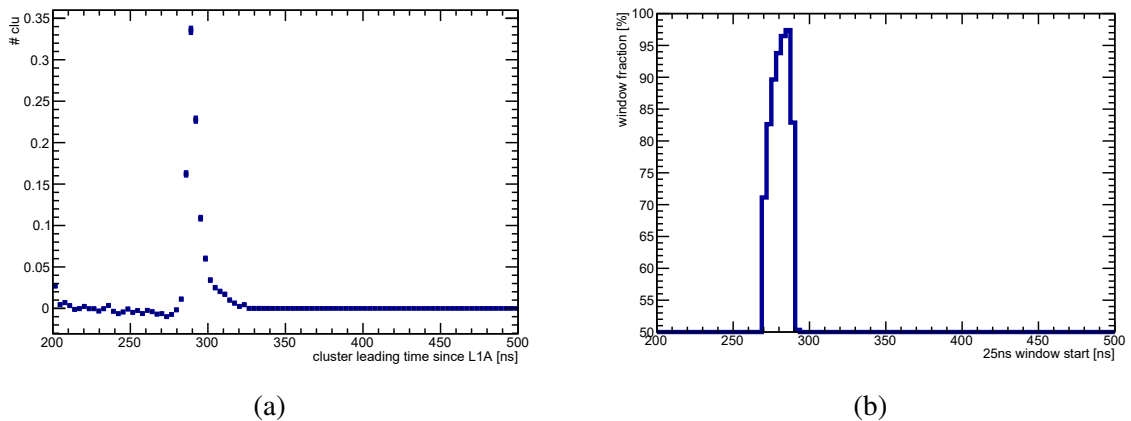


**Figure 3.34:** (a) Timing distribution of hits obtained with respect to a scintillator trigger obtained during a  $^{90}\text{Sr}$  source test with a threshold of  $300 e^-$  and (b) the fraction of hits within a moving 25 ns window (reproduced from [72]).

### 3.4.3 Beam test results

The detection efficiency of the MALTA sensors is measured during a beam test. The test is performed using the 120 GeV pion beam provided by the CERN SPS [76]. The device under test (DUT), i.e. the MALTA chip that is being measured, is placed between three and three planes of reference detectors, in this case MIMOSA-26 sensors which make up a so-called beam telescope [77]. A sketch of this setup is shown in fig. 3.35. The tracks of the particles from the beam are reconstructed from the telescope with a position resolution of  $3\ \mu\text{m}$  for hits on the DUT. The detection efficiency is calculated as the ratio of the number of events with telescope tracks and a corresponding hit on the DUT over the number of all events with a telescope track within a given acquisition window. The telescope and the DUT are aligned in a way that the beam intensity is the highest over a region of the DUT which is of particular interest. For example, fig. 3.36a shows the number of tracks passing through the plane of the DUT during a testbeam run. The DUT covers an area of nearly  $2\times 2\ \text{cm}^2$ , with coordinate (0,0) being the centre of the chip. The beam intensity and therefore the number of tracks is the highest over sectors 2 and 3 for which the detection efficiency was measured during this test. Fig. 3.36b shows the overall detection efficiency obtained during this run. The threshold of the MALTA chip was set to a value of around  $250\ e^-$ , the lowest which still allowed operation with noise levels that would not significantly affect the readout and data acquisition. The bias voltage of the p-wells was set to the lowest possible  $-6\ \text{V}$ , while the substrate voltage was set to  $-15\ \text{V}$  in this test. Note that three quarters of the chip have been masked either using the in-pixel masking circuitry or in the offline data analysis to reduce the amount of noise hits and data to be collected. It can be seen that the overall efficiency over the unmasked region of the chip is close to 100% and relatively uniform over the two sectors.

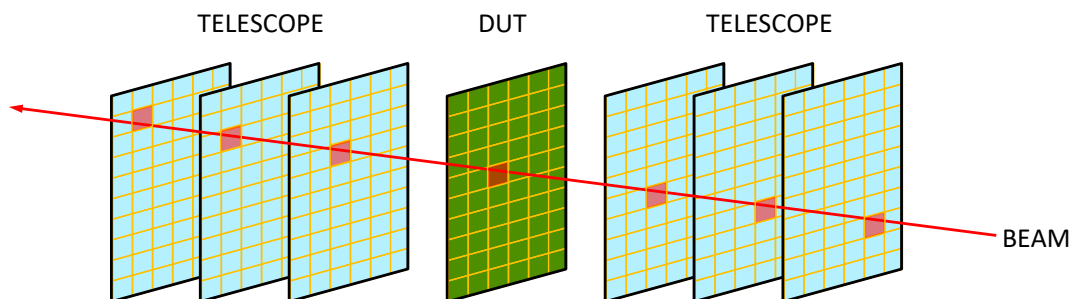


**Figure 3.35:** A sketch of the testbeam setup used to measure the detection efficiency of MALTA chips.

Since the telescope provides a track resolution of  $3\ \mu\text{m}$ , the detection efficiency can be analysed with sub-pixel precision to check whether a uniform high efficiency can be achieved over the full area of a pixel. The in-pixel efficiency obtained this way for  $2\times 2$  pixel groups of sector 2 with several threshold settings is plotted in fig. 3.37. This sector contains a collection

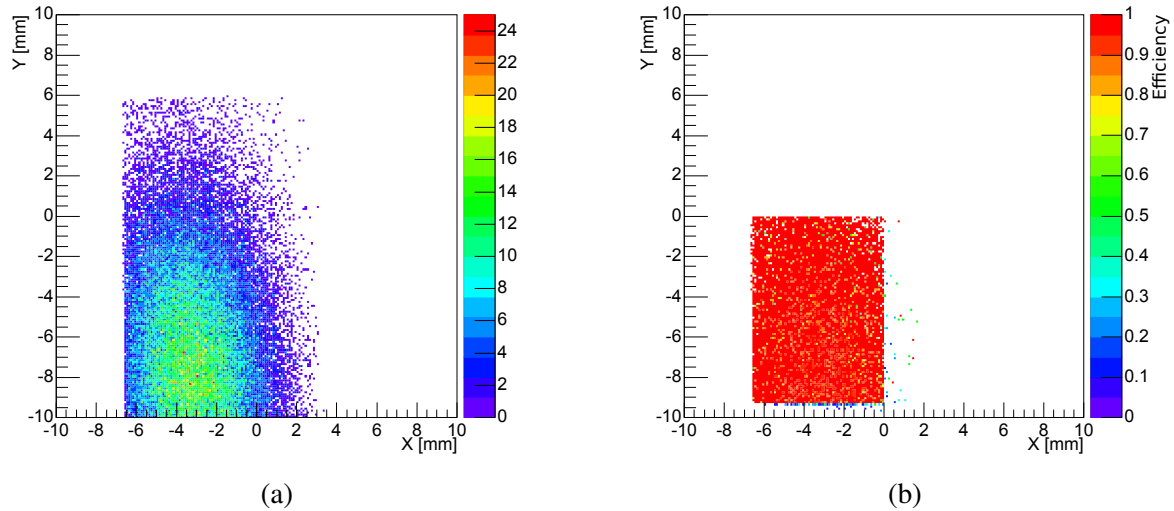


**Figure 3.36:** (a) Number of tracks and (b) overall efficiency during a testbeam run for an unirradiated MALTA chip. A region of interest has been defined over sectors 2 and 3.

electrode with a diameter of  $3\ \mu\text{m}$ , a diode reset and a "maximum" deep p-well layout. For a threshold setting of around  $450\ e^-$ , an efficiency of around 98% is obtained in the centre of the pixels, close to the collection electrode. However, a slight efficiency loss is observed in the corners of the pixels, where charge is shared between the four pixels. The charge deposited by the particle is split more or less equally between the pixels, and for this relatively high threshold the collected charge is not always enough to flip the discriminator of the front-end. This is the reason why the average efficiency at this threshold is below 95%. By adjusting the front-end setting for a lower threshold of around  $350\ e^-$ , the efficiency loss in the pixel corners becomes far less prominent, resulting in an overall efficiency of above 97%, which is close to uniform over the pixel area, as seen in fig. 3.37b.

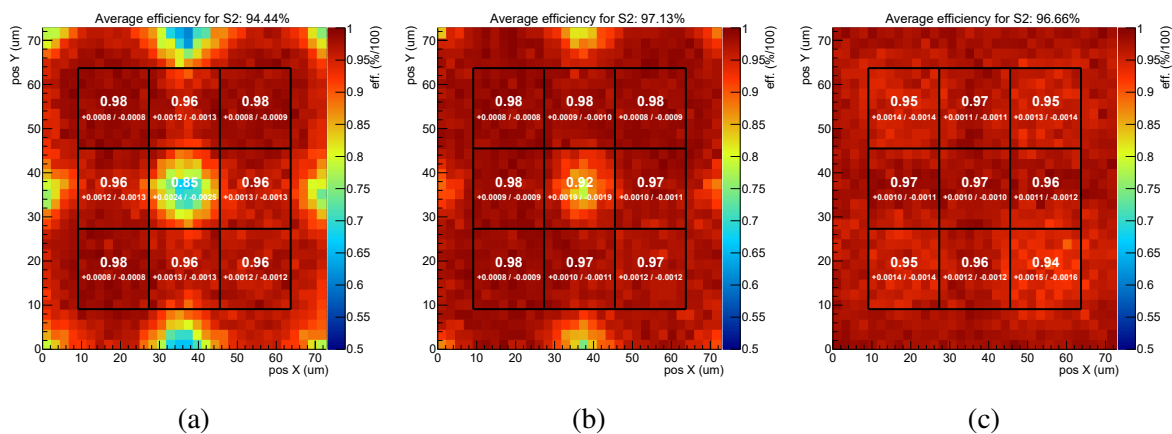


**Figure 3.37:** In-pixel efficiency for  $2 \times 2$  pixel groups at different thresholds: (a) threshold of  $450\ e^-$ , (b) threshold of  $350\ e^-$ , (c) threshold of  $250\ e^-$ .

By going even lower with the threshold, down to about  $250\ e^-$ , the inefficiency in the corner regions disappears completely, but in fig. 3.37c the efficiency in the centre of the pixel decreases

by 2-3%. The reason for this is that, due to the inability to mask noisy pixels over some regions of the matrix, the noise hit rates at this threshold become significant. Since the merger logic is disabled and the matrix is read out using the OR logic at the chip periphery, if two reference pulses arrive at the periphery at the same time, the merging of the group and column address pulses will result in the wrong address information. Even for the highest particle hit rates during the beam test, this occurs very rarely, and the efficiency loss due to this effect is negligible. However, with high noise levels on the chip, this "merging" between pulses containing the actual hit information from a particle with pulses caused by noise hits can lead to a loss of address information from the particle hits and hence the  $\sim 1\%$  efficiency loss in fig. 3.37c. Of course, in future designs, a fully functional merger logic at the periphery would prevent the possibility for this to happen. Apart from that, with a fully functional masking procedure and lower levels of RTS noise, one will be able to contain the noise rates to levels where this phenomenon practically never occurs even with the backup readout option using the OR logic.

As mentioned, the results shown were obtained with a p-well bias voltage of  $-6$  V and a substrate bias voltage of  $-15$  V. These values proved to be a good working point to obtain the highest possible detection efficiency. A high absolute value of the p-well voltage helps to deplete the n- region around the electrode and reduce the electrode capacitance, while a somewhat higher substrate voltage enhances the vertical electric field and hence the speed of the charge collection. The efficiency was found to be close to uniform over sectors 0-3, with no significant difference observed between the two sizes of the collection electrode ( $2\ \mu\text{m}$  or  $3\ \mu\text{m}$  diameter). A slight difference of up to 2% in detection efficiency was found between the two different deep p-well geometries ("medium" or "maximum"), where the "maximum" deep p-well layout shows a higher efficiency due to a somewhat lower threshold, as seen in the threshold scans in fig. 3.27. In most measurements, sectors 4-7, which use a PMOS reset as opposed to a diode, were disabled to reduce the noise hit rates, since the threshold of these sectors is in any case slightly higher and no further improvement in efficiency is expected.

## **3.5 Performance of irradiated sensors**

### **3.5.1 Sensor and front-end after irradiation**

A number of MALTA chips have been irradiated with neutrons up to  $10^{15}$   $n_{\text{eq}}/\text{cm}^2$  of NIEL fluence at the TRIGA reactor in Ljubljana [78]. The chips also received up to 1 Mrad of TID coming from the  $\gamma$  background radiation at the facility. During irradiation, the chips were not powered. After irradiation, the chips are kept at a low temperature (below  $-20^\circ\text{C}$ ) to avoid annealing of the radiation damage. All the measurements are also performed at temperatures of  $-20^\circ\text{C}$  or below, since the sensor leakage current values at room temperature cause a significant

increase in noise, as discussed in sect. 3.2.3. The I-V curves of the sensor showing the p-well and substrate currents for different p-well and substrate voltages at room temperature are seen in fig. 3.38. The value of the substrate leakage current at low substrate voltages, before punchthrough, increases by over two orders of magnitude compared to unirradiated samples, from a few  $\mu\text{A}$  to about  $500 \mu\text{A}$ . The p-well current is also increased, but not so dramatically, since this also includes surface leakage currents near the Si-SiO<sub>2</sub> interface. After cooling down to  $-30^\circ\text{C}$ , the *SUB* current is reduced to values of a few microamps, which means that after cooling the irradiated chips can be operated in similar conditions to the unirradiated ones. It is also noticeable that the onset of punchthrough occurs at somewhat lower *SUB* voltages, but that the current increase is much slower than for unirradiated sensors, which can be explained by the changes in the doping concentrations in the sensor after irradiation, possibly even type inversion of the p- epitaxial layer, as explained in sect. 2.2.

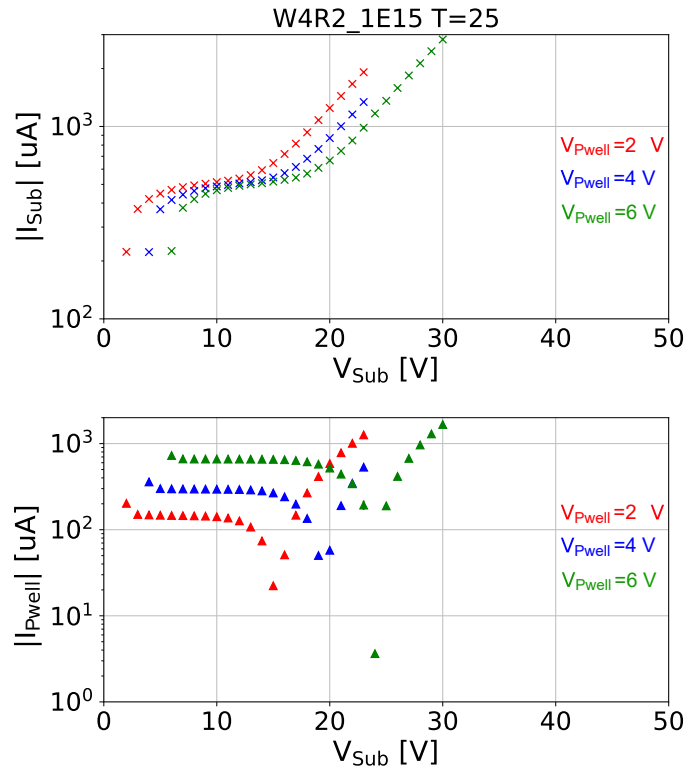


**Figure 3.38:** Sensor leakage current after neutron irradiation to  $10^{15} \text{ n}_{\text{eq}}/\text{cm}^2$ , measured at room temperature on the *SUB* and *PWELL* nodes with varying *SUB* voltage.

To compare the sensor and front-end performance of unirradiated and irradiated chips, an  $^{55}\text{Fe}$  source spectrum is collected from the diode reset analogue monitoring pixels of each sample at  $-30^\circ\text{C}$ , with the same front-end bias settings. The results are shown in fig. 3.39. The sensor and front-end are fully functional after irradiation to  $10^{15} \text{ n}_{\text{eq}}/\text{cm}^2$ , and the amplitude of the K- $\alpha$  peak is even shifted to higher values, going from 433 mV for the unirradiated sample

to about 478 mV for the irradiated one. The cause of this factor of 1.1 increase in signal is later revealed to be the decrease in the collection electrode capacitance after the changes in effective doping due to irradiation. This automatically results in a higher voltage signal for the same collected charge at the input of the front-end amplifier, which in turn results in a higher signal at the amplifier output, since the front-end gain does not degrade significantly with neutron irradiation nor after 1 Mrad of TID. The RMS of the K- $\alpha$  peak, which gives an estimate of the noise levels, shows quite a significant increase, and the  $\mu/\sigma$  is nearly a factor of 2 larger than for unirradiated sensors at room temperature (fig. 3.25) and nearly a factor of 3 larger than the unirradiated sample at low temperature in fig. 3.39. This can in part be attributed to the increase in sensor leakage current, but also to a noise increase in the front-end after 1 Mrad of TID.

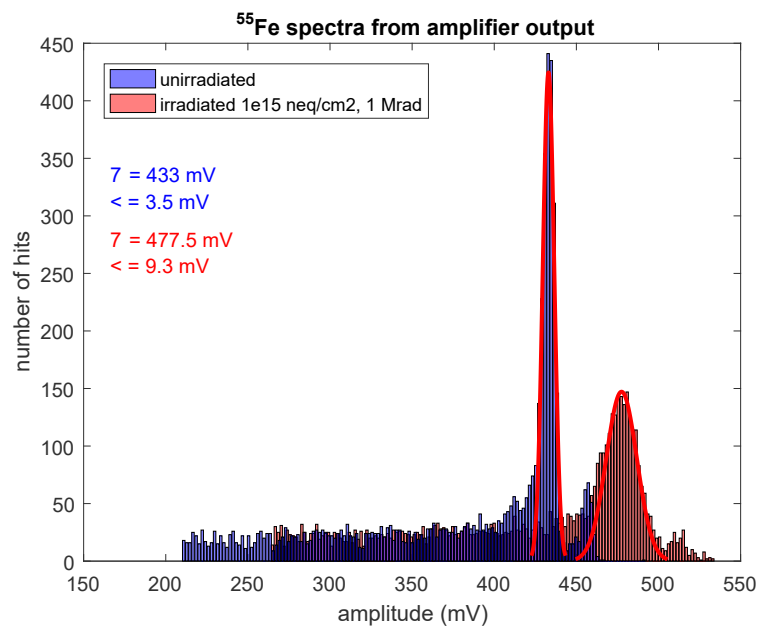


**Figure 3.39:**  $^{55}\text{Fe}$  source spectra obtained from the monitored analogue outputs of front-ends with diode reset before and after neutron irradiation to  $10^{15} \text{ n}_{\text{eq}}/\text{cm}^2$ .

Threshold scans have been performed on MALTA chips irradiated with neutrons to  $5 \times 10^{14} \text{ n}_{\text{eq}}/\text{cm}^2$ . The high  $I_{DB}$  setting used in this measurement, corresponding to the maximum DAC code of 127, is the reason for the high mean threshold value of around  $500 \text{ e}^-$  in fig. 3.40a. The difference in threshold between the two sectors almost disappears after irradiation, indicating that the electrode capacitance is now less affected by the deep p-well geometry around it. The increase in the mean value of noise in fig. 3.40b from  $8 \text{ e}^-$  for unirradiated devices to  $12 \text{ e}^-$  after neutron irradiation is expected from the  $^{55}\text{Fe}$  spectra. However, apart from the mean value of the noise, the RTS tail in the distribution also becomes more prominent, meaning that an even larger number of noisy pixels will appear when working at low thresholds. Furthermore, the threshold variation given by the RMS value of the threshold distributions increases by a factor of 2 compared to unirradiated devices and is around  $70 \text{ e}^-$ , which limits the operating threshold

of irradiated chips even more. This type of increase in variation after uniform irradiation is unexpected, and the exact reasons for it are still under investigation. Nevertheless, based on these numbers, the decision has been made to include a per-pixel threshold adjustment in future designs to achieve a better threshold uniformity and hence a lower minimal operating threshold.

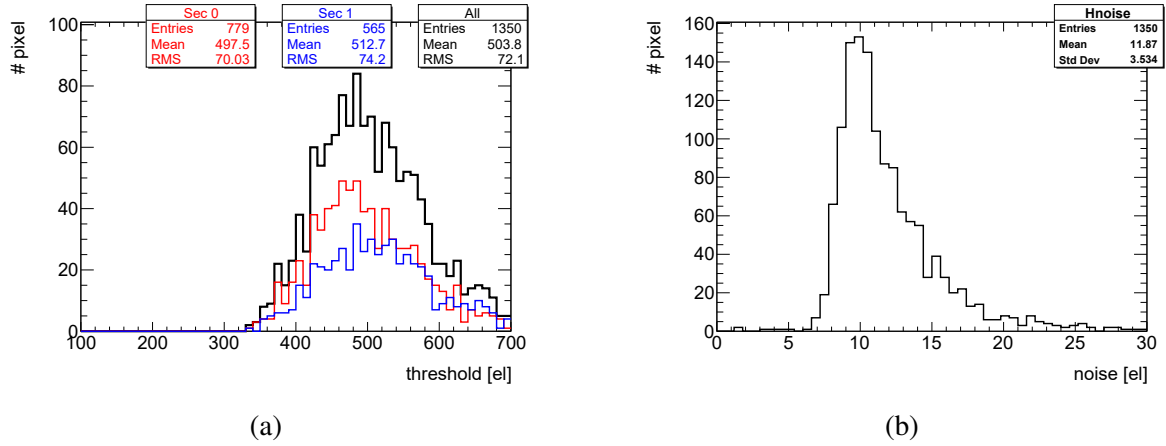


**Figure 3.40:** (a) Threshold and (b) noise distributions on a chip irradiated with neutrons to  $5 \times 10^{14} \text{ n}_{\text{eq}}/\text{cm}^2$ .

MALTA chips have also been irradiated with x-rays up to 70 Mrad. Since x-rays do not cause displacement damage, this type of irradiation will mostly affect the front-end electronics. Since the effects of TID damage also depend on the biases of the transistors in the front-end, the chip was powered during irradiation, though not all the bias settings for the front-end were at their nominal value, because the hit activity during irradiation would have been too high. After reaching 70 Mrad, the irradiation is stopped and threshold scans are performed with the nominal front-end settings and an  $I_{DB}$  value equal to the maximum DAC code. The results are shown in fig. 3.41. Since the sensor is not affected, the threshold difference between the two sectors remains, and the increase in threshold variation compared to unirradiated devices is still significant, though not as alarming as after neutron irradiation. The increase in noise, however,

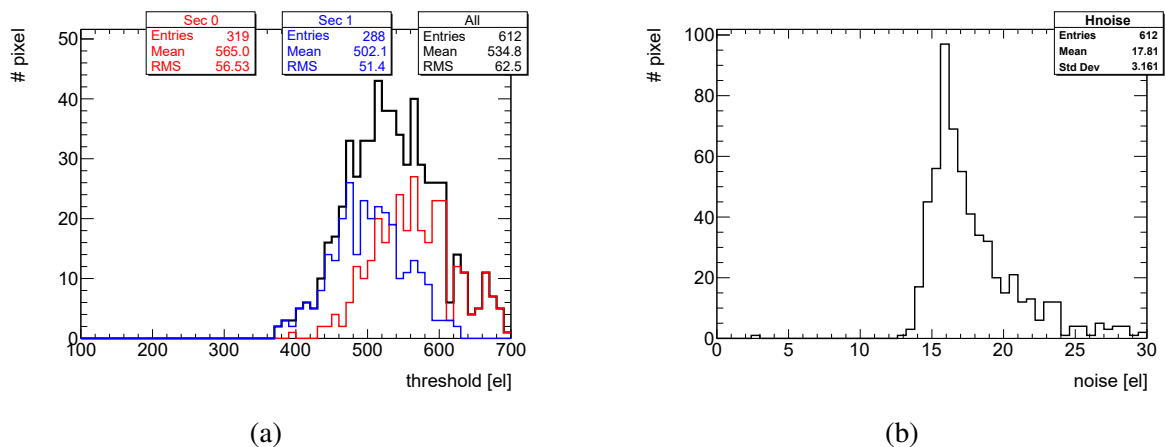


**Figure 3.41:** (a) Threshold and (b) noise distributions on a chip irradiated with x-rays to 70 Mrad.

is more prominent than after neutron irradiation, with a mean noise value close to  $18\text{ e}^-$  and still a noticeable RTS tail. Again, the net result of the higher threshold dispersion and noise is a higher minimal operating threshold, which could cause a lower detection efficiency.

### 3.5.2 Efficiency in beam tests

The detection efficiency of MALTA sensors irradiated with neutrons to  $10^{15}\text{ n}_{\text{eq}}/\text{cm}^2$  has also been characterised in beam tests with the 120 GeV pion beam of the CERN SPS. The measurement setup is the same as for unirradiated chips in fig. 3.35, with the addition that the DUT is placed inside a cooling box and kept at temperatures below  $-20^\circ\text{C}$  to avoid annealing and reduce the sensor leakage current. The beam is once again centred over sectors 2 and 3 to compare the performance of the two different deep p-well geometries. The in-pixel efficiency plots for  $2\times 2$  pixel groups in sector 3 at different threshold settings are shown in fig. 3.42. From fig. 3.42a, which shows the efficiency for a threshold of around  $320\text{ e}^-$ , it is immediately noticeable that the sensor suffers from a significantly degraded efficiency in the pixel corners after irradiation. While the efficiency in the pixel centre is 96%, basically equal to the number for unirradiated sensors, the efficiency in the corner between four pixels drops to an average number of 43%, resulting in an overall efficiency of only 73.3%. By decreasing the threshold, the inefficient regions in the corners decrease as well, and the overall efficiency goes up to 77.5%. However, for the lowest achieved threshold of about  $230\text{ e}^-$ , the efficiency loss due to merging of particle hits with noise hits at the chip periphery becomes significant. This is evidenced by the decrease in efficiency of a few percent in the pixel centres. The corner efficiency still improves by lowering the threshold, but the average efficiency over the full pixel area plateaus at around 78% because of this hit merging effect.

The fact that the shape of the efficient region around the octagonal collection electrode is not symmetrical on all sides points to an influence of the deep p-well coverage on the detection efficiency. In sector 3, the deep p-well was removed asymmetrically around the collection electrodes in areas where no PMOS transistors are used for the front-end and readout electronics. The shape of the efficient regions correlates well with the areas of removed deep p-well. This becomes painfully obvious when comparing the in-pixel efficiency for sectors with the two deep p-well layouts. This is depicted in fig. 3.43. In sector 2, where the deep p-well, the yellow layer in fig. 3.43c, surrounds the purple n-well electrode symmetrically on all sides, the region of high efficiency is also symmetrical around the electrodes. Moreover, the efficiency loss in the pixel corners is much more pronounced than for sector 3, and the average efficiency peaks at only 66.3%. On the other hand, the high efficiency regions in sector 3 are significantly larger, and the highest efficiency of 80% for one quarter of a pixel corresponds to the areas with the largest portion of the removed deep p-well.



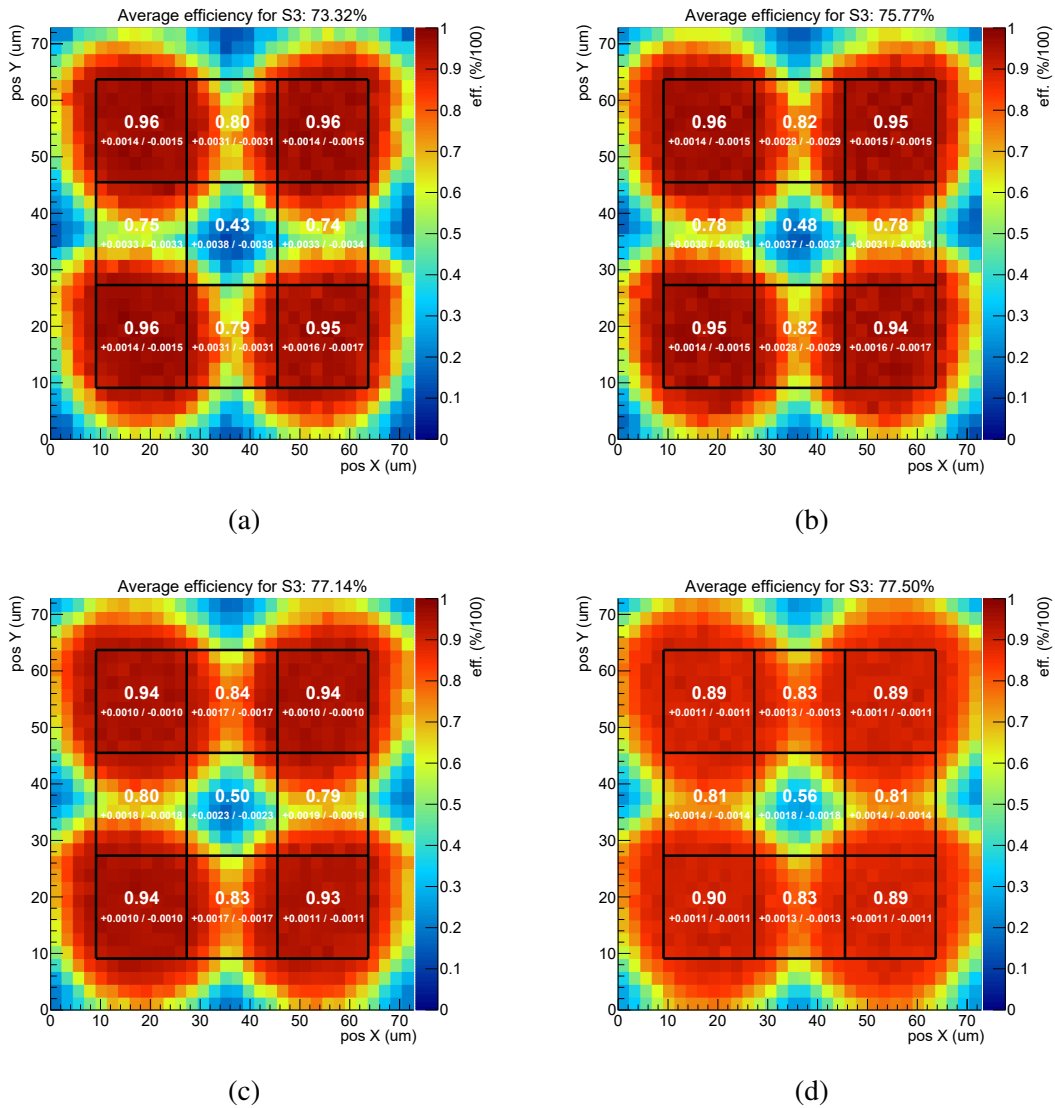


**Figure 3.42:** In-pixel efficiency in sector 3 after  $10^{15} \text{ n}_{\text{eq}}/\text{cm}^2$  at different thresholds: (a)  $320 \text{ e}^-$ , (b)  $280 \text{ e}^-$ , (c)  $250 \text{ e}^-$ , (d)  $230 \text{ e}^-$ .

All these measurements point to the fact that the loss in detection efficiency in the pixel corners after irradiation is caused by the lack of lateral electric field which would "push" the charge towards the collection electrode. Therefore, charge deposited by particles near the pixel corners is more likely to be trapped by radiation-induced defects, resulting in the particles not being detected. Indeed, the planar junction introduced by the process modification using the n- implant ensures full depletion of the sensitive layer and a strong vertical electric field, but introduces a lateral field minimum near the pixel edges. Removing the deep p-well in larger areas around the electrode helps to create a lateral potential gradient and "funnel" the charge towards the electrode. The lateral electric field near the pixel edges is very sensitive to changes in pixel size, with smaller pixels being less affected by the problem of a field minimum near the edges. This, in combination with the fact that the testbeam data on the Investigator test-chip was taken at a very low threshold which can not be achieved in the large MALTA matrix, explains

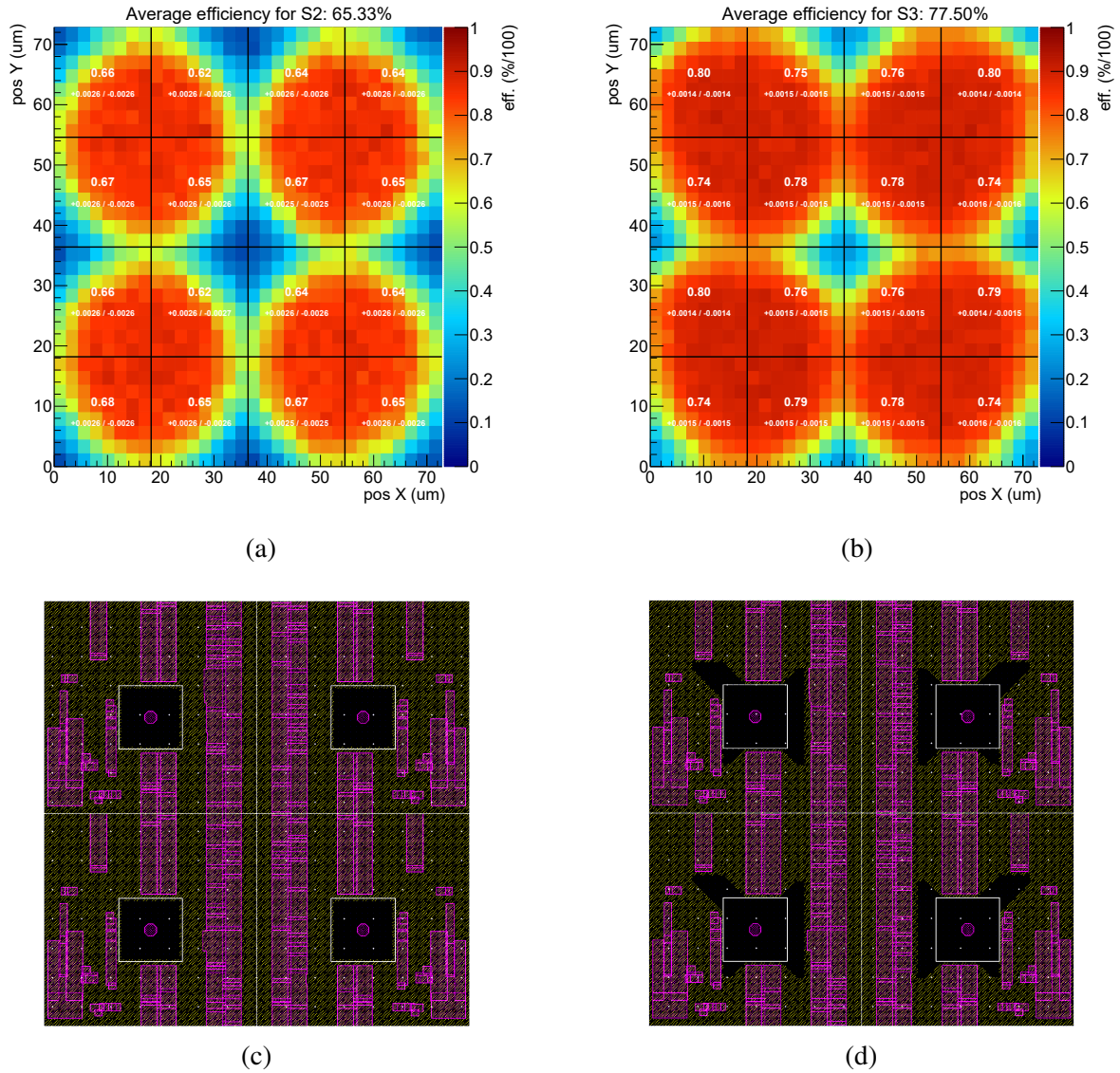


**Figure 3.43:** Correlation between in-pixel efficiency after  $10^{15}$   $n_{eq}/cm^2$  and deep p-well coverage within the pixel. (a) and (b) show the efficiency measured in different sectors, while (c) and (d) show the layout of the n-wells and deep p-well in the respective sectors.

the fact why no efficiency loss was observed after irradiation in the  $25 \times 25 \mu m^2$  pixels of the Investigator, as opposed to the  $36.4 \times 36.4 \mu m^2$  pixels of the MALTA.

The above efficiency measurements were taken at a p-well bias of  $-6$  V and a substrate bias of  $-15$  V. An absolute substrate bias higher than 6 V enhances the vertical electric field and helps with the charge collection, especially for charge deposited near the pixel centres. The efficiency is fairly uniform in the range of substrate voltages between  $-9$  V and  $-15$  V. However, for higher absolute values of substrate voltage, up to around  $-25$  V when punchthrough sets in, the efficiency decreases by several percent. This is due to the fact that the vertical electric field becomes so strong that an even larger fraction of the charge deposited near the pixel borders is pushed into the potential well where it gets trapped. In other words, the increase in the ratio of vertical over lateral field results in an even lower efficiency near the pixel borders.

Another measurement which demonstrates the causes of the efficiency loss between unirradiated and irradiated sensors is the measurement of the average cluster size within the pixel. For each particle track, the number of pixel hits on the DUT, i.e. the cluster size produced by that track is calculated. The position dependence of this number within the  $2 \times 2$  pixel group is shown for an unirradiated and a  $10^{15} \text{ n}_{\text{eq}}/\text{cm}^2$  irradiated chip with similar low thresholds in fig. 3.44. Before irradiation, the cluster size for particles passing close to the collection electrode is close to 1, the cluster size near the border between two pixels is close to 2, and it gets even larger for hits in the corner between four pixels. This means that the particles are detected even if the charge they deposit is shared by 3-4 pixels. This is reflected in the average cluster size over the full pixel, which is calculated to be 1.53. In stark contrast, the average cluster size after irradiation is only 1.06. The cluster size near the pixel borders barely changes compared to the cluster size in the middle of the pixels, which means that most of the hits with cluster size 2 and almost all hits with cluster size 3 and 4 are lost. This once again confirms that the efficiency loss is the result of the trapping of charge shared between multiple pixels, and that the collected charge in these cases is not enough to exceed the threshold.

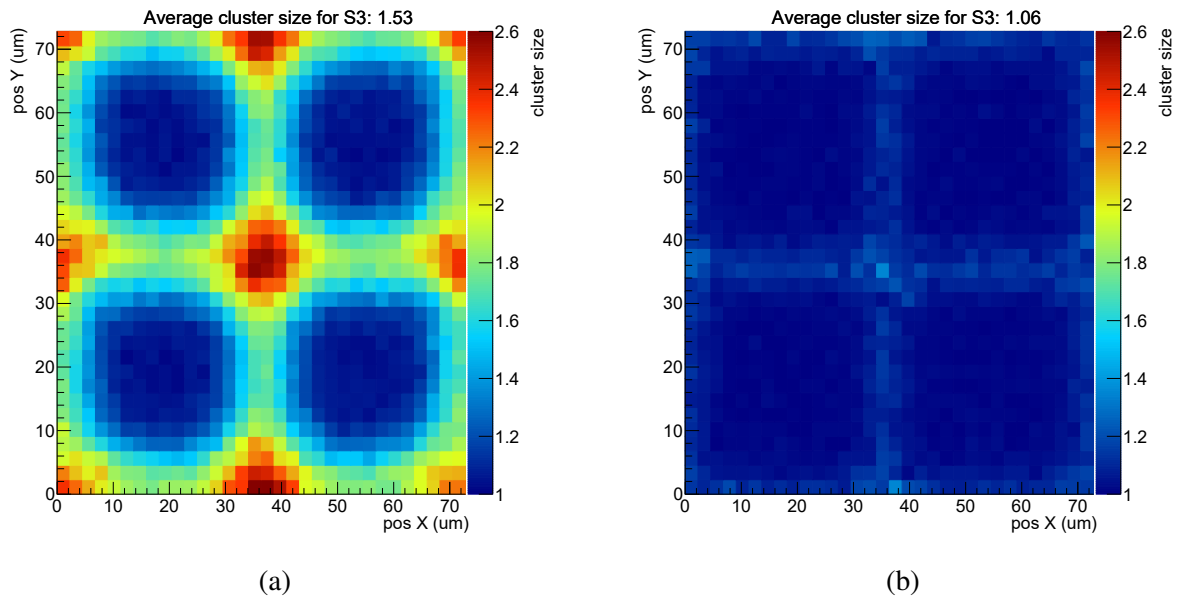


**Figure 3.44:** In-pixel cluster size in sector 3 (a) before and (b) after irradiation to  $10^{15} \text{ n}_{\text{eq}}/\text{cm}^2$ . The reduction in cluster size near the pixel edges is caused by the loss in detection efficiency.

In conclusion, the measurement results presented show that the designed sensor, front-end and readout architecture are fully functional and show a good performance in terms of timing and detection efficiency before irradiation. However, due to higher operating thresholds caused by RTS noise and a larger than expected threshold dispersion of the front-end circuit, in combination with degraded charge collection after irradiation due to the lack of lateral electric field near the pixel edges, the efficiency after  $10^{15} \text{ n}_{\text{eq}}/\text{cm}^2$  is below 80%. The issues leading to this efficiency loss will be addressed in future designs, as discussed in the next chapter.

# Chapter 4

## Optimisation of pixel matrix and readout electronics

### 4.1 Process improvements for radiation hardness

To improve the detection efficiency in the pixel corners after irradiation, two new process changes have been developed to increase the lateral electric field at the pixel borders. The idea is to introduce a junction along the sensor depth near the edge of the pixel, which would enhance the lateral component of the electric field. This can be achieved by introducing an additional extra-deep p-well implant near the pixels edges or by creating a gap in the n-implant. The cross-sections of a pixel as well as a top view of the layout of  $2 \times 2$  pixels for both solutions are shown in fig. 4.1 and fig. 4.2, respectively. Apart from significantly increasing the lateral field, both modifications shift the minimum of the electric field deeper into the silicon compared to the original modified process. As a result, the electric field already starts to bend towards the collection electrodes deeper within the silicon, reducing the drift path and hence the charge collection time [79].

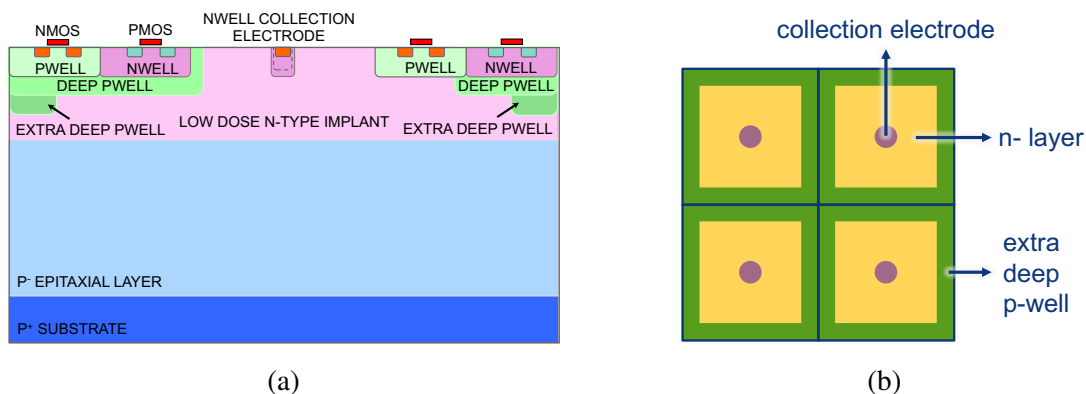


**Figure 4.1:** Process modification with an additional extra-deep p-well near the pixel edges: (a) cross-section of a pixel, (b) top view of the modified layers in  $2 \times 2$  pixels.

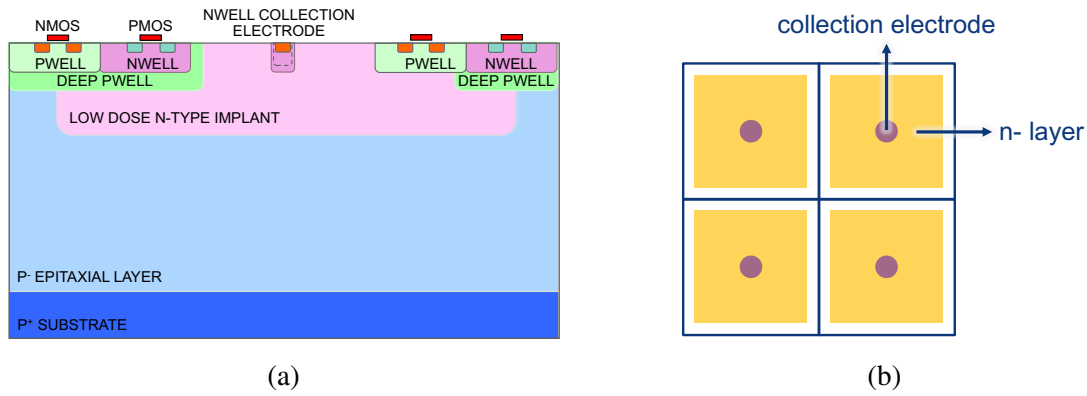


**Figure 4.2:** Process modification with a gap in the n– layer near the pixel edges: (a) cross-section of a pixel, (b) top view of the modified layers in  $2 \times 2$  pixels.

Transient three-dimensional TCAD simulations have been performed for both modifications to assess the improvements in charge collection time and collected charge after irradiation. The traversal of a minimum ionising particle (MIP) is simulated at the corner of the  $36.4 \times 36.4 \mu\text{m}^2$  pixel, which is the worst case in terms of charge collection. To model the effects of radiation damage, defect levels are introduced in the silicon bulk according to [80]. The voltage on the collection electrode is set to 0.8 V, which is around the voltage needed for the correct operation of the first stage of the front-end amplifier, while the p-wells and the substrate are biased at  $-6$  V. The transient evolution of the electrode current for the two new modifications and the original modified process is shown in fig. 4.3a. Both proposed modifications provide a reduction in charge collection time by at least a factor of two. By integrating the electrode current over time one obtains the total collected charge. For the original modified process, a large fraction of the

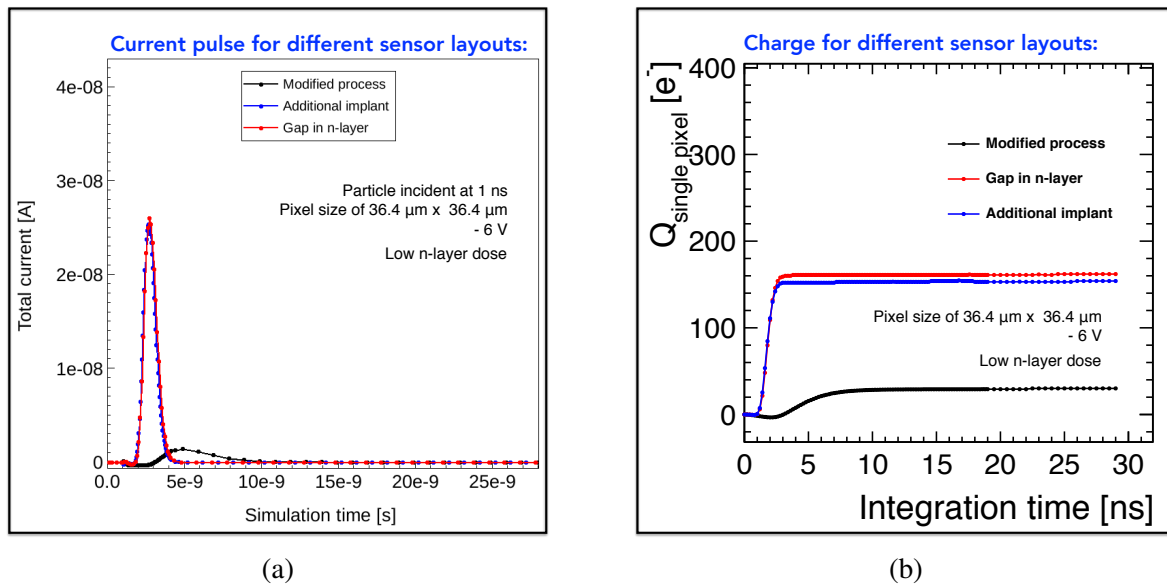


**Figure 4.3:** TCAD simulations for (a) electrode current and (b) charge collected for a MIP incident at the pixel corner after irradiation with different sensor layouts. Both new concepts show an improved charge collection time and higher collected charge [79].

charge, which is above  $300 e^-$  before irradiation, is lost due to the trapping of charge carriers in the low-field regions. For the new modifications, a fraction of the charge is still lost, but the total collected charge is at least a factor of three higher than with the original modified process. Using these simulations, the optimal width of the additional extra-deep p-well in the case of the first modification (the green area in fig. 4.1b) for a pixel pitch of  $36.4 \mu\text{m}$  is found to be  $2.5 \mu\text{m}$  for each pixel. Conversely, the optimal width of the gap in the n- implant in the case of the second modification (the white area near the pixel borders in fig. 4.2b) is found to be  $2 \mu\text{m}$  per pixel.

Note that both improvements reduce the potential barrier between the p-wells and the substrate provided by the n- layer. As a result, punchthrough will occur at lower substrate voltages than in the original modified process. With a p-well voltage of  $-6 \text{ V}$ , for the gap in the n- implant the simulated substrate voltage at which punchthrough starts to occur is only around  $-8 \text{ V}$ , while for the additional extra-deep p-well this value is simulated to be around  $-10 \text{ V}$ . However, as evidenced by the MALTA efficiency measurements, increasing the substrate voltage beyond those values does not result in better charge collection, so the optimal substrate voltage for the new modifications is in any case in the range achievable before the onset of punchthrough. Also note that both improvements require only a minimal change in the manufacturing process. In the case of the gap in the n- layer, only a mask change for the n- implant is required, while for the additional extra-deep p-well, one additional mask is required, but this implant is already available in the foundry, so no process development is needed.

## 4.2 Pixel matrix design changes

The new process modifications have been included in a small-scale redesign of the MALTA pixel matrix, which is part of a new test-chip called miniMALTA. The new matrix is 16 (columns) by 64 (rows) large, and contains only the "medium" deep p-well variation of the sensor layout, which has proven beneficial for the charge collection. Horizontally, it is divided into four sectors: one with PMOS reset and the original modified process and three with diode reset and the three process variations: original modified process, additional extra-deep p-well and gap in the n- layer. Vertically, it is divided into two sectors with different front-end designs. The left side contains a front-end modified by enlarging two front-end transistors, most importantly M3, in order to reduce RTS noise. The  $W/L$  ratio of M3 has been increased from  $1/0.18 \mu\text{m}$  to  $1.22/0.38 \mu\text{m}$ , which was a simple layout change increasing the area of said transistor by more than a factor of two. The change also provides a decrease in the output conductance of M3 and an increase in front-end gain, which is simulated to be around 30% higher, with only a slight penalty on the transconductance of M3 and the capacitance on  $OUT_A$ . The size of the clipping transistor M4 has also been increased for better control of the clipping threshold. The right



side of the matrix contains the original MALTA front-end for comparison. In terms of readout architecture, the matrix is the same as the MALTA design: only the four groups of  $2 \times 8$  pixels with the highest group addresses of both "colours" have been included, resulting in the 64 row height.

The layout of the full miniMALTA chip is shown in fig. 4.4. Apart from the changes in the pixel matrix, miniMALTA contains several new features at the chip periphery. A new readout logic is included at the end-of-column to synchronise the asynchronous signals coming from the matrix. After synchronisation, the hit data is read out synchronously with a clock frequency of up to 640 MHz. This is done to simplify the design of the digital periphery after problems with the asynchronous merger logic, but also to enhance compatibility with the off-chip readout systems typically used in the experiments, while maintaining a low digital power consumption in the matrix. A new design of the configuring logic (labelled "slow control"), which was not working reliably in MALTA, has also been included. The DACs have been modified to use 8 bits and to be more modular and independent of the matrix size (the previous design implemented in MALTA was a single block occupying the full width of 512 pixels). Finally, the data transmission unit (DTU) used in the ALPIDE chip was added to send the serialised hit data off-chip using a single LVDS output transmitting the data at 1.2 Gb/s with double data rate (DDR). The 600 MHz needed for this transmission is also generated inside the DTU using a phase-locked loop (PLL).

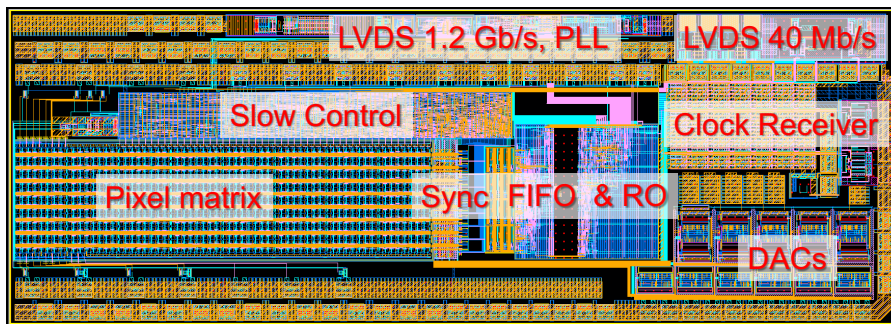


Figure 4.4: Layout of the  $5 \times 1.7 \text{ mm}^2$  miniMALTA chip.

## 4.3 Synchronisation at the end-of-column

### 4.3.1 Random-access memory for synchronisation

The basic idea of the synchronisation circuitry at the end-of-column is to use the reference signal to store the asynchronous pixel and group address signals into a random-access memory (RAM). Since the pulses on the address lines are aligned in time with the reference signal, the latter can be used to enable the writing into the RAM cells, resulting in a logic one being written

if there is a pulse on a certain address line or a logic zero being written in the absence of a pulse. Each of the two 22-bit buses in a double column (one for the "blue" groups and one for the "red" groups) are connected to their own synchronisation block, so the total number of these blocks is two per double column. Apart from the pixel and group address data, the reference signal also stores a timestamp by storing the values of two counters: a 3-bit BCID counter running at 40 MHz and a 4-bit fine time counter running at 640 MHz. This means that the time of arrival of the pulses from the matrix can be recorded with a precision of one 640 MHz clock cycle, which is around 1.5 ns. As already mentioned, this can be useful to obtain some information about the charge collected by pixels in a cluster. In the case of multiple consecutive pulses on one reference line, up to four data words can be stored in four rows of the RAM memory. Hence, each synchronisation block contains  $28 \times 4$  RAM cells, as visualised in fig. 4.5.

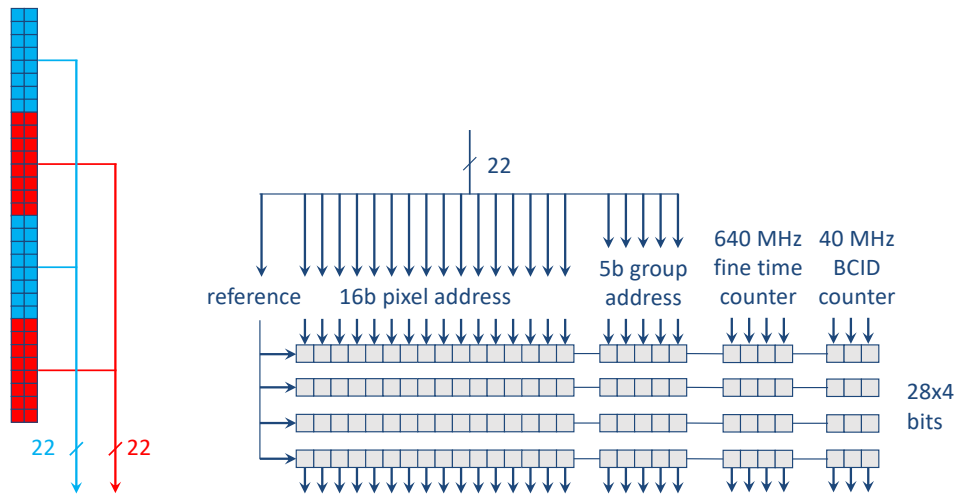


**Figure 4.5:** Working principle of the synchronisation memory in miniMALTA. The 22 address bits and additional timestamps are stored in a  $28 \times 4$  RAM memory.

The basic building block of the RAM memories is the standard dual-port RAM cell with 8 transistors depicted in fig. 4.6. This cell consists of two cross-coupled inverters (transistors M0-M4) and two sets of two NMOS pass transistors used for writing and reading. The writing is done using M4 and M6, which force the the values of  $DATA_{IN}$  and its complement  $DATA_{INB}$  to be stored at the outputs of the two inverters in feedback when the reference signal  $REF$  is active. The memory cell is read out when a read signal is applied to the gates of M5 and M7, forcing the value of  $DATA_{OUT}$  to the value of  $DATA_{IN}$  previously stored. Note that because only NMOS pass transistors are used to save space, the signals will not achieve a full swing of 1.8 V on  $DATA_{OUT}$ , but will go up to  $\sim 1.2$  V determined by the threshold voltage of the NMOS devices. However, the quick transition between 0 and 1.2 V because of the small size of the memory and low capacitance of the data lines allows a simple inverter on the complementary data output  $DATA_{OUTB}$  to be used to restore the full-swing data signal on  $OUT$ . Therefore, when the  $READ$



signal is active, the previously stored  $DATA_{IN}$  will be asserted to the  $OUT$  node of the memory cell. The  $DATA_{IN}$  and  $DATA_{OUT}$  lines are in common for the four rows of the RAM memory, but the use of a dual-port cell enables the simultaneous writing and reading of different rows within the memory.

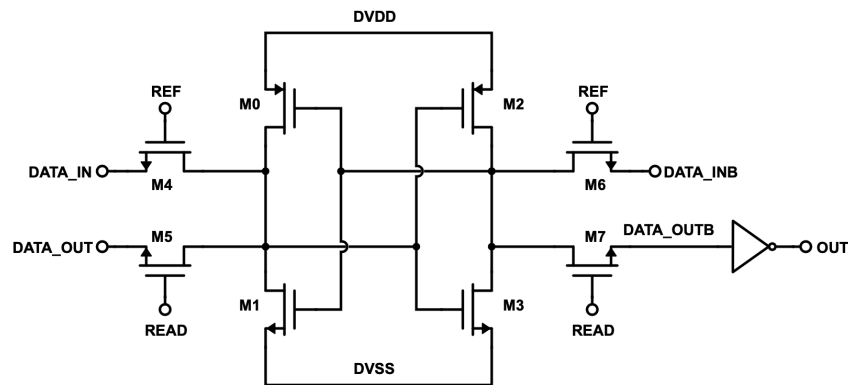


**Figure 4.6:** Schematic of the standard dual port RAM cell used as the basic memory element. An inverter is enough to convert the RAM data output signal to a full-swing digital pulse.

The way the RAM cells and the synchronisation blocks are organised within the layout of two double columns is shown in fig. 4.7. The four synchronisation blocks, two for the "blue" groups and two for the "red" groups of the two double columns are placed one above the other, taking up a total width of four columns ( $145.6 \mu\text{m}$ ) and a height of only  $157.3 \mu\text{m}$ . Each synchronisation block contains the full-custom layout of the  $28 \times 4$  RAM cells and the addressing logic needed to point to the correct rows for writing and reading, which was synthesised and laid out using digital place-and-route tools. The routing structure connecting the matrix signals to the inputs of the RAM again has a balanced capacitive load, and additional buffers and delay gates are added to the address lines to ensure that a timing misalignment of up to  $\sim 400$  ps with respect to the reference signal still results in the correct writing of the RAM cells.

### 4.3.2 Peripheral readout logic

The  $READ$  signal used to read out the data from the synchronisation memories is generated by the synchronous peripheral readout logic. This logic is designed to operate with the fast 640 MHz clock also used for storing the fine timestamp in the RAM cells. A block diagram of the readout logic is shown in fig. 4.8. When a data word is stored in one of the synchronisation memories, a signal is sent to the priority encoder logic denoting that a hit has been detected. The priority encoder then sends the  $READ$  signal to the corresponding memory. The data word from that memory is then transferred to a larger first-in-first-out (FIFO) memory, which is a standard clocked RAM memory with a depth of 64 words provided by the foundry. In the process, 4 double-column identifier bits are added to the 28-bit data word, as well as additional BCID

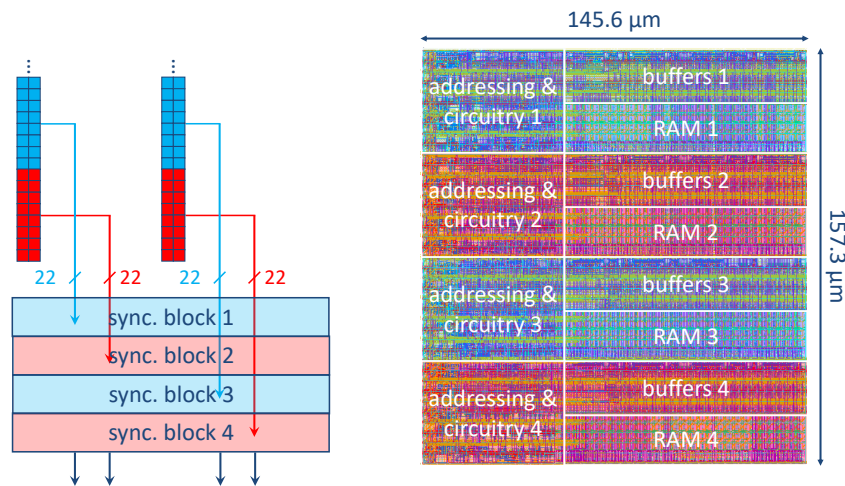


**Figure 4.7:** The organisation and layout of 4 synchronisation memories and the surrounding logic.

timestamping bits to allow the storage of the data word for a longer time without losing timing information, resulting in a 48-bit length of the data word. If there are multiple hits stored in the synchronisation memories, the priority encoder will give priority to the reading out of the leftmost memory (memory 0). The decision on which memory has the priority and the process of transferring hits from that memory to the large FIFO takes three 640 MHz clock cycles. With this kind of readout rate, simulations show that a synchronisation memory depth of four is enough to have negligible hit losses with the expected hit rates. The value of three bits for assigning the BCID timestamp during synchronisation also comes from the fact that, with the readout rates in question, eight 25 ns clock cycles are enough to read out the synchronised data in all cases.

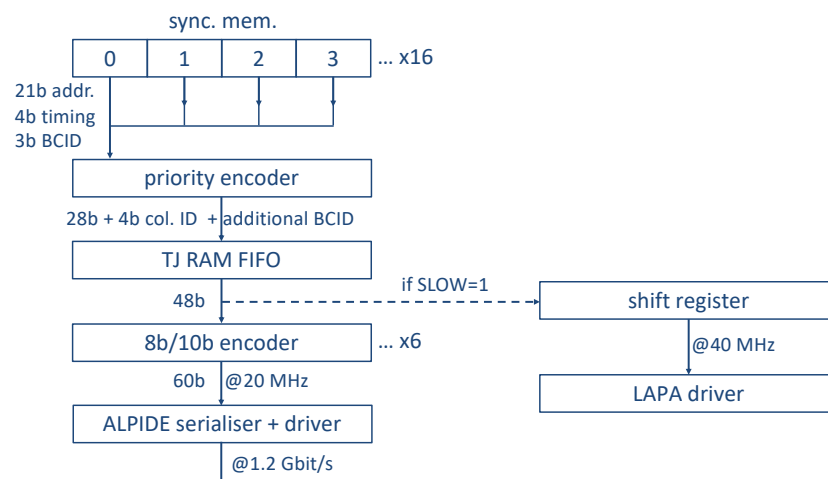


**Figure 4.8:** Block diagram of the logic used to read out the 16 synchronisation memories.

Once the data word is stored in the FIFO, it is read out in two 40 MHz clock cycles and sent to an 8b/10b encoder. This kind of encoding is commonly used to achieve a DC balanced code

when the resulting data word is serialised (the average number of zeros and ones transmitted is equal). This gives the possibility to AC couple the chip output to the readout systems, which is typically done in the experiments. Six 8b/10b encoders are used to encode the 48-bit data word into the final 60-bit data word. The parallel 60 bits are then fed to the ALPIDE data transmission unit, which serialises the bits and transmits them off-chip through a single LVDS data output at 1.2 Gb/s, using double data rate and a 600 MHz clock generated by the internal PLL.

As a backup feature, a so-called "slow" readout option has also been included in the peripheral readout logic. If this mode is enabled, the 48-bit data word at the output of the FIFO is directly serialised using a shift register with a slow clock of 40 MHz. This means that the time to transmit the serialised data is  $48 \times 25 \text{ ns} = 1.2 \text{ }\mu\text{s}$ , which is a factor of 24 slower than the "fast" readout using the ALPIDE DTU. In this case, the data is transmitted off-chip using the LAPA LVDS driver, already implemented and tested in MALTA. This mode of operation limits the maximum output bandwidth and readout rate of the chip, but preserves all the address and timing information, and provides a functionality equal to the "fast" readout for sufficiently low particle hit rates.

#### 4.4 Test results before and after irradiation

As was the case with MALTA, the fabricated miniMALTA chips are wirebonded to a PCB and read out with an FPGA, this time a Kintex KC705. One of the first tests performed is a DAC linearity scan, not only to test the performance of the redesigned DACs, but also to check the operation of the new configuring logic. The DAC currents and voltages are monitored by connecting a source meter to the DAC monitoring pads of the chip. The measured current and voltage values for different codes of a current DAC ( $I_{THR}$ ) and a voltage DAC ( $V_{HIGH}$ ) are shown in fig. 4.9. Both DACs show an excellent linearity, which is within 0.6%. The same

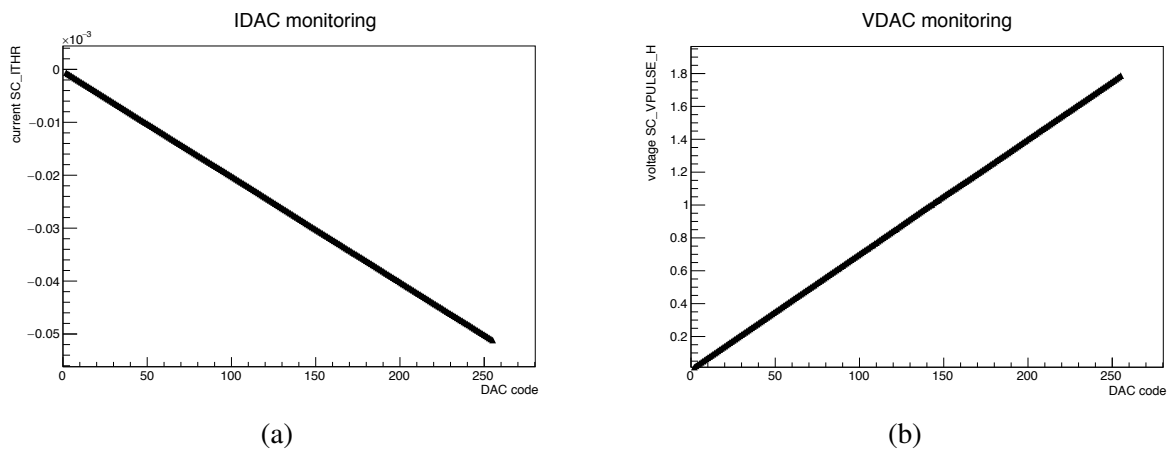


**Figure 4.9:** Linearity plots for (a) current DACs and (b) voltage DACs in the miniMALTA chip. In both cases the integral nonlinearity is below 0.6%.

plots have also been produced for the DACs on chips which had received up to 90 Mrad of TID. Apart from a slight decrease in the range of the current DACs, as expected from the TID-induced threshold voltage increase of the PMOS transistor generating the reference current, the functionality and linearity of the DACs remains within the same values as before irradiation. This confirms that the DACs and the digital logic used to configure them operate without problems even after irradiation.

The next step is to test the front-end performance of unirradiated devices, in particular to compare the two different front-end designs implemented on the chip. Again, this can be done by placing an  $^{55}\text{Fe}$  source over the pixels where the analogue output of the front-end amplifier can be monitored and comparing the resulting amplitude distributions. For this and all further measurements, the p-well voltage is set to  $-2\text{ V}$ , since it could not be increased to higher absolute values because the source/drain of a decoupling capacitor was mistakenly connected to this voltage, causing a breakdown of the gate oxide for the usual value of  $-6\text{ V}$ . However, already at  $-2\text{ V}$  of p-well bias, the n-implant around the collection electrode is depleted, so a small capacitance and a near-maximal amplifier output signal are already achieved. The substrate is biased at  $-6\text{ V}$ , and no signs of punchthrough between p-well and substrate are observed. Both monitored pixels use the original modified process without any of the new process improvements.

As expected, for the same DAC settings the front-end with the enlarged transistors M3 and M4 exhibits a higher gain, resulting in the K- $\alpha$  peak in the  $^{55}\text{Fe}$  spectrum shifted towards higher amplitudes, as seen in fig. 4.10. However, the difference in the peak amplitude and hence a

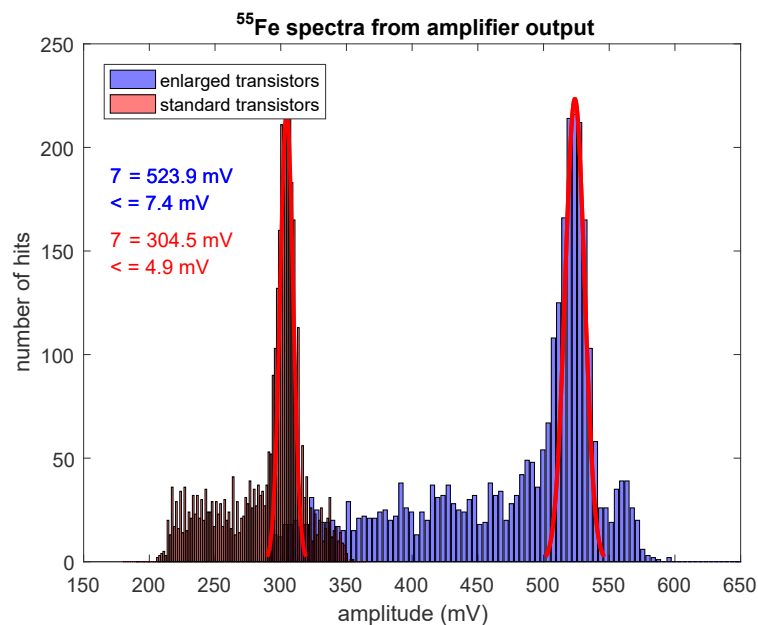


**Figure 4.10:** Comparison of  $^{55}\text{Fe}$  spectra obtained from the monitored amplifier outputs in the sectors with enlarged and standard transistors.

difference in gain of a factor of 1.7 is significantly higher than expected from simulations. This has raised some questions on the modelling of the output conductance of the devices, especially with reverse p-well bias and BSIM simulation models, which are being discussed with the foundry. Nevertheless, this significant gain increase makes it easier to achieve the desired low thresholds with the modified front-end. Note that the spectrum in the front-end with standard transistors is not to be compared with the spectra obtained from MALTA shown in the previous sections, since the front-end settings had to be adjusted to avoid saturating the  $OUT_A$  signal in the sector with enlarged transistors for the maximum charge deposited by the  $^{55}\text{Fe}$  source ( $I_{THR}$  had to be set to a high DAC code of 127).

The gain difference of a factor of 1.7 is confirmed by a threshold difference of a factor of 1.8 between the two front-end flavours, as seen in the threshold scans over the full matrix in fig. 4.11a. Again, the scan is performed using the pulse injection circuitry and by sweeping the value of  $V_{LOW}$ , obtaining the S-curves and converting the threshold value to electrons. The scan is performed at a temperature of  $-20^\circ\text{C}$  to be able to directly compare the threshold values with those of irradiated chips later on. Note that the temperature has quite an impact on the threshold, which decreases at lower temperatures, mainly due to an increase in the transconductance of the discriminator input transistor M9. Apart from the threshold difference between the two sectors, the threshold dispersion of the sector with enlarged transistors (sector 1, red curve) is also a factor of 2 lower than for the original front-end, since for a constant discriminator threshold the mismatch scales approximately with the charge threshold of the front-end. The relatively high thresholds in both sectors are a result of setting the discriminator threshold to a high value ( $I_{DB}$  DAC code of 100). Another interesting difference to observe between the two designs is the noise distribution shown in fig. 4.11b. The two sectors show a similar mean noise value, but the reduction in the number of pixels in the noise tail for the enlarged transistor sector is striking, resulting in a smaller RMS value of the noise distribution. This confirms that the tail in the

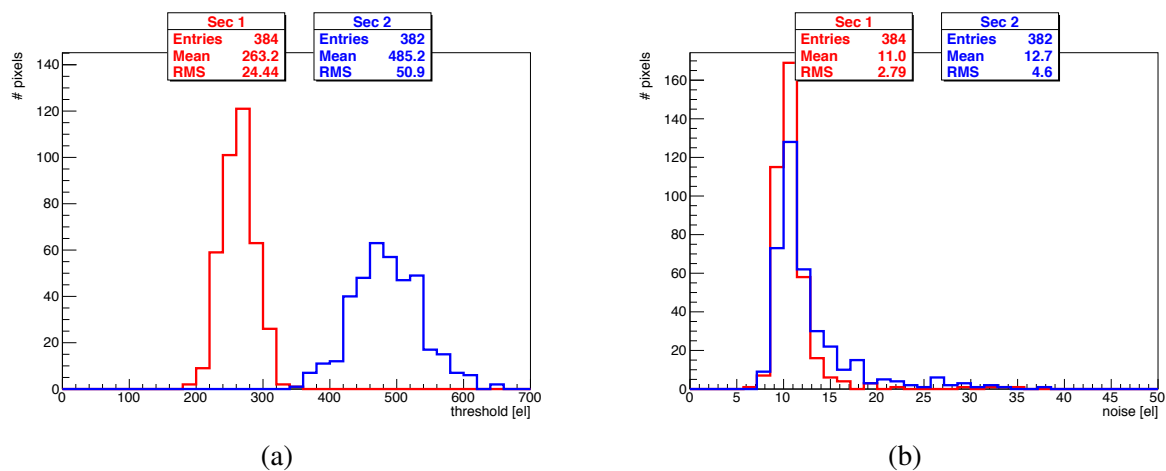


**Figure 4.11:** (a) Threshold and (b) noise distributions for the two sectors of an unirradiated miniMALTA chip. The left side of the matrix (red sector) has a lower threshold due to a higher front-end gain.

blue curve is indeed caused by random telegraph noise in transistor M3, and that increasing the area of this device by more than a factor of 2 almost completely removes the excessively noisy pixels, which is why the red curve resembles a Gaussian distribution much more.

Several miniMALTA chips have been irradiated with neutrons to NIEL fluences of  $10^{15}$   $n_{eq}/cm^2$  and  $2 \times 10^{15}$   $n_{eq}/cm^2$ . During irradiation, the chips have also received 1 Mrad and 2 Mrad of TID dose, respectively. The performance of the sensor and analogue front-end can once again be compared by acquiring  $^{55}Fe$  spectra from the monitored amplifier outputs. This comparison is shown in fig. 4.12. All the amplitude distributions were obtained from pixels with enlarged transistors and without any of the new process modifications. The p-well was biased at  $-2$  V, while the substrate was at a voltage of  $-6$  V. The front-end settings were once again adjusted to avoid saturating the analogue output in any of the samples, and are the same for all three samples compared. An increase in the mean signal amplitude of the K- $\alpha$  peak by about a factor of 1.2 is observed for the  $10^{15}$   $n_{eq}/cm^2$  sample compared to the unirradiated one. As mentioned before, this is attributed to the decrease of the collection electrode capacitance after irradiation. This has been confirmed by measuring the K- $\alpha$  peak amplitude on the collection electrodes themselves. A new feature in miniMALTA are additional monitoring pixels which buffer the voltage signal of the electrode itself, without amplification, and the monitored signal amplitudes show the same factor of 1.2 difference. Since the source followers used to buffer the electrode signals are designed for a gain close to 1, changes in the circuit can not explain an increase in signal after irradiation. One can also observe that the sensor and front-end are fully functional even after a fluence of  $2 \times 10^{15}$   $n_{eq}/cm^2$ . There is only a slight reduction in signal amplitude

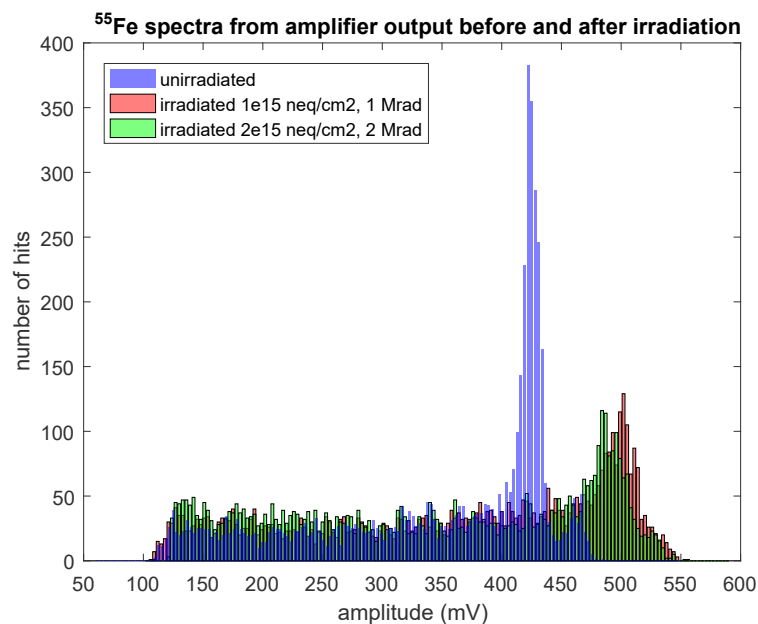


**Figure 4.12:** Comparison of  $^{55}Fe$  spectra obtained from the monitored amplifier outputs before and after neutron irradiation.

compared to the  $10^{15}$  n<sub>eq</sub>/cm<sup>2</sup> irradiated sample, which is attributed to a slight decrease in the front-end gain after TID. Nevertheless, the peak amplitude is still higher than before irradiation. The energy resolution is degraded to the point where it is difficult to resolve the K- $\alpha$  from the K- $\beta$  peak of the <sup>55</sup>Fe source, which is due to the noise increase also observed in MALTA.

The threshold and noise distributions of a chip irradiated to  $10^{15}$  n<sub>eq</sub>/cm<sup>2</sup> are shown in fig. 4.13. These are directly comparable to the distributions for the unirradiated chip shown in fig. 4.11, since the threshold scans were performed in the same conditions and with the same front-end settings. A decrease in threshold by a factor of 1.4 in both sectors is observed compared to the unirradiated samples. This is partly because of the decrease in input capacitance, but also because of a threshold decrease with TID due to a threshold voltage decrease in M9. The RMS threshold variation is similar to the unirradiated chips, so the ratio between mean threshold and RMS is somewhat degraded, but not the extent observed in MALTA. The mean noise values show a slight increase after irradiation, and the RTS noise tail, especially in the sector with the original front-end transistor sizes (blue curve), becomes much more prominent. A slight tail can now also be observed in the enlarged transistor sector, so increasing the size of M3 to even higher values in future designs will help to completely suppress RTS noise even after irradiation. Nonetheless, one can conclude that the new front-end with enlarged transistors provides a significant improvement compared to the MALTA front-end by increasing the gain, reducing the operating threshold and thereby the threshold dispersion, while almost completely eliminating RTS noise.

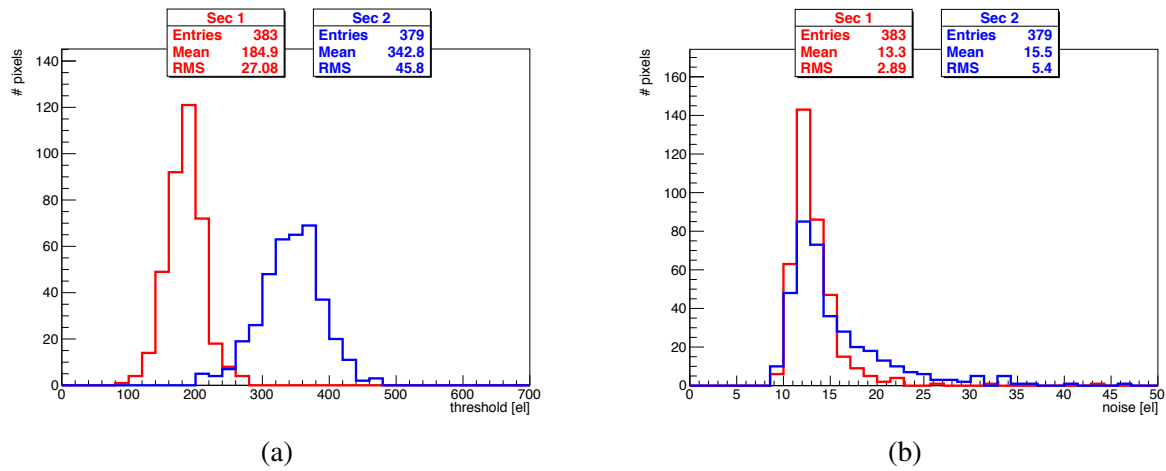


**Figure 4.13:** Threshold and noise distributions for the two sectors of a miniMALTA chip irradiated with neutrons to  $10^{15}$  n<sub>eq</sub>/cm<sup>2</sup>.

To assess the improvement in charge collection brought about by the new process modifications before measuring the detection efficiency in beam tests, one can acquire data from a <sup>90</sup>Sr source and compare the hit occupancies in sectors with different process changes. The difference in threshold between the two front-ends also has an impact on the occupancy, since more hits are likely to be detected at lower thresholds. The source is placed over the chip in a

way that it provides a close to uniform illumination of all sectors. The hit occupancies in all the sectors are uniform before irradiation, which is expected, since the detection efficiency of even the sector with a higher threshold and no process improvements is close to 100%, as seen from beam test results on unirradiated MALTAs. However, after irradiation, the hit rates show a very significant sector dependence, as seen in fig. 4.14. The most interesting comparison is between sectors in the bottom half of the chip, since the gradient of the source illumination should be negligible over such a small area. It is clear that the bottom quarter of the chip, which contains the sectors with the original modified process, sees a considerably smaller number of hits than the sectors above it, which include the additional extra-deep p-well near the pixel edges. The ratio between the number of hits in the sector with enlarged transistors (left hand side) and extra-deep p-well and the sector with the original transistors (right side) and original modified process is about 100/60, which is consistent with the efficiency results obtained from irradiated MALTA chips at these thresholds. The sectors with the gap in the n- layer on top of the chip show an even higher occupancy, which could be due to the source gradient and a few pixels with excessive noise rates which have not been masked. Note that to obtain this hit occupancy map, several noisy pixels on the right side had to be masked, while on the left side no pixels were masked at all. This is another confirmation that the enlarged M3 on the left side significantly reduces the RTS noise hit rates, since even with a lower threshold the number of noisy pixels is smaller. Also note that due to a problem in the biasing of the PMOS reset transistor, two sectors of the chip are disabled, resulting in no hits between rows 32 and 47.

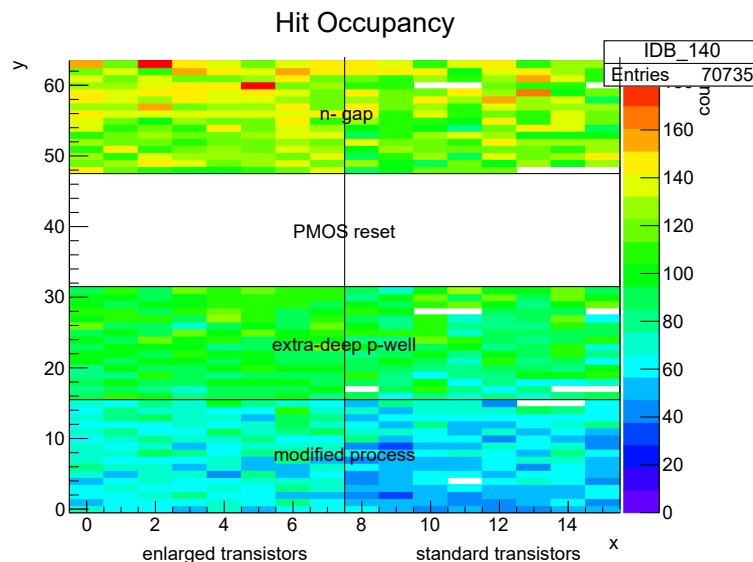
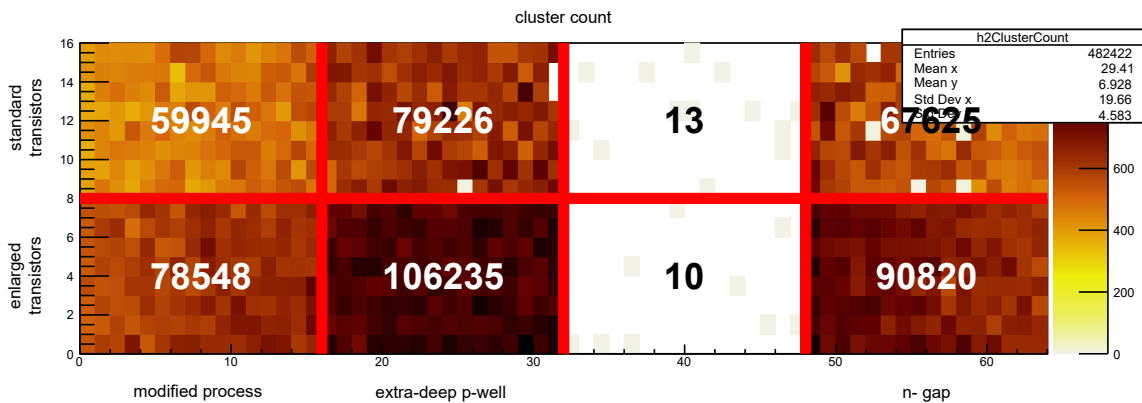


**Figure 4.14:** Hit occupancy over the full matrix during a  $^{90}\text{Sr}$  source acquisition after neutron irradiation to  $10^{15} \text{ n}_{\text{eq}}/\text{cm}^2$ . The sectors with lower threshold and process modifications show the highest occupancy.

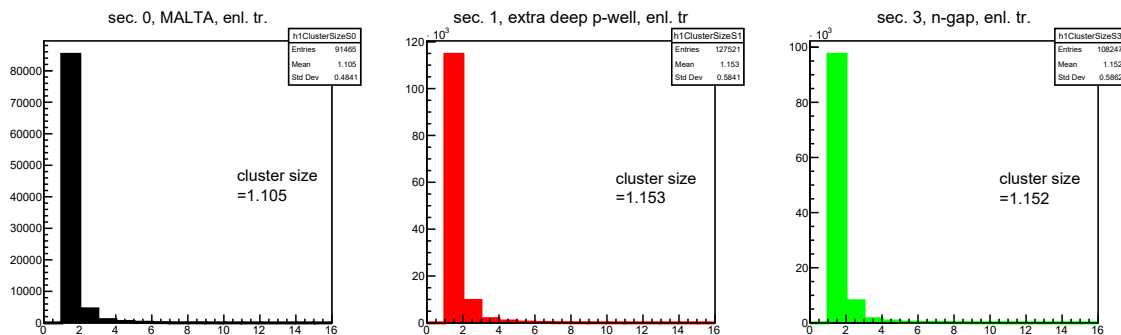
Apart from the difference in hit occupancy, the new process modifications should also affect the average number of hits in a cluster. Since the electric field in both the sensors with the extra-



deep p-well and the n- gap directs the charge more towards the electrode, a smaller average cluster size is expected. This is proven to be true for unirradiated samples, where the cluster size for a  $^{90}\text{Sr}$  source on the left side of the chip goes from 1.67 in the original modified process to 1.6 in the sectors with the gap in the n- layer. However, in samples irradiated to  $10^{15} \text{ n}_{\text{eq}}/\text{cm}^2$ , the trend is reversed and the original modified process has an average cluster size of 1.1, while both process improvements show a cluster size of 1.15. The reason for this is the loss of efficiency near the pixel edges in the original modified process. If charge is shared between multiple pixels, in most cases the particle is not detected at all, so hits with large cluster sizes are not seen, resulting in a reduced average cluster size for the original modified process. The reduction in cluster size for the two process improvements is still significant, but the fact that it stays higher than for the original modified process is already an indication of improved detection efficiency near the pixel boundaries. The cluster size distributions as well as the cluster occupancies for data from this  $^{90}\text{Sr}$  source acquisition are plotted in fig. 4.15. The threshold in the sectors with enlarged transistors is set to around  $280 \text{ e}^-$ , while for the original front-end it is around  $500 \text{ e}^-$ . In all three process flavours the cluster occupancy is higher in the enlarged transistor sectors, which means that there is a threshold dependence to the efficiency even with the new improved



(a)



(b)

**Figure 4.15:** (a) Cluster occupancy and (b) cluster size distribution for different sectors with enlarged transistors in miniMALTA after  $10^{15} \text{ n}_{\text{eq}}/\text{cm}^2$ .

sensor layouts, because a fraction of the hits are lost a high threshold of  $500 e^-$ . However, the difference between the extra-deep p-well sector and the original modified process sector with the same threshold is equally striking, indicating that the process improvements themselves could bring up to a factor of 1.35 increase in detection efficiency. Similar trends are also observed for samples irradiated to  $2 \times 10^{15} n_{eq}/cm^2$ , which confirms the new process modifications improve the charge collection even after higher irradiation fluences.

Four miniMALTA chips have also been irradiated with protons in the irradiation facility at the University of Birmingham [81]. Proton irradiations cause both NIEL and TID damage and are useful to assess the combined effects of high NIEL fluences on the sensor and high TID doses on the electronics. Once again, a comparison between the  $^{55}Fe$  spectra collected from three chips is made, as shown in fig. 4.16. With the same front-end settings, a factor of 1.13 decrease in signal amplitude is observed after irradiation to  $7 \times 10^{13} n_{eq}/cm^2$  and 9.3 Mrad. With this non-ionising fluence the effect on the input capacitance is still negligible, so a slight decrease in front-end gain due to TID causes this reduction in signal. However, after  $5 \times 10^{14} n_{eq}/cm^2$  and 66.5 Mrad the K- $\alpha$  peak shifts towards higher amplitudes, close to the unirradiated values, which is likely due to a combination of decreasing input capacitance and the front-end recovering after higher TID doses, as explained in sect. 2.4. The fact that the RMS of the K- $\alpha$  peak after proton irradiation to  $5 \times 10^{14} n_{eq}/cm^2$  is very similar to the unirradiated values is somewhat surprising, since after neutron irradiation to similar fluences the RMS showed an increase of up to a factor of two. Therefore, further proton irradiations are planned to confirm the findings in this measurement.

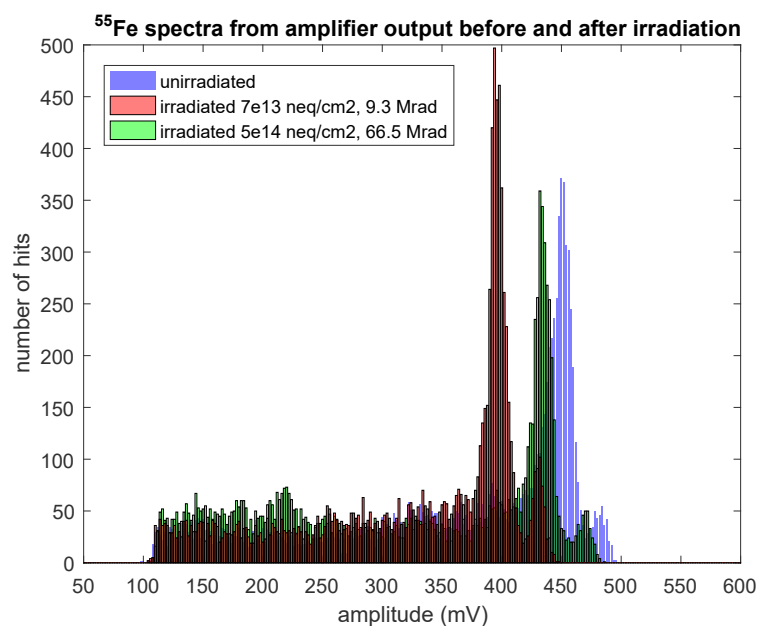


**Figure 4.16:** Comparison of  $^{55}Fe$  spectra obtained from the monitored amplifier outputs before and after proton irradiation.

Threshold scans have been performed on various chips for various levels of neutron and proton irradiation to compare the effects of different types of irradiation. The measured mean threshold values for different settings of the  $I_{DB}$  DAC current are summarised in fig. 4.17. Table 4.1 shows which chip has been irradiated to which level and with what type of particles. As already mentioned, the general trend is that for the same  $I_{DB}$  value the threshold decreases both with proton and neutron irradiation. Neutron irradiation seems to affect the threshold more because of the decrease in electrode capacitance after a high NIEL fluence and a decrease in the discriminator threshold due to TID. The effect on the discriminator threshold is the dominant effect after proton irradiation and still causes a decrease in threshold, though not as significant as

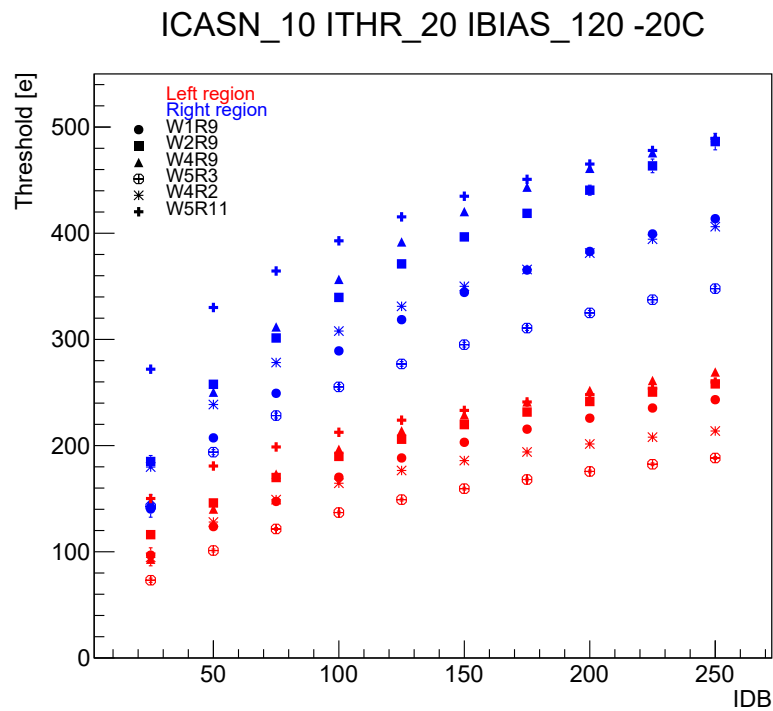


**Figure 4.17:** Comparison of threshold versus  $I_{DB}$  DAC value for an unirradiated, 2 neutron irradiated and 3 proton irradiated miniMALTA chips.

**Table 4.1:** List of miniMALTA chips and the levels to which they have been irradiated.

Chip	Irradiation type	NIEL fluence ( $n_{eq}/cm^2$ )	TID dose (Mrad)
W5R11	none	0	0
W4R9	proton	$7 \times 10^{13}$	9.3
W2R9	proton	$5 \times 10^{14}$	66.5
W1R9	proton	$7 \times 10^{14}$	91
W4R2	neutron	$1 \times 10^{15}$	1
W5R3	neutron	$2 \times 10^{15}$	2

with high neutron fluences. Note that by varying other front-end DAC settings one can achieve an even wider range of thresholds, and ultimately the only limiting factors as to how low one can go with the charge threshold after irradiation are the noise and threshold dispersion.

The performance of the readout architecture, especially the newly implemented synchronisation block has also been tested extensively. The previous measurements (threshold scans and source acquisitions) already prove that the pixel address data is read out correctly and that the asynchronous matrix signals can indeed be synchronised on-chip and read out using the synchronous periphery logic. For these measurements, the "slow" readout mode, where the data is serialised at 40 Mb/s, has been used. First measurements on the "fast" readout mode for high hit rates indicate that this mode of operation also functions correctly, but the firmware development for sampling the 1.2 Gb/s output signal is still ongoing.

An additional function of the synchronisation block is to add the 640 MHz fine time and 40 MHz BCID timestamps to the address words. An early test to check the validity of these timing bits is to look at the distribution of the fine time and BCID values in the data acquired while placing a  $^{90}\text{Sr}$  source over the chip. Since the timing of the particle hits is not correlated with any of the clocks, a uniform distribution for both counters is expected. The measured distributions for the BCID and fine time counter values are shown in fig. 4.18. The  $x$ -axis of the plots gives the value of the 4-bit fine time counter and the 15-bit BCID counter (added in the peripheral logic after synchronisation) values converted to a decimal number. Both distributions are uniform to within  $\pm 10\%$ . The slight non-uniformity stems from the fact that the period of counters used to generate these timestamps is not exactly balanced, so each value of the counter will have a slightly different duration than the others. In the case of the fine time, the simulated timing difference between the values matches almost exactly the measured distributions: a shorter duration for a given counter value results in less hits with that value within the distribution. This is already a good indication that the timestamps are stored correctly and that they can be used to obtain the time of arrival of hit signals to the periphery.

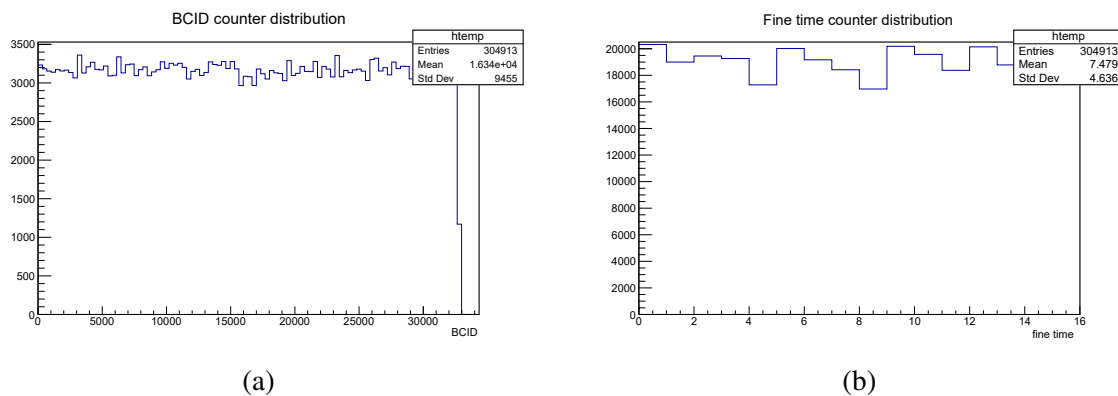


**Figure 4.18:** Distribution of (a) BCID and (b) fine time counter values during a  $^{90}\text{Sr}$  source acquisition. Both distributions are uniform within  $\pm 10\%$ .

The 640 MHz clock used in the peripheral readout logic and for the fine time counter is generated on the FPGA board and sent to the chip. Depending of the FMC cable connection between the chip and the FPGA, the clock signal can be degraded to the point where some of the data words coming from the chip do not contain the correct address information. Slowing the clock down to 320 MHz solves these problems, so most of the following tests are performed with this clock frequency. This implies a slower readout of the synchronisation memories, which does not present any limitation for the hit rates used in source tests and beam tests. It also implies that the resolution of the fine time counter is now one 320 MHz clock cycle, so around 3 ns. With this in mind, one can use the timestamps to obtain information about the timing difference of hits within clusters. An example for this is shown in fig. 4.19 for horizontal clusters between two double columns, so hits in neighbouring pixels within the same row, but in different groups of  $2 \times 8$ , therefore stored in different synchronisation memories. The hit data was acquired during a beam test, and the hit position on the sensor can be obtained from the beam telescope with a sub-pixel precision. When charge is shared equally among two pixels, the timing difference is close to 0, since the two pixel front-ends respond at approximately the same time. This happens if the charge is deposited very close to the boundary between the pixels. Fig. 4.19b shows that these hits (the red squares between pixel 0 and 1) indeed result in a timing difference of 0. As the hit position moves further away from the pixel edge, one pixel will collect the majority of the charge, while the other will collect only a small amount, so the average timing difference increases. As seen in fig. 4.19a, the vast majority of the hits come with a timing difference of less than 50 ns, as expected from the time walk curve of the amplifier. This confirms that the timing information from the counters is correct and that it can be used to at least qualitatively estimate the charge deposited in pixels of a cluster. Note that, for flexibility, the rising edges of two clocks used for timestamping (the 40 MHz and the 320 MHz) are not synchronised on-chip, but can be synchronised on the FPGA with a precision of one

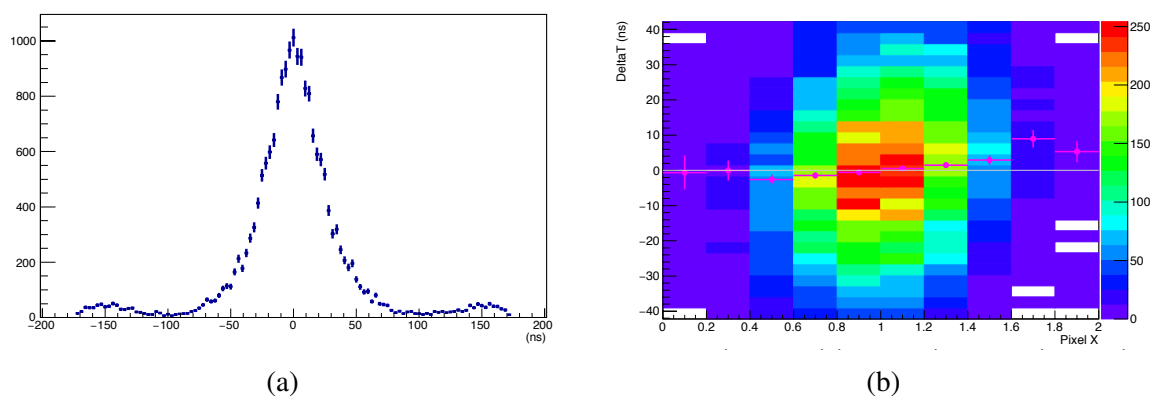


**Figure 4.19:** (a) Distribution of the timing difference between two pixels in a horizontal cluster between two double columns during a beam test and (b) the same timing difference versus hit position within the pixel.

320 MHz clock cycle. This still leaves a slight misalignment between the clocks, resulting in the fact that hits arriving close to the rising edge of the 40 MHz clock, within this misalignment window, can not be assigned the correct timing information in the offline analysis. This is why a small fraction of hits in the timing distribution is assigned the wrong delay value (around  $\pm 150$  ns). This can easily be solved by dividing the frequency of the fast clock on-chip and using this clock to generate the BCID counter value, which will probably be the case in future designs.

As was the case with MALTA, the detection efficiency of miniMALTA chips before and after irradiation has been measured in beam tests. Beam test campaigns have been carried out at the German Electron Synchrotron (DESY) and the ELSA electron accelerator in Bonn. The following results are taken from the beam tests at ELSA, where the miniMALTA (the DUT) and the beam telescope are placed in a 2.5 GeV electron beam. The six telescope planes used in these tests were actually unirradiated MALTA sensors, which provide a good position resolution for tracks on the DUT surface thanks to the small pixel size. However, the resolution is somewhat degraded due to multiple scattering effects caused by the low-energy electron beam, so the best resolution one can achieve is around 13  $\mu\text{m}$ . This limits the amount of in-pixel efficiency studies that can be performed, but is more than enough to determine the overall efficiency for different sectors of the miniMALTA chip. The reconstructed tracks are matched to hits from the DUT after applying a timing cut, and the efficiency is once again calculated as the number of matched tracks over the total number of reconstructed tracks.

The efficiency plots for an unirradiated miniMALTA sample with a 30  $\mu\text{m}$  thick epitaxial layer are shown in fig. 4.20a. The  $I_{DB}$  DAC setting of 20 results in a threshold of around 200  $e^-$  in sectors on the left-hand side and 380  $e^-$  on the right-hand side. The p-well and the substrate are biased at  $-2$  V and  $-6$  V, respectively. Pixels in the bottom right sector, which are identical to the MALTA design, show an efficiency of 98%, which matches the highest efficiency numbers measured on unirradiated MALTA chips. The process improvements in the sectors above increase the efficiency by an additional percent, while the combination of process improvements and low thresholds on the left-hand side brings the detection efficiency up to 99.8% in the sector with additional extra-deep p-well. This demonstrates that the process changes improve the charge collection even before irradiation, and that at low enough thresholds the sensor is fully efficient. Fig. 4.20b shown the detection efficiency measured for a sample irradiated with neutrons to  $10^{15}$   $n_{\text{eq}}/\text{cm}^2$ . During the measurement, the chip was cooled down to  $-20^\circ\text{C}$ . The  $I_{DB}$  setting of 100 corresponds to a threshold of 200  $e^-$  and 340  $e^-$  on the left and right side of the chip, respectively. Looking at the bottom right sector identical to MALTA, the efficiency of 78.8% again matches the highest values measured in MALTA beam tests quite well. The process improvements bring a significant efficiency increase of nearly 10%, even with the relatively high threshold of 340  $e^-$  on the right side. With lower thresholds obtained on the left side of the chip, the efficiency reaches an impressive 97.9% in the sector with the

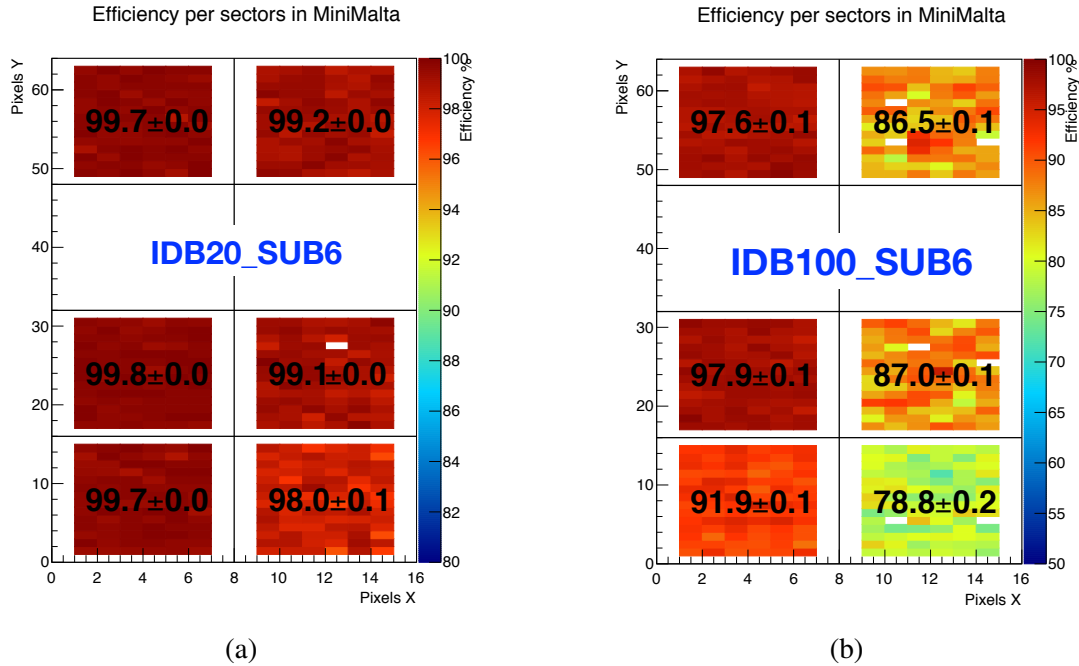


**Figure 4.20:** Efficiency in beam tests for different sectors of miniMALTA: (a) before irradiation, (b) after neutron irradiation to  $10^{15} \text{ n}_{\text{eq}}/\text{cm}^2$ .

additional extra-deep p-well. The sectors with extra-deep p-well consistently give a slightly higher efficiency than the sectors with the gap in the n– layer, indicating that the former process improvement is the better in terms of charge collection from a  $30 \mu\text{m}$  thick epitaxial layer.

A summary of efficiency measurements performed on two chips irradiated to  $10^{15} \text{ n}_{\text{eq}}/\text{cm}^2$  at different threshold settings is shown in fig. 4.21. The two chips differ between each other in terms of the thickness of the epitaxial layer, which is either  $25 \mu\text{m}$  or  $30 \mu\text{m}$ , as well as the depth of the n– layer, which was implanted at a different angle, using channelling for the former and

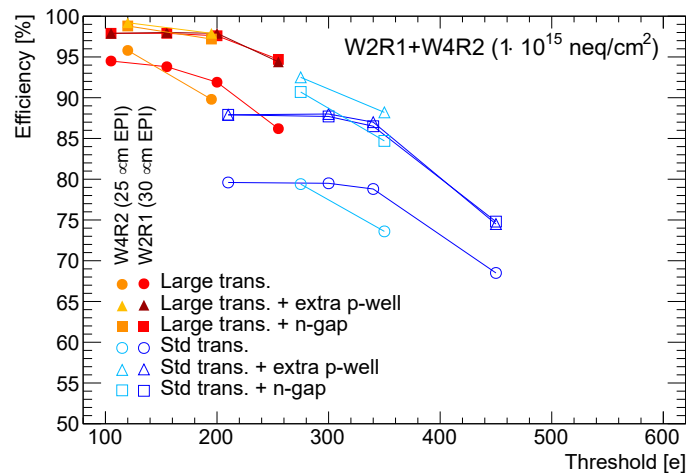


**Figure 4.21:** Efficiency versus threshold after neutron irradiation to  $10^{15} \text{ n}_{\text{eq}}/\text{cm}^2$ . The plot contains the combined data obtained from both sides of two chips at different threshold settings.

avoiding channelling for the latter thickness. The performance in terms of efficiency is similar for both wafer types, with a slightly higher efficiency achieved for the 25  $\mu\text{m}$  epitaxial layer thickness, where the difference between the extra-deep p-well and the n- gap is slightly more pronounced as well. In both cases the efficiency scales close to linearly with the threshold, before saturating at a value of 98-99% at the lowest achievable thresholds. In all cases, the sectors with process improvements show a significantly higher efficiency than the sectors with the original modified process, confirming that the increase in lateral electric field near the pixel borders indeed results in a much improved charge collection. Similarly, the improved front-end with the enlarged transistors gives a higher efficiency through a lower charge threshold, which can be achieved due to the decrease in RTS noise.

To check whether a high detection efficiency can be maintained for even higher fluences, miniMALTA chips irradiated to  $2 \times 10^{15} \text{ n}_{\text{eq}}/\text{cm}^2$  have also been tested during the same beam test campaigns. Efficiency results for one of these samples with a 30  $\mu\text{m}$  thick epitaxial layer are shown in fig. 4.22a. The charge threshold of the two sides of the chip was set around  $150 \text{ e}^-$  and  $280 \text{ e}^-$ . At the higher threshold of the two, one can observe that, after this fluence, even the process improvements are not enough to bring the efficiency above 70%. At a threshold of  $150 \text{ e}^-$ , the efficiency in the sectors with the process improvements reaches 91.6%. For the lowest achievable thresholds close to  $100 \text{ e}^-$  even higher numbers of up to 94% have been reached. This means that the best sectors on the chip are close to being fully efficient even

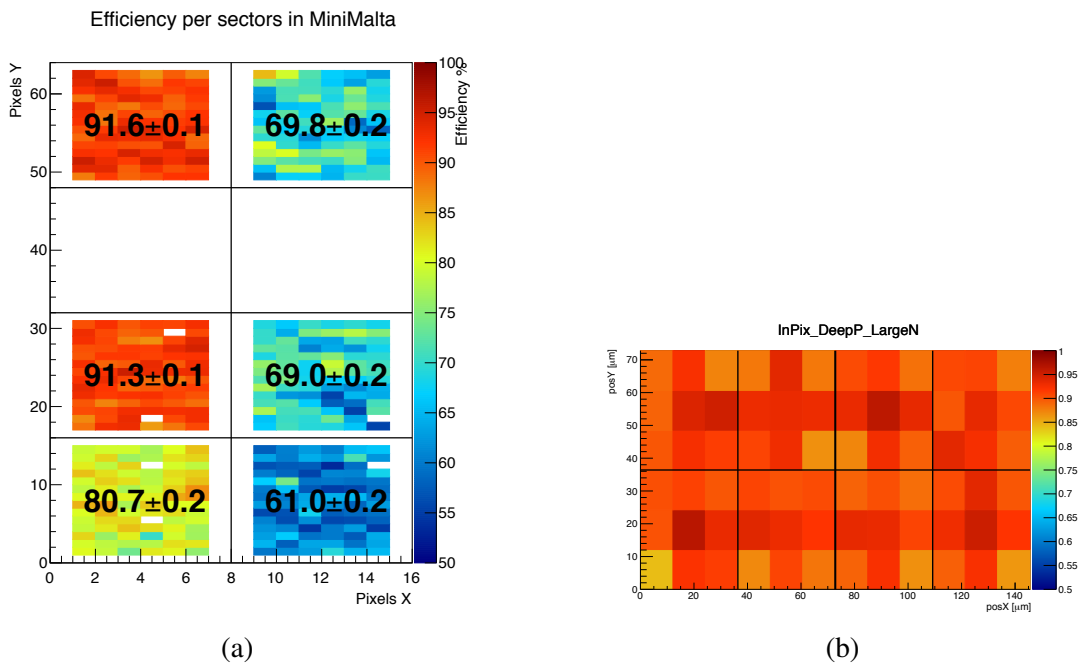


**Figure 4.22:** (a) Overall efficiency for different sectors of miniMALTA after neutron irradiation to  $2 \times 10^{15} \text{ n}_{\text{eq}}/\text{cm}^2$  and (b) in-pixel efficiency for a 4x2 pixel group with enlarged transistors and extra-deep p-well.



after a fluence of  $2 \times 10^{15}$  n<sub>eq</sub>/cm<sup>2</sup>. Looking at the in-pixel efficiencies for the sector with enlarged transistors and extra-deep p-well in fig. 4.22b, this time with a much coarser position resolution than for the MALTA in-pixel plots, as explained earlier, one can still correlate the slight efficiency loss in the best sectors with charge loss in the pixel corners. To further improve the detection efficiency, one would need to work at thresholds even lower than 100 e<sup>-</sup> or use a smaller pixel size with a redesigned front-end and readout logic to fit in the available area.

In conclusion, the improved front-end with increased gain and lower RTS noise implemented in the miniMALTA chip allows operating the chip at low thresholds down to 100 e<sup>-</sup>. At these thresholds and with the process modifications for improved charge collection near the pixel edges, the sensors are practically fully efficient even after irradiation to  $10^{15}$  n<sub>eq</sub>/cm<sup>2</sup>. The new digital periphery which synchronises the asynchronous signals from the pixel matrix has proven to be an efficient and low-power way of reading out the chip while preserving accurate timing information.

# Chapter 5

## Outlook for future design improvements

### 5.1 Further optimisation of analogue front-end circuitry

After the excellent results obtained with the miniMALTA sensors, design work is continuing towards a new generation of large pixel matrices in TowerJazz 180 nm. Since the baseline designs for the ATLAS pixel detector are still the hybrid solutions designed by the RD53 collaboration [82], new applications for large monolithic pixel sensors are also being investigated. Further improvements on the front-end circuitry are being pursued in order to further reduce the noise and threshold dispersion and achieve even lower operating thresholds, resulting in an even higher detection efficiency after high irradiation fluences. Different approaches for the readout of the large pixel matrices are also being investigated, either through an improved version of the MALTA-like asynchronous readout optimised for smaller pixel sizes, or through a more conservative synchronous column-drain type of architecture. The submission of two large matrices with all the improvements mentioned is planned for the end of 2019.

As far as the front-end design is concerned, a further increase in the area and output resistance of the M3 NMOS current source would result in a further reduction of RTS noise after irradiation and an even higher gain of the amplifier. A higher gain could also be beneficial for the threshold mismatch, since the input-referred mismatch coming from the discriminator stage is divided by the gain of the amplifier stage. Another way to significantly increase the gain is to increase the size of the source capacitance  $C_S$ , as explained in sect. 3.2.1. A re-layout of the front end with the length of M3 increased by an additional factor of 2 compared to the enlarged sectors of miniMALTA, as well as  $C_S$  increased by nearly an additional factor of 7, has already been included in a pixel size of  $33.04 \times 33.04 \mu\text{m}^2$ . Note that a smaller pixel pitch than  $36.4 \mu\text{m}$  is preferred mainly due to the improvement in charge collection near the pixel edges and the additional margin it provides in terms of the radiation hardness of the sensor.

Even though an increased gain helps in reducing the mismatch contribution of the second stage, measurements indicate that the dominant contribution is the threshold variation comes from the gain dispersion itself, caused by the variation on the output conductance of M3. The gain is defined by the total conductance seen from  $OUT_A$ , which includes mainly the output conductance of M3 and the transconductance of M6. For low  $I_{THR}$  settings which bring the highest gain, the M3 output conductance dominates, and the variation on this causes a larger dispersion than for high  $I_{THR}$  settings. Therefore, another potential improvement is to completely eliminate the contribution of the M3 output conductance, which can be achieved by cascoding this transistor. By adding a cascode M10, as shown in fig. 5.1, the conductance of the M3-M10 combination decreases by nearly two orders of magnitude. This also brings an additional increase in gain. The node at the M10 source introduces an additional pole which deteriorates the stability of the circuit, however, with a large  $C_S$  capacitance a phase margin of above  $60^\circ$  can still be achieved. Also, M10 can be made narrow and long for reduced capacitance on  $OUT_A$ , while M3 can be somewhat wider for a higher  $g_m$ .

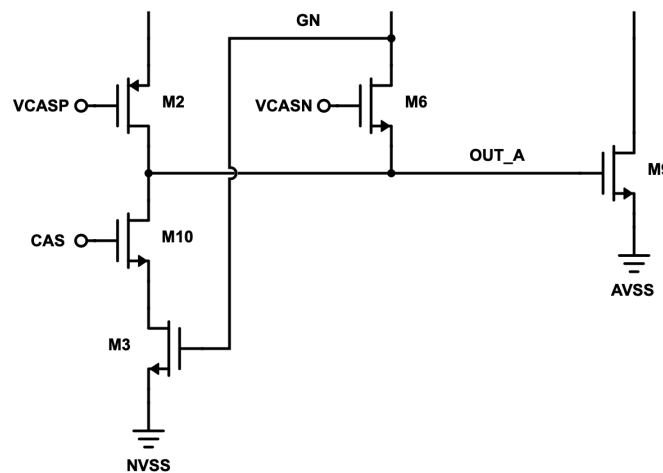


**Figure 5.1:** Transistors connecting to the  $OUT_A$  node in the front-end design with cascoded M3 (M10 is the cascode transistor).

An additional change in fig. 5.1 is that the M2 cascode is now biased by a DAC voltage  $V_{CASP}$  to have more margin with the saturation of transistors above it. Also note that the grounds of the main branch of the amplifier (node  $NVSS$ ) and the discriminator ground ( $AVSS$ ) have been split. In times of high hit activity, when multiple discriminators are firing and consuming significant current, a common ground could mean a transient voltage increase on the source of M3 in case the resistance of the ground connection is not negligible, resulting in a voltage signal on  $OUT_A$  which could lead to fake hits. This phenomenon is completely avoided if the two grounds are connected to different ground lines which are only connected together at the pad level or on the PCB.

A simulation comparing the transient response of the miniMALTA front-end with enlarged M3 and the newly designed front-end with cascoded M3 for an input charge of  $200 e^-$  is shown in fig. 5.2. With the same front-end settings, adjusted for the miniMALTA front-end to have a threshold of around  $200 e^-$ , the new design exhibits a factor of 3 higher gain, which makes any mismatch contribution from the second stage negligible when referred back to the input. Note that the front-end biases need to be adjusted to achieve the desired threshold with the cascoded front-end ( $I_{THR}$  has to be increased to have a threshold sufficiently higher than the noise levels, around  $100 e^-$ ). Also note that, in the simulation, the gate voltage of the clipping transistor has been adjusted for a discriminator pulse width which is still within the simulation window. By further decreasing this gate voltage one can achieve a faster clipping and keep the duration of the pulses within the desired few hundred nanoseconds.

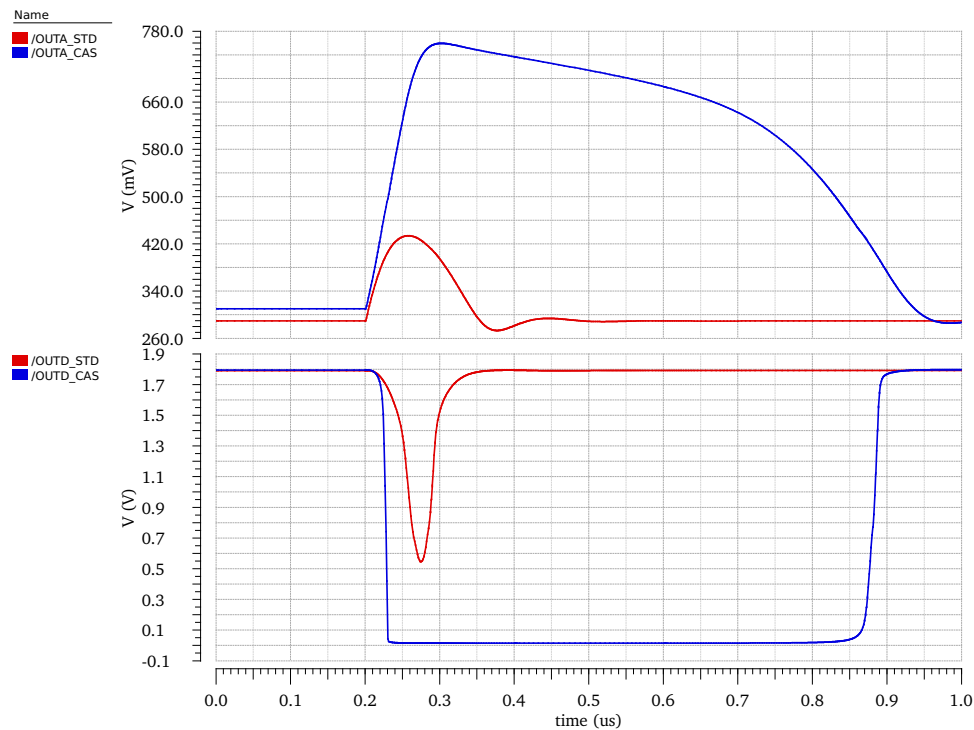


**Figure 5.2:** Comparison of simulated waveforms on  $OUT_A$  and  $OUT_D$  between the miniMALTA enlarged front-end and the new cascoded design with an input charge of  $200 e^-$ . The gain of the cascoded front-end is a factor of 3 higher.

A linearised noise analysis shows that, with a sensor leakage current of  $10 \text{ pA}$ , the RMS noise level on  $OUT_A$  of  $4.61 \text{ mV}$  for the cascoded front-end is about 10% lower than the previous design, mainly due to the reduction in the  $1/f$  noise component of transistor M3. However, because of the higher gain, the new front-end can achieve a signal amplitude of  $148.11 \text{ mV}$  with only  $100 e^-$  of input charge, effectively doubling the signal-to-noise ratio compared to the original design. Monte Carlo simulations are also performed to assess the improvements in threshold variation. The resulting S-curve is shown in fig. 5.3. At a threshold of  $100 e^-$ , the

simulated mismatch RMS is less than  $3 e^-$ , which is a factor of 2.7 improvement compared to the original design. Apart from that, since the variation on the output conductance of M3 now causes only a marginal variation in the gain of the circuit, the measured variation is expected to match the simulated one better than for the previous design. Note that a higher gain and lower operating threshold also mean a lower in-time threshold of the front-end, which is beneficial for the in-time efficiency and time resolution of the circuit.

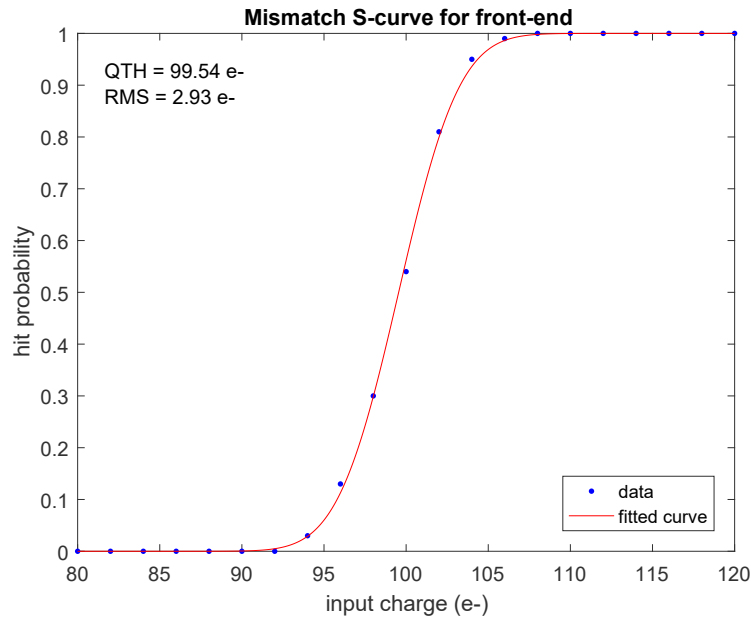


**Figure 5.3:** Simulated mismatch S-curve for the front-end with cascode. At a threshold setting of  $100 e^-$ , the mismatch RMS is reduced by a factor of 2.7 compared to the front-end implemented in miniMALTA.

## 5.2 In-pixel threshold tuning

As mentioned in sect. 3.5.1, a per-pixel threshold tuning mechanism is being investigated for future designs as an additional handle to reduce the charge threshold variation in a large pixel matrix. A circuit has already been designed to include a 3-bit storage and threshold tuning DAC inside the pixel, while minimising the area and maximising the robustness of the threshold adjustment. The idea is store the bit combination corresponding to the desired threshold value in three in-pixel set-reset (SR) latches using the standard schematic of two custom NOR gates in feedback, shown in fig. 5.4a. The set and reset signals are provided for each column, so an additional "enable" signal is needed to select the row in which the bits are to be written. The schematic of the NOR gate which includes this enabling signal is shown in fig. 5.4b. The set or reset signals asserted to the  $IN$  port of the NOR gate are stored only if the  $EN$  enable signal is active, allowing the storage of the bits individually for each pixel. A functionality to send the

desired set and reset signals for each column individually or for all columns at the same time is foreseen at the digital periphery.

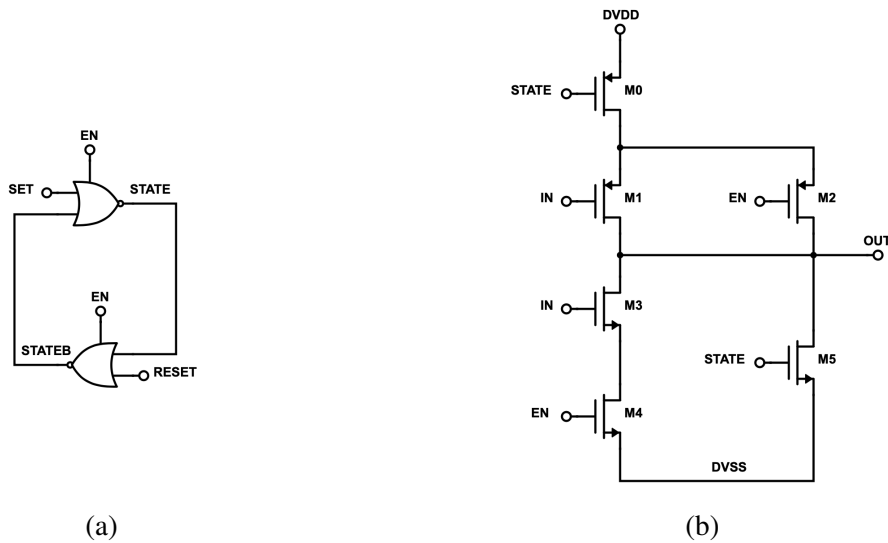


**Figure 5.4:** Circuits used to store the 3 threshold tuning bits within the pixel: (a) latch using two NOR gates with an enable signal, (b) schematic of the NOR gate itself.

If all three latches within the pixel are reset, and hence code 000 is written, the pixel is masked and no output pulse can be generated by the front-end discriminator. This also allows the masking of individual pixels within the matrix, without relying on the intersection between a vertical, horizontal and diagonal masking line as in previous designs, thus eliminating the possibility of unintentionally masked "ghost" pixels. The other seven possible codes that can be written in the three bits decide between seven possible threshold values. The way this is realised is that seven voltages are provided for each double column, each voltage corresponding to a gate voltage needed for a certain  $I_{DB}$  current setting. The three bits control the gates of PMOS transistors acting as switches and connecting one of the seven lines to the gate of the  $I_{DB}$  current source. Therefore, the stored 3-bit combination will decide between seven  $I_{DB}$  settings and hence seven different settings for the discriminator threshold, thus adjusting the charge threshold of the particular front-end. The seven potential gate voltages are provided by a current DAC summing the nominal  $I_{DB}$  current with an  $I_{TRIM}$  current at the analogue chip periphery. By adjusting  $I_{TRIM}$  one can also adjust the range of  $I_{DB}$  values in the pixels required to correct a certain threshold dispersion.

An analogue simulation with capacitances extracted from the layout of the threshold tuning block, demonstrating the functionality of the tuning circuitry, is shown in fig. 5.5. The values of the  $I_{DB}$  and  $I_{TRIM}$  DAC current were set to 500 nA and 70 nA, respectively. First, a set pulse on bit 0 and reset pulses on bits 1 and 2 are sent to the tuning cell, resulting in code 001 being stored on bits  $Q[2:0]$  if the  $EN$  signal is at a high level. This sets the  $I_{DB}$  gate voltage to the highest possible value, resulting in the lowest possible  $I_{DB}$  current setting of 500 nA and

the lowest possible threshold of the discriminator. After that, set pulses are sent on all three bits, lowering the  $I_{DB}$  gate voltage and changing the  $I_{DB}$  current setting to its highest value of 920 nA, which results in the highest charge threshold. By changing the  $I_{DB}$  setting in this range, the charge threshold for a miniMALTA-like front-end increases from  $200 e^-$  to about  $230 e^-$ . The  $I_{TRIM}$  DAC current can be increased if a larger range of threshold adjustment is needed. Note that the width of the set/reset pulses controlled by the digital periphery was set to 200 ns in this simulation, and can be further reduced if a faster tuning over all pixels is needed.

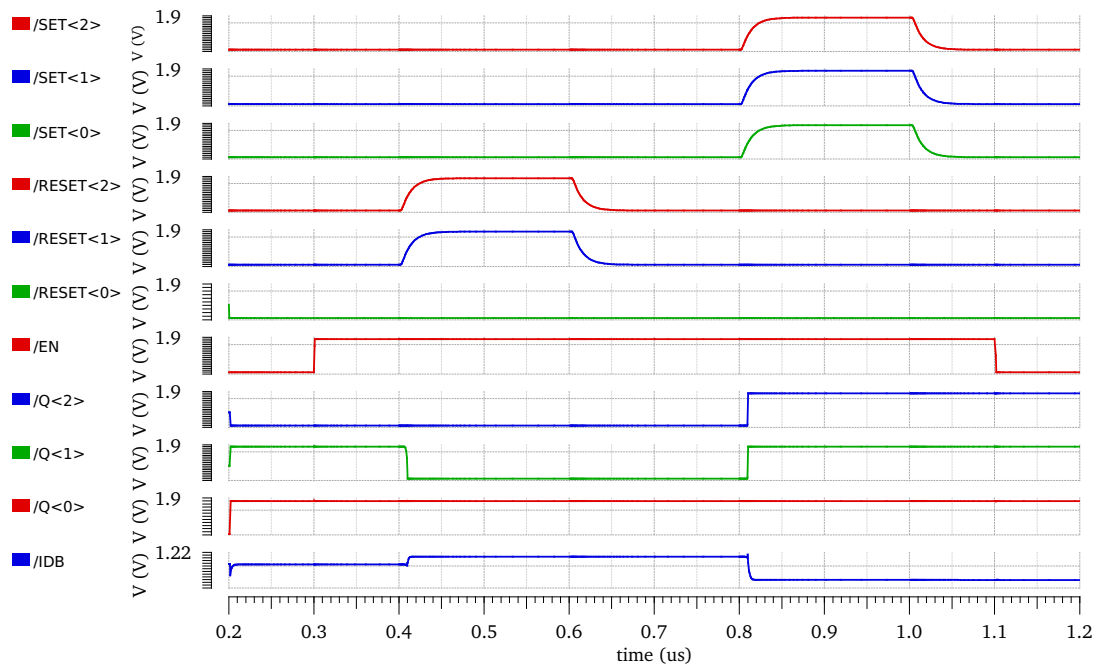


**Figure 5.5:** Simulation demonstrating the functionality of the in-pixel threshold tuning circuitry. The  $I_{DB}$  gate voltage is changed when a 3-bit code is written in the tuning latches.

The layout of the analogue part of a  $33.04 \times 33.04 \mu\text{m}^2$  pixel, including the improved version of the front-end with an enlarged capacitance  $C_S$  and the cells for the threshold tuning is shown in fig. 5.6. The layout also includes the routing structure for all the analogue bias voltages as well as the signals required for the addressing and operation of the tuning cells. The redesign of the digital part of the pixel in order to fit it in the available area is ongoing, and a large matrix of these pixels will be included in the next TowerJazz engineering run at the end of 2019.

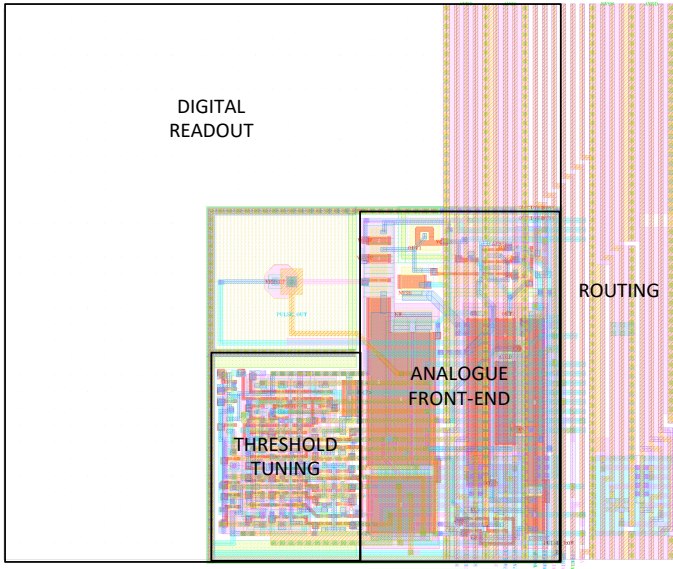


**Figure 5.6:** Layout of the analogue part of a  $33.04 \times 33.04 \mu\text{m}^2$  pixel which includes the threshold tuning circuitry.



# Chapter 6

## Conclusion

Monolithic pixel detectors combining the sensor and the readout electronics in the same piece of silicon can have a significant advantage over their hybrid counterparts in terms of power consumption, material budget and cost. For that reason, novel radiation-hard monolithic active pixel sensors are being considered for the inner tracking layers of the high energy physics experiments at CERN. Achieving sufficient radiation tolerance even for the most extreme radiation levels close to the particle interaction point requires charge collection by drift and uniform depletion of the sensitive layer, as well as the development of radiation-hard front-end and readout electronics.

Monolithic active pixel sensors in the TowerJazz 180 nm CMOS technology have been designed to meet the specifications of the outer pixel layers in the upgraded ATLAS Inner Tracker. After encouraging results obtained from prototype chips, design activity has been started to develop large-scale sensors with small collection electrodes using a novel process modification to fully deplete the sensitive layer and achieve sufficient radiation hardness. The MALTA sensor contains a matrix of  $512 \times 512$  pixels with a pitch of  $36.4 \mu\text{m}$ , and uses a fast, low-power, low-noise analogue front-end inside each pixel for amplification and hit discrimination. The digital hit signals of the discriminators are read out using a novel asynchronous readout architecture which avoids propagating a clock to the pixel matrix in order to reduce the digital power consumption and increase the hit rate capability.

Measurement results on the produced MALTA sensors demonstrate the functionality of the analogue and digital circuitry implemented, and show excellent timing characteristics for both parts. However, higher than expected levels of RTS noise, which have been linked to the small dimensions of a transistor within the front-end, combined with the larger than expected pixel-to-pixel threshold variation, prevent operating the chip at very low charge thresholds. Nevertheless, even at higher thresholds, the unirradiated sensors show close to full detection efficiency in particle beam tests. The chips remain fully functional even after irradiation to  $10^{15} \text{ n}_{\text{eq}}/\text{cm}^2$ , but an efficiency loss is observed near the pixel boundaries, which has been linked to the lack

of lateral electric field pushing the charge towards the small collection electrode, resulting in a charge loss due to trapping. This, in combination with the higher operating thresholds, prevents the detection efficiency from reaching the desired values.

To address the efficiency loss after irradiation, two new process changes have been developed to increase the lateral field near the pixel boundaries. These modifications, together with improvements on the front-end for higher gain and reduced RTS noise, have been included in miniMALTA, a small-scale redesign of the MALTA sensor. Additional digital circuitry to synchronise the asynchronous matrix signals at the chip periphery has also been included. Measurements show a significant improvement in terms of front-end gain and RTS noise, as well as a much improved detection efficiency after irradiation in the sectors with the process changes. The improved charge collection together with the lower operating thresholds achievable allow the sensor to be close to fully efficient even after  $10^{15}$  n<sub>eq</sub>/cm<sup>2</sup>.

Design work is continuing on the next iteration of large-scale monolithic sensors in TowerJazz 180 nm. Further improvements on the front-end circuitry, including a per-pixel threshold tuning to reduce the threshold variation, are being investigated to lower the operating thresholds even further in order to achieve a high detection efficiency after even higher irradiation fluences. The improved front-end will be included in two large pixel matrices with different readout architectures, which will be a part of the next TowerJazz engineering run at the end of 2019.

# Bibliography

- [1] Garoby, R., “Scenarios for upgrading the LHC injectors”, in LHC-LUMI-06 Proceedings, January 2006.
- [2] The ATLAS Collaboration *et al.*, “The ATLAS experiment at the CERN Large Hadron Collider”, Journal of Instrumentation, Vol. 3, No. 08, August 2008, pp. S08003.
- [3] The CMS Collaboration *et al.*, “The CMS experiment at the CERN LHC”, Journal of Instrumentation, Vol. 3, No. 08, August 2008, pp. S08004.
- [4] The ALICE Collaboration *et al.*, “The ALICE experiment at the CERN LHC”, Journal of Instrumentation, Vol. 3, No. 08, August 2008, pp. S08002.
- [5] The LHCb Collaboration *et al.*, “The LHCb detector at the LHC”, Journal of Instrumentation, Vol. 3, No. 08, August 2008, pp. S08005.
- [6] Evans, L., Bryant, P., “LHC machine”, Journal of Instrumentation, Vol. 3, No. 08, August 2008, pp. S08001.
- [7] The ATLAS Collaboration, ATLAS: technical proposal for a general-purpose pp experiment at the Large Hadron Collider at CERN, ser. LHC Tech. Proposals. Geneva: CERN, 1994, available at: <https://cds.cern.ch/record/290968>
- [8] Wermes, N., “Pixel vertex detectors”, in 34th SLAC Summer Institute On Particle Physics, July 2006, pp. 1-31.
- [9] Apollinari, G., Alonso, I. B., Brüning, O., Fessia, P., Lamont, M., Rossi, L., Taviani, L., High-Luminosity Large Hadron Collider (HL-LHC): Technical Design Report V. 0.1. Geneva, Switzerland: CERN, 2017, available at: <http://cds.cern.ch/record/2284929>
- [10] Backhaus, M., “The upgraded Pixel Detector of the ATLAS Experiment for Run 2 at the Large Hadron Collider”, Nuclear Instruments and Methods in Physics Research Section A: Accelerators, Spectrometers, Detectors and Associated Equipment, Vol. 831, 2016, pp. 65-70, Proceedings of the 10th International “Hiroshima” Symposium on the Development and Application of Semiconductor Tracking Detectors.

- [11] The ATLAS Collaboration, “Technical Design Report for the ATLAS Inner Tracker Strip Detector”, CERN, Geneva, Switzerland, Tech. Rep. CERN-LHCC-2017-005.ATLAS-TDR-025, April 2017, available at: <https://cds.cern.ch/record/2257755>
- [12] Tlustos, L., “Performance and limitations of high granularity single photon processing X-ray imaging detectors”, Doctoral thesis, Technische Universität Wien, Vienna, Austria, 2005, available at: <https://cds.cern.ch/record/846447>
- [13] Hemperek, T., “Exploration of advanced CMOS technologies for new pixel detector concepts in High Energy Physics”, Doctoral thesis, Rheinische Friedrich-Wilhelms-Universität, Bonn, Germany, October 2015, available at: <https://hss.ulb.uni-bonn.de/2018/5035/5035.htm>
- [14] Perić, I., Blanquart, L., Comes, G., Denes, P., Einsweiler, K., Fischer, P., Mandelli, E., Meddeler, G., “The FEI3 readout chip for the atlas pixel detector”, Nuclear Instruments and Methods in Physics Research Section A: Accelerators, Spectrometers, Detectors and Associated Equipment, Vol. 565, No. 1, 2006, pp. 178-187, Proceedings of the International Workshop on Semiconductor Pixel Detectors for Particles and Imaging.
- [15] Garcia-Sciveres, M. *et al.*, “The FE-I4 pixel readout integrated circuit”, Nuclear Instruments and Methods in Physics Research Section A: Accelerators, Spectrometers, Detectors and Associated Equipment, Vol. 636, No. 1, Supplement, 2011, pp. S155-S159, Proceedings of the 7th International “Hiroshima” Symposium on the Development and Application of Semiconductor Tracking Detectors.
- [16] van Hoorne, J. W., “Study and Development of a novel Silicon Pixel Detector for the Upgrade of the ALICE Inner Tracking System”, Doctoral thesis, Technische Universität Wien, Vienna, Austria, October 2015, available at: <https://cds.cern.ch/record/2119197>
- [17] Garcia-Sciveres, M., Wermes, N., “A review of advances in pixel detectors for experiments with high rate and radiation”, Reports on Progress in Physics, Vol. 81, No. 066101, May 2018, pp. 1-43.
- [18] Fano, U., “Ionization yield of radiations. II. The fluctuations of the number of ions”, Physical Review, Vol. 72, July 1947, pp. 26-29.
- [19] Eidelman, S. *et al.*, “Review of Particle Physics”, Physics Letters B, Vol. 592, 2004, pp. 1+, available at: <http://pdg.lbl.gov>
- [20] Sternheimer, R. M., “The density effect for the ionization loss in various materials”, Physical Review, Vol. 88, November 1952, pp. 851-859.

- [21] Landau, L. D., “On the energy loss of fast particles by ionization”, *Journal of Physics*, Vol. 8, No. 4, 1944, pp. 201-205.
- [22] Bichsel, H., “Straggling in thin silicon detectors”, *Reviews of Modern Physics*, Vol. 60, July 1988, pp. 663-699.
- [23] Seltzer, S. M., Berger, M. J., “Evaluation of the collision stopping power of elements and compounds for electrons and positrons”, *The International Journal of Applied Radiation and Isotopes*, Vol. 33, No. 11, 1982, pp. 1189-1218.
- [24] Tsai, Y.-S., “Pair production and bremsstrahlung of charged leptons”, *Reviews of Modern Physics*, Vol. 46, October 1974, pp. 815-851.
- [25] p–n junction, available at: [https://en.wikipedia.org/wiki/P-n\\_junction](https://en.wikipedia.org/wiki/P-n_junction)
- [26] Streetman, B. G., Banerjee, S. K., *Solid State Electronic Devices*, 6th ed. New Jersey, USA: Pearson Education Inc., 2009.
- [27] Sze, S., *Physics of Semiconductor Devices*. New Jersey, USA: John Wiley & Sons, 1981.
- [28] Ramo, S., “Currents induced by electron motion”, *Proceedings of the Institute of Radio Engineers*, Vol. 27, No. 9, September 1939, pp. 584-585.
- [29] Rossi, L., Fischer, P., Rohe, T., Wermes, N., *Pixel Detectors: From Fundamentals to Applications*. Berlin, Germany: Springer, 2006.
- [30] Srour, J. R., Marshall, C. J., Marshall, P. W., “Review of displacement damage effects in silicon devices”, *IEEE Transactions on Nuclear Science*, Vol. 50, No. 3, June 2003, pp. 653-670.
- [31] Hoffelner, W., “Irradiation damage in nuclear power plants”, in *Handbook of Damage Mechanics: Nano to Macro Scale for Materials and Structures*, Voyiadjis, G. Z., (ed.). New York, USA: Springer, 2015, pp. 1427-1461.
- [32] Gregory, B. L., Sander, H. H., “Injection Dependence of Transient Annealing in Neutron-Irradiated Silicon Devices”, *IEEE Transactions on Nuclear Science*, Vol. 14, December 1967, pp. 116-126.
- [33] Snoeys, W., “CMOS monolithic active pixel sensors for high energy physics”, *Nuclear Instruments and Methods in Physics Research Section A: Accelerators, Spectrometers, Detectors and Associated Equipment*, Vol. 765, 2014, pp. 167-171, *Proceedings of the 9th International “Hiroshima” Symposium on Development and Application of Semiconductor Tracking Detectors (HSTD-9 2013)*.

- [34] Snoeys, W., “Monolithic pixel detectors for high energy physics”, Nuclear Instruments and Methods in Physics Research Section A: Accelerators, Spectrometers, Detectors and Associated Equipment, Vol. 731, 2013, pp. 125-130, PIXEL 2012.
- [35] Dorokhov, A. *et al.*, “High resistivity CMOS pixel sensors and their application to the STAR PXL detector”, Nuclear Instruments and Methods in Physics Research Section A: Accelerators, Spectrometers, Detectors and Associated Equipment, Vol. 650, Sep. 2011, pp. 174-177.
- [36] Peric, I., “A novel monolithic pixelated particle detector implemented in high-voltage CMOS technology”, Nuclear Instruments and Methods in Physics Research Section A: Accelerators, Spectrometers, Detectors and Associated Equipment, Vol. 582, No. 3, 2007, pp. 876-885, VERTEX 2006.
- [37] Kemmer, J., Lutz, G., “New structures for position sensitive semiconductor detectors”, Nuclear Instruments and Methods in Physics Research Section A: Accelerators, Spectrometers, Detectors and Associated Equipment, Vol. 273, No. 2, 1988, pp. 588-598.
- [38] Arai, Y. *et al.*, “Development of SOI pixel process technology”, Nuclear Instruments and Methods in Physics Research Section A: Accelerators, Spectrometers, Detectors and Associated Equipment, Vol. 636, No. 1, Supplement, 2011, pp. S31-S36, Proceedings of the 7th International “Hiroshima” Symposium on the Development and Application of Semiconductor Tracking Detectors.
- [39] Goiffon, V., Virmontois, C., Magnan, P., Cervantes, P., Corbiere, F., Estriebeau, M., Pinel, P., “Radiation damages in CMOS image sensors: Testing and hardening challenges brought by deep sub-micrometer CIS processes”, Proceedings of SPIE - The International Society for Optical Engineering, Vol. 7826, October 2010.
- [40] Oldham, T. R., McLean, F. B., “Total ionizing dose effects in MOS oxides and devices”, IEEE Transactions on Nuclear Science, Vol. 50, No. 3, June 2003, pp. 483-499.
- [41] Faccio, F., Cervelli, G., “Radiation-induced edge effects in deep submicron CMOS transistors”, IEEE Transactions on Nuclear Science, Vol. 52, No. 6, December 2005, pp. 2413-2420.
- [42] Hillemanns, H. *et al.*, “Radiation hardness and detector performance of new 180nm CMOS MAPS prototype test structures developed for the upgrade of the ALICE Inner Tracking System”, in 2013 IEEE Nuclear Science Symposium and Medical Imaging Conference (2013 NSS/MIC), October 2013, pp. 1-5.

- [43] Snoeys, W. *et al.*, “Integrated circuits for particle physics experiments”, IEEE Journal of Solid-State Circuits, Vol. 35, No. 12, December 2000, pp. 2018-2030.
- [44] Anelli, G. *et al.*, “Radiation tolerant VLSI circuits in standard deep submicron CMOS technologies for the LHC experiments: practical design aspects”, IEEE Transactions on Nuclear Science, Vol. 46, No. 6, December 1999, pp. 1690-1696.
- [45] Snoeys, W. J., Gutierrez, T. A. P., Anelli, G., “A new NMOS layout structure for radiation tolerance”, in 2001 IEEE Nuclear Science Symposium Conference Record (Cat. No. 01CH37310), Vol. 2, November 2001, pp. 822-826.
- [46] Snoeys, W. *et al.*, “Layout techniques to enhance the radiation tolerance of standard CMOS technologies demonstrated on a pixel detector readout chip”, Nuclear Instruments and Methods in Physics Research Section A: Accelerators, Spectrometers, Detectors and Associated Equipment, Vol. 439, No. 2, 2000, pp. 349-360.
- [47] Petersen, E., Pickel, J., Adams, J., Smith, E., “Rate prediction for single event effects - a critique”, IEEE Transactions on Nuclear Science, Vol. 39, January 1993, pp. 1577-1599.
- [48] Spieler, H., Semiconductor Detector Systems. New York, USA: Oxford University Press, 2005.
- [49] Fossum, E. R., “CMOS image sensors: electronic camera on a chip”, in Proceedings of International Electron Devices Meeting, December 1995, pp. 17-25.
- [50] Turchetta, R. *et al.*, “A monolithic active pixel sensor for charged particle tracking and imaging using standard VLSI CMOS technology”, Nuclear Instruments and Methods in Physics Research Section A: Accelerators, Spectrometers, Detectors and Associated Equipment, Vol. 458, No. 3, 2001, pp. 677-689.
- [51] Sansen, W. M. C., Analog Design Essentials. Berlin, Germany: Springer-Verlag, 2006.
- [52] Krummenacher, F., “Pixel detectors with local intelligence: an IC designer point of view”, Nuclear Instruments and Methods in Physics Research Section A: Accelerators, Spectrometers, Detectors and Associated Equipment, Vol. 305, No. 3, 1991, pp. 527-532.
- [53] Prathapan, M. *et al.*, “Towards the large area HVCMOS demonstrator for ATLAS ITk”, Nuclear Instruments and Methods in Physics Research Section A: Accelerators, Spectrometers, Detectors and Associated Equipment, Vol. 936, 2019, pp. 389-391, Frontier Detectors for Frontier Physics: 14th Pisa Meeting on Advanced Detectors.
- [54] Marin Tobon, C. A., “PADRE pixel read-out architecture for Monolithic Active Pixel Sensor for the new ALICE Inner Tracking System in TowerJazz 180 nm technology”,

- Doctoral thesis, Universitat Politècnica de València, Valencia, Spain, 2017, available at: <https://cds.cern.ch/record/2316141>
- [55] Wang, T. *et al.*, “Depleted fully monolithic CMOS pixel detectors using a column based readout architecture for the ATLAS Inner Tracker upgrade”, *Journal of Instrumentation*, Vol. 13, No. 03, March 2018, pp. C03039.
- [56] Moustakas, K. *et al.*, “CMOS monolithic pixel sensors based on the column-drain architecture for the HL-LHC upgrade”, *Nuclear Instruments and Methods in Physics Research Section A: Accelerators, Spectrometers, Detectors and Associated Equipment*, Vol. 936, 2019, pp. 604-607, *Frontier Detectors for Frontier Physics: 14th Pisa Meeting on Advanced Detectors*.
- [57] Berdalovic, I. *et al.*, “Monolithic pixel development in TowerJazz 180 nm CMOS for the outer pixel layers in the ATLAS experiment”, *Journal of Instrumentation*, Vol. 13, January 2018, pp. C01023.
- [58] Scannicchio, D. A., “ATLAS trigger and data acquisition: Capabilities and commissioning”, *Nuclear Instruments and Methods in Physics Research Section A: Accelerators, Spectrometers, Detectors and Associated Equipment*, Vol. 617, 2010, pp. 306-309.
- [59] Aglieri, G. *et al.*, “Monolithic active pixel sensor development for the upgrade of the ALICE inner tracking system”, *Journal of Instrumentation*, Vol. 8, No. 12, December 2013, pp. C12041.
- [60] Snoeys, W. *et al.*, “A process modification for CMOS monolithic active pixel sensors for enhanced depletion, timing performance and radiation tolerance”, *Nuclear Instruments and Methods in Physics Research Section A: Accelerators, Spectrometers, Detectors and Associated Equipment*, Vol. 871, 2017, pp. 90-96.
- [61] Saks, N. S., Ancona, M. G., Modolo, J. A., “Radiation effects in MOS capacitors with very thin oxides at 80°K”, *IEEE Transactions on Nuclear Science*, Vol. 31, No. 6, December 1984, pp. 1249-1255.
- [62] Senyukov, S., Baudot, J., Besson, A., Claus, G., Cousin, L., Dorokhov, A., Dulinski, W., Goffe, M., Hu-Guo, C., Winter, M., “Charged particle detection performances of CMOS pixel sensors produced in a 0.18  $\mu\text{m}$  process with a high resistivity epitaxial layer”, *Nuclear Instruments and Methods in Physics Research Section A: Accelerators, Spectrometers, Detectors and Associated Equipment*, Vol. 730, 2013, pp. 115-118, *Proceedings of the 9th International Conference on Radiation Effects on Semiconductor Materials Detectors and Devices*.



- [63] van Hoorne, J., “The Investigator: an efficient tool to optimize design parameters of a CMOS pixel sensor”, in 2016 IEEE Nuclear Science Symposium and Medical Imaging Conference (2016 NSS/MIC), November 2016.
- [64] Riegel, C., Backhaus, M., Hoorne, J. V., Kugathasan, T., Musa, L., Pernegger, H., Riedler, P., Schaefer, D., Snoeys, W., Wagner, W., “Radiation hardness and timing studies of a monolithic TowerJazz pixel design for the new ATLAS Inner Tracker”, *Journal of Instrumentation*, Vol. 12, No. 01, January 2017, pp. C01015.
- [65] Pernegger, H. *et al.*, “First tests of a novel radiation hard CMOS sensor process for depleted monolithic active pixel sensors”, *Journal of Instrumentation*, Vol. 12, No. 06, June 2017, pp. P06008.
- [66] Cardella, R., Berdalovic, I., Egidos Plaja, N., Kugathasan, T., Marin Tobon, C. A., Pernegger, H., Riedler, P., Snoeys, W., “LAPA, a 5 Gb/s modular pseudo-LVDS driver in 180 nm CMOS with capacitively coupled pre-emphasis”, *Proceedings of Science*, Vol. TWEPP-17, 2017, pp. 038.5.
- [67] Kim, D. *et al.*, “Front end optimization for the monolithic active pixel sensor of the ALICE Inner Tracking System upgrade”, *Journal of Instrumentation*, Vol. 11, No. 02, February 2016, pp. C02042.
- [68] Caicedo, I. *et al.*, “The Monopix chips: Depleted monolithic active pixel sensors with a column-drain read-out architecture for the ATLAS Inner Tracker upgrade”, *Journal of Instrumentation*, Vol. 14, No. 06, 2019, pp. C06006.
- [69] Gao, C. *et al.*, “A novel source-drain follower for monolithic active pixel sensors”, *Nuclear Instruments and Methods in Physics Research Section A: Accelerators, Spectrometers, Detectors and Associated Equipment*, Vol. 831, 2016, pp. 147-155, *Proceedings of the 10th International “Hiroshima” Symposium on the Development and Application of Semiconductor Tracking Detectors*.
- [70] Pelgrom, M. J. M., Duinmaijer, A. C. J., Welbers, A. P. G., “Matching properties of MOS transistors”, *IEEE Journal of Solid-State Circuits*, Vol. 24, No. 5, October 1989, pp. 1433-1439.
- [71] Hillemanns, H., Cavicchioli, C., Kugathasan, T., Marin Tobon, C., Musa, L., Riedler, P., Snoeys, W., “Total ionizing dose effects in 180nm CMOS structures for monolithic active pixel sensors for the ALICE Inner Tracking System detector upgrade”, November 2013, unpublished.

- [72] Berdalovic, I. *et al.*, “MALTA: a CMOS pixel sensor with asynchronous readout for the ATLAS High-Luminosity upgrade”, in 2018 IEEE Nuclear Science Symposium and Medical Imaging Conference (2018 NSS/MIC), in press.
- [73] Kugathasan, T. *et al.*, “Monolithic pixel development in 180 nm CMOS for the outer pixel layers in the ATLAS experiment”, Proceedings of Science, Vol. TWEPP-17, 2017, pp. 047.
- [74] Cardella, R. *et al.*, “MALTA: an asynchronous readout CMOS monolithic pixel detector for the ATLAS High-Luminosity upgrade”, Journal of Instrumentation, Vol. 14, No. 06, 2019, pp. C06019.
- [75] Horstmann, M., picoTDC: Picosecond Time to Digital Converter, Draft manual V. 0.5, CERN, Geneva, Switzerland, 2018.
- [76] Hiti, B. *et al.*, “Development of the monolithic MALTA CMOS sensor for the ATLAS ITK outer pixel layer”, Proceedings of Science, Vol. TWEPP-18, 2018, pp. 155.
- [77] McGoldrick, G., Cerv, M., Gorisek, A., “Synchronized analysis of testbeam data with the Judith software”, Nuclear Instruments and Methods in Physics Research Section A Accelerators Spectrometers Detectors and Associated Equipment, Vol. 765, 11 2014, pp. 140-145.
- [78] Snoj, L., Zerovnik, G., Trkov, A., “Computational analysis of irradiation facilities at the JSI TRIGA reactor”, Applied Radiation and Isotopes, Vol. 70, No. 3, 2012, pp. 483-488.
- [79] Munker, M., Benoit, M., Dannheim, D., Fenigstein, A., Kugathasan, T., Leitner, T., Pernegger, H., Riedler, P., Snoeys, W., “Simulations of CMOS pixel sensors with a small collection electrode, improved for a faster charge collection and increased radiation tolerance”, Journal of Instrumentation, Vol. 14, No. 05, 2019, pp. C05013.
- [80] Moscatelli, F., Passeri, D., Morozzi, A., Mendicino, R., Dalla Betta, G. ., Bilei, G. M., “Combined bulk and surface radiation damage effects at very high fluences in silicon detectors: Measurements and TCAD simulations”, IEEE Transactions on Nuclear Science, Vol. 63, No. 5, October 2016, pp. 2716-2723.
- [81] Allport, P. *et al.*, “Recent results and experience with the Birmingham MC40 irradiation facility”, Journal of Instrumentation, Vol. 12, No. 03, March 2017, pp. C03075.
- [82] Garcia-Sciveres, M., Loddo, F., “RD53B Manual”, CERN, Geneva, Tech. Rep. CERN-RD53-PUB-19-002, March 2019, available at: <https://cds.cern.ch/record/2665301>

# Biography

Ivan Berdalović was born in Mohács, Hungary, on 8 November 1992. He finished primary and secondary school in Beli Manastir, Croatia, after which he started his studies in Electrical Engineering and Information Technology at the Faculty of Electrical Engineering and Computing at the University of Zagreb. During his studies, he worked on subjects in the field of microelectronics, semiconductor technology, optoelectronics as well as analogue and digital integrated circuits. Other than having an excellent grade point average, he also received the "Josip Lončar" award for his success during the first year of Master studies as well as the Rector's Award for best scientific paper. He received his MSc in 2016 on the topic of single-photon avalanche photodetectors, after which he was hired as a PhD student at the European Organisation for Nuclear Research (CERN), where he has been working on the design of advanced pixel detectors for the ATLAS experiment. Apart from technical training in the topics of microelectronics and detectors, during his PhD he also attended courses on innovation management and technological competence leveraging, and acquired a PRINCE2 certificate in project management. He is the author and co-author of numerous papers on avalanche photodiodes and radiation-hard pixel detectors, and he has participated in several international conferences.

## List of publications

### Journal articles

1. I. Berdalovic, R. Bates, C. Buttar, R. Cardella, N. Egidos Plaja, T. Hemperek, B. Hiti, J.W. van Hoorne, T. Kugathasan, I. Mandic, D. Maneuski, C.A. Marin Tobon, K. Moustakas, L. Musa, H. Pernegger, P. Riedler, C. Riegel, D. Schaefer, E.J. Schioppa, A. Sharma, W. Snoeys, C. Solans Sanchez, T. Wang and N. Wermes, "Monolithic pixel development in TowerJazz 180 nm CMOS for the outer pixel layers in the ATLAS experiment", Proceedings of the 11th International Conference on Position Sensitive Detectors (PSD 11), Journal of Instrumentation, vol. 13, C01023, 2018.
2. T. Wang, M. Barbero, I. Berdalovic, C. Bepin, S. Bhat, P. Breugnon, I. Caicedo, R. Cardella, Z. Chen, Y. Degerli, N. Egidos, S. Godiot, F. Guilloux, T. Hemperek, T. Hirono, H. Krüger, T. Kugathasan, F. Hügging, C.A. Marin Tobon, K. Moustakas, P. Pangaud, P.

- Schwemling, H. Pernegger, D.-L. Pohl, A. Rozanov, P. Rymaszewski, W. Snoeys and N. Wermes, “Depleted fully monolithic CMOS pixel detectors using a column based readout architecture for the ATLAS Inner Tracker upgrade”, Proceedings of the 19th International Workshop on Radiation Imaging Detectors (IWORID 2017), Journal of Instrumentation, vol. 13, C03039, 2018.
3. K. Moustakas, M. Barbero, I. Berdalovic, C. Bepin, P. Breugnon, I. Caicedo, R. Cardella, Y. Degerli, N. Egidos Plaja, S. Godiot, F. Guilloux, T. Hemperek, T. Hirono, H. Krueger, T. Kugathasan, C. A. Marin Tobon, P. Pangaud, H. Pernegger, E. J. Schioppa, W. Snoeys, M. Vandenbroucke, T. Wang and N. Wermes, “CMOS monolithic pixel sensors based on the column-drain architecture for the HL-LHC upgrade”, Nuclear Instruments and Methods in Physics Research Section A: Accelerators, Spectrometers, Detectors and Associated Equipment, vol. 936, 2019, pp. 604-607.
  4. R. Cardella, I. Asensi Tortajada, I. Berdalovic, F. Dachs, V. Dao, L. Flores Sanz de Acedo, F. Piro, T. Hemperek, B. Hiti, T. Kugathasan, C. A. Marin Tobon, K. Moustakas, H. Pernegger, P. Riedler, P. Rymaszewski, E. J. Schioppa, A. Sharma, L. Simon Argemi, W. Snoeys, C. Solans Sanchez, T. Wang and N. Wermes, “MALTA: an asynchronous readout CMOS monolithic pixel detector for the ATLAS High-Luminosity upgrade”, Proceedings of the 9th International Workshop on Semiconductor Pixel Detectors for Particles and Imaging (PIXEL 2018), Journal of Instrumentation, vol. 14, C06019, 2019.
  5. I. Caicedo, M. Barbero, P. Barrillon, I. Berdalovic, S. Bhat, C. Bepin, P. Breugnon, R. Cardella, Z. Chen, Y. Degerli, J. Dingfelder, S. Godiot, F. Guilloux, T. Hirono, T. Hemperek, F. Hügging, H. Krüger, T. Kugathasan, K. Moustakas, P. Pangaud, H. Pernegger, D.-L. Pohl, P. Riedler, A. Rozanov, P. Rymaszewski, P. Schwemling, W. Snoeys, M. Vandenbroucke, T. Wang and N. Wermes, “The Monopix chips: depleted monolithic active pixel sensors with a column-drain read-out architecture for the ATLAS Inner Tracker upgrade”, Proceedings of the 9th International Workshop on Semiconductor Pixel Detectors for Particles and Imaging (PIXEL 2018), Journal of Instrumentation, vol. 14, C06006, 2019.

## Conference proceedings

1. I. Berdalović, Ž. Osrečki, F. Šegmanović, D. Grubišić, T. Knežević, T. Suligoj, “Design of passive-quenching active-reset circuit with adjustable hold-off time for single-photon avalanche diodes”, Proceedings of the 39th International Convention on Information and Communication Technology, Electronics and Microelectronics (MIPRO 2016)
2. T. Kugathasan, R. Bates, C. Buttar, I. Berdalovic, B. Blochet, R. C. Cardella, M. Dalla, N. Egidos Plaja, T. Hemperek, J. W. Van Hoorne, D. Maneuski, C. A. Marin Tobon, K. Moustakas, H. Mugnier, L. Musa, H. Pernegger, P. Riedler, C. Riegel, J. Rousset, C.

- Sbarra, D. M. Schaefer, E. J. Schioppa, A. Sharma, W. Snoeys, C. Solans Sanchez, T. Wang and N. Vermes, “Monolithic pixel development in 180 nm CMOS for the outer pixel layers in the ATLAS experiment”, Proceedings of the Topical Workshop on Electronics for Particle Physics (TWEPP 2017).
3. R. Cardella, I. Beraldovic, N. Egidios Plaja, T. Kugathasan, C. A. Marin Tobon, H. Pernegger, P. Riedler and W. Snoeys, “LAPA, a 5 Gb/s modular pseudo-LVDS driver in 180 nm CMOS with capacitively coupled pre-emphasis”, Proceedings of the Topical Workshop on Electronics for Particle Physics (TWEPP 2017).
  4. I. Beraldovic, L. Simon Argemi, R. Cardella, F. Dachs, V. Dao, L. Flores Sanz de Acedo, T. Hemperek, B. Hiti, T. Kugathasan, C. A. Marin Tobon, K. Moustakas, H. Pernegger, F. Piro, P. Riedler, E. J. Schioppa, A. Sharma, W. Snoeys, C. Solans Sanchez, T. Suligoj, T. Wang, P. Rymaszewski and I. Asensi Tortajada, “MALTA: a CMOS pixel sensor with asynchronous readout for the ATLAS High-Luminosity upgrade”, Proceedings of the 2018 IEEE Nuclear Science Symposium and Medical Imaging Conference (NSS/MIC 2018).
  5. B. Hiti, L. Argemi, I. Asensi Tortajada, I. Beraldovic, I. Caicedo Sierra, R. Cardella, F. Dachs, V. Dao, N. Egidios Plaja, A. Gorisek, T. Hemperek, H. Kruger, T. Kugathasan, I. Mandic, C. A. Marin Tobon, K. Moustakas, M. Munker, H. Pernegger, F. Piro, P. Riedler, P. Rymaszewski, C. Riegel, E. J. Schioppa, A. Sharma, W. Snoeys, C. Solans Sanchez, T. Wang and N. Vermes, “Development of the monolithic MALTA CMOS sensor for the ATLAS ITk outer pixel layer”, Proceedings of the Topical Workshop on Electronics for Particle Physics (TWEPP 2018).

# Životopis

Ivan Berdalović rođen je u Mohácsu, u Mađarskoj, 8.11.1992. Osnovnu i srednju i školu završava u Belom Manastiru, a potom upisuje studij elektrotehnike i informacijske tehnologije na Fakultetu Elektrotehnike i računarstva Sveučilišta u Zagrebu. Tijekom studija bavi se predmetima na području mikroelektronike, poluvodičke tehnologije, optoelektronike te analognih i digitalnih integriranih sklopova. Uz odličan prosjek prima i nagradu "Josip Lončar" za uspjeh na prvoj godini diplomskog studija te Rektorovu nagradu za najbolji znanstveni rad. Magistrirao je 2016. na temu fotodetektora s lavinskom multiplikacijom za detekciju jednog fotona, nakon čega se zapošljava kao doktorand u Europskoj organizaciji za nuklearna istraživanja (CERN), gdje se bavi projektiranjem naprednih piksel detektora za eksperiment ATLAS. Osim stručnog usavršavanja na području mikroelektronike i detektora, tijekom doktorata sudjeluje i na tečajevima o menadžmentu inovacijama i primjeni tehnologija u poslovnom svijetu, te stječe i certifikat PRINCE2 za upravljanje projektima. Autor je i koautor brojnih radova na temu fotodioda s lavinskom multiplikacijom i piksel detektora otpornih na zračenje, te je sudjelovao na nekolicini međunarodnih konferencija.